

ARTICLE

Partial-differential-algebraic equations of nonlinear dynamics by Physics-Informed Neural-Network: (I) Operator splitting and framework assessment

Dedicated to Professor Robert L. Taylor for his 90th birthday.

Loc Vu-Quoc^{1,✉} and Alexander Humer²

^{1,✉} Aerospace Engineering, University of Illinois at Urbana-Champaign, IL 61801, USA • ✉ vql@illinois.edu

² Institute of Technical Mechanics, Johannes Kepler University, A-4040 Linz, Austria • alexander.humer@jku.at

ABSTRACT

Several forms for constructing novel physics-informed neural-networks (PINNs) for the solution of partial-differential-algebraic equations (PDAEs) based on derivative operator splitting are proposed, using the nonlinear Kirchhoff rod as a prototype for demonstration.

The present work is a natural extension of our review paper in [1] aiming at both experts and first-time learners of both deep learning and PINN frameworks, among which the open-source DeepXDE (DDE) [2] is likely the most well documented framework with many examples. Yet, we encountered some pathological problems (time shift, amplification, static solutions) and proposed novel methods to resolve them.

Among these novel methods are the PDE forms, which evolve from the lower-level form with fewer unknown dependent variables (e.g., displacements, slope, finite extension) to higher-level form with more dependent variables (e.g., forces, moments, momenta, etc.), in addition to those from lower-level forms. Traditionally, the highest-level form, the balance-of-momenta form, is the starting point for (hand) deriving the lowest-level form through a tedious (and error prone) process of successive substitutions. The next step in a finite element method is to discretize the lowest-level form upon forming a weak form and linearization with appropriate interpolation functions, followed by their implementation in a code and testing. The time-consuming tedium in all of these steps could be bypassed by applying the proposed novel PINN directly to the highest-level form.

We also developed a script based on [JAX](#), the High Performance Array Computing. For the axial motion of elastic bar, while our [JAX](#) script did not show the pathological problems of [DDE-T](#) (DDE with TensorFlow backend), it is slower than [DDE-T](#). Moreover, that [DDE-T](#) itself being more efficient in higher-level form than in lower-level form makes working directly with higher-level form even more attractive in addition to the advantages mentioned further above.

Since coming up with an appropriate learning-rate schedule for a good solution is more art than science, we systematically codified in detail our experience running optimization through a normalization/standardization of the network-training process so readers can reproduce our results.

KEYWORDS

PINN, Physics-Informed Neural Network; Beam, small deformation, Euler-Bernoulli, large deformation, Kirchhoff rod, statics, dynamics.

TABLE OF CONTENTS

1	Introduction	2
2	PDEAs: Beam formulations with no shear	4
2.1	Geometrically-exact beam with no shear, Kirchhoff rod	4
2.1.1	Kinematics, finite extension, constitutive relations	4
2.1.2	Balance of momenta, non-dimensional form	5
2.1.3	Constitutive relations, non-dimensional form	7
2.1.4	Equations of motion, non-dimensional form	7
2.1.5	Input parameters: Boundary and initial conditions, distributed load	8
2.2	Inconsistency, reduction from geometrically-exact beam with shear	9

2.3	Small deformation, Euler-Bernoulli	10
3	PINN formulations	11
3.1	Inputs	11
3.2	Form 1: No operator splitting	12
3.3	Form 2a: Split time derivatives	12
3.4	Form 2b: Split space derivatives	13
3.5	Form 3: Split time and space derivatives	13
3.6	Form 4: Balance of momenta with no substitution	13
4	Generic PDEs, auxilliary conditions, loss function	14
5	Numerical examples	14
5.1	Network architecture, data-point grids	15
5.2	Training (optimization) learning-rate scheduling	17
5.3	Axial motion of elastic bar	29
5.3.1	Form 1: Shift, amplification, early stopping, static solution	29
5.3.2	Form 2a: No time shift, static solution, efficiency	34
5.3.3	Form 2b: Same issues as Form 1	36
5.3.4	Form 3 (or 4): No space/time shift, static solution, efficiency	42
6	Closure	49
	References	49
	Appendices	52
1	Analysis of time shift and amplification	52
2	Filtering static solutions, barrier functions	54
3	Error relative to exact solution, generalization	57

1 Introduction

As a prototype of partial-differential-algebraic equations (PDAEs) for novel physics-informed neural network (PINN) formulations, the geometrically-exact rod with no shear is considered here, starting with the assumption often attributed to Kirchhoff (or Kirchhoff-Clebsch, or Kirchhoff-Love, or Kirchhoff-Clebsch-Love; see the review in [3] [4] and the references therein): Plane cross section initially perpendicular to the undeformed centroidal line remains perpendicular to the deformed centroidal line.¹

Our formulation's starting point is similar to that in [4], then takes on a different direction as we are aiming at developing a finite deformable rod, without introducing approximations, culminating in a system of nonlinear partial differential equations, complemented by algebraic expressions with derivatives (AEDs), i.e., a PDAE system of the form

$$\mathcal{D}_i^{(k)}(\mathbf{u}(X, t), t) = 0, \quad \mathbf{u}(X, t) := \left[\{\partial_X^p u_j, \partial_X^{p-1} u_j, \dots, \partial_X^1 u_j\}, \{\partial_t^q u_j, \partial_X^{q-1} u_j, \dots, \partial_t^1 u_j\}, u_j \right], \quad (82)$$

where $\mathcal{D}_i^{(k)}$ is a nonlinear differential operator, operating on $\mathbf{u}(X, t)$, which collects the unknown dependent variables $\{u_j\}$ and their partial derivatives, with $\{k, i, j, p, q\}$ being indices to be defined later in the paper.

An example of a PDAE system is the motion of the Kirchhoff-rod Form-1 (Section 3.2) Eq. (41), Eq. (42), Eq. (36), Eq. (43); these equations form an implicit system of nonlinear PDEs in terms of the four dependent variables $\{\bar{u}, \bar{v}, \bar{\alpha}\}, \bar{k}$. While it is possible to eliminate two dependent variables $\{\bar{\alpha}, \bar{k}\}$ by

¹Even though this assumption is part of the ‘‘Kirchhoff-Love hypotheses’’ in contemporary literature, neither Kirchhoff, nor Love, made these hypotheses [3], in which the author wrote ‘‘Major and minor authors alike have found the arguments of KIRCHHOFF not persuasive.’’ The method of derivation in the 1992 review paper [3] based on the first Piola-Kirchhoff stress tensor closely resembles, however, the derivation in Simo (1982) [5], Simo, Heljmsstad & Taylor (1984) [6], and Simo (1985) [7].

substituting Eq. (36) and Eq. (43) into Eq. (41) and Eq. (42), the resulting equations, which can be put in generic form as,

$$\dot{\mathbf{y}}(X, t) = \mathbb{F}(\mathbf{y}(X, t), t), \quad (1)$$

where the partial space derivatives are included in the nonlinear operator \mathbb{F} , become much more complex.

After deep learning achieved a sharp decrease in image classification error in 2012, and then by 2015 surpassed human performance [1], research in AI was revived after a long “winter” and took on a burgeoning turn, especially in deep learning. Following this trend, as a method to solve PDEs without a need for discretization as in traditional methods (such as finite-difference, finite-element, boundary-element methods), physics-informed neural network (PINN) was reintroduced [8] [9] after a long dormant period since first proposed in the late 1990s [10] [11]. PINN is given a key role in “Multi-physics & multi-scale modeling,” the first of the nine motifs in the “Simulation Intelligence” roadmap proposed in [12]. For nonlinear problems, it is recently reported that PINN is 37 times faster than the traditional finite-difference method [13]. Since PINN converts all problems, even linear ones, to a nonlinear optimization problem, the more a problem is nonlinear, the better for the application of PINN.

This present work is a natural extension of our review paper in [1] aiming at both experts and first-time learners of both deep learning and PINN frameworks, among which the open-source DeepXDE (DDE) [2] is likely the most well documented framework with many examples and a forum for discussion among users. So naturally, we chose to implement our novel PINN formulations in DDE with TensorFlow backend, abbreviated as **DDE-T**. Yet, we encountered some pathological problems (time shift, amplification, static solutions, as exemplified through the motion of an elastic bar) and propose novel methods to resolve them.

Among these novel PINN formulations are the different PDE forms, obtained by splitting the derivative operators, evolving from the lower-level form with fewer unknown dependent variables (e.g., displacements, slope, finite extension; see the Kirchhoff-rod Form 1 in Section 3.2) to higher-level form with more dependent variables (e.g., forces, moments, momenta, etc.), in addition to those from lower-level forms (see Kirchhoff-rod Form 4 in Section 3.6).

Traditionally, the highest-level form, the balance-of-momenta form, is the starting point for (hand) deriving the lowest-level form through a tedious (and error prone) process of successive substitutions. The next step in a finite element method is to discretize the lowest-level form, after forming the weak form and constructing a linearization, with appropriate interpolation functions, followed by their implementation and testing in a FE code [14] [15] [16]. There are a number of finite-element frameworks to choose from, e.g., the Berkeley code **FEAP** by Taylor [17] and **Netgen/NGSolve** [18].

The time-consuming tedium of all of these traditional steps could be bypassed by our novel application of PINN directly to the highest-level momentum form.²

Perplexed with the number of pathological problems encountered with linear dynamic problems when using **DDE-T**, as mentioned above, in parallel with developing novel methods to circumvent the problems in **DDE-T**, we also developed a script based on **JAX**, the High Performance Array Computing.

For the axial motion of elastic bar, while our **JAX** script did not show the pathological problems of **DDE-T** (DDE with TensorFlow backend), and is faster than **DDE-T** for lower-level Form 1, it is slower than **DDE-T** in all PDE forms tested. Moreover, that **DDE-T** itself being more efficient in higher-level form than in lower-level form makes working directly with higher-level form even more attractive in addition to the advantages mentioned further above.

Arriving at an appropriate learning-rate schedule for a category of problems is more art than science,

² To filter the static solutions with near-zero acceleration encountered when using **DDE-T**, we introduce various forms of barrier functions, a novelty in PINN formulations, with room for improvements. A full-length report, with much more details than in the shortened version by half that is the present paper, can be found on arXiv.org [?].

and has to be done by trial-and-error. Because of the large number of parameters in the training process, we systematically codify our experience running optimization (training process) through a normalization/-standardization of the network-training process and the result presentation so readers could understand and reproduce our results. The training speed, or computational efficiency, is most likely related to how the gradient is computed in different software (e.g., [DDE-T](#) vs [JAX](#)).

Large computational efficiency is recently obtained with the proposed novel PINN formulations for the transverse motion of the Euler-Bernoulli beam and for the geometrically-exact Kirchhoff rod to be reported in a follow-up publication.

2 PDEAs: Beam formulations with no shear

As a particular case of the general partial-differential-algebraic equations (PDEAs) represented by Eq. (82), consider the geometrically-exact beam with no shear, i.e., the Kirchhoff rod, a derivation for which is first provided followed by pointing out the inconsistency of such formulation based on geometrically-exact beam with shear. Then approximations are introduced to recover the classical linear Euler-Bernoulli beam with axial deformation in preparation for an implementation in a PINN framework, beginning with [DDE-T](#), then with [JAX](#).

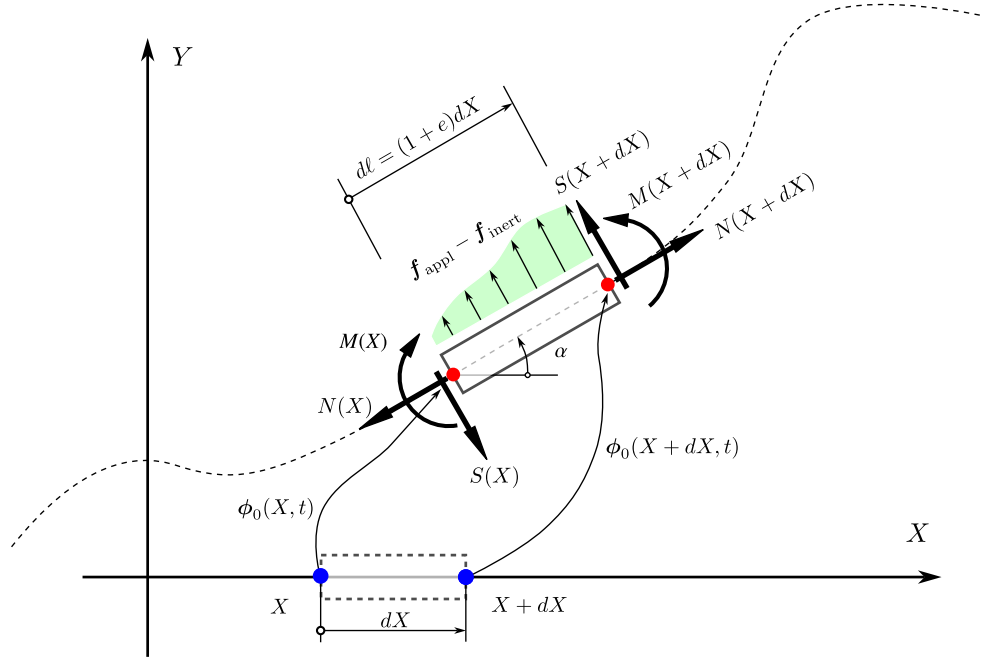


Figure 1: *Geometrically-exact beam without shear deformation.* Section 2.1. Shear forces introduced for equilibrium. Section 2.2: Inconsistency in Kirchhoff rod (large deformation) and Euler-Bernoulli (small deformation) beam theories. Figure 2, geometrically-exact beam with shear deformation.

2.1 Geometrically-exact beam with no shear, Kirchhoff rod

All equations are first derived in dimensional form, then subsequently converted to non-dimensional form.

2.1.1 Kinematics, finite extension, constitutive relations

Figure 1 provides a pictorial definition of the finite extension e expressed as

$$e = \frac{d\ell}{dL} - 1 = \frac{d\ell}{dX} - 1, \text{ with } dL = dX, \text{ and } d\ell = (1 + e)dX, \quad (2)$$

with the following kinematics of deformation $(x, y) = \phi_0(X, t)$ such that

$$x = X + u(X, t) \Rightarrow dx = dX + du = d\ell \cos \alpha, \quad y = v(X, t) \Rightarrow dy = dv = d\ell \sin \alpha, \quad (3)$$

where $\{u(X, t), v(X, t)\}$ are the axial and transversal displacements, respectively. The gradients of the spatial coordinates (x, y) with respect to the material coordinate X are then:

$$\frac{dx}{dX} = 1 + u^{(1)} = \frac{d\ell \cos \alpha}{dL} = (1 + e) \cos \alpha, \quad \frac{dy}{dX} = v^{(1)} = \frac{d\ell \sin \alpha}{dL} = (1 + e) \sin \alpha, \quad (4)$$

which give rise to the expression for the slope α of the centroidal line, together with the relations involving finite extension e and the displacements (u, v) :

$$\tan \alpha = \frac{v^{(1)}}{1 + u^{(1)}}, \quad e \cos \alpha = 1 + u^{(1)} - \cos \alpha, \quad e \sin \alpha = v^{(1)} - \sin \alpha. \quad (5)$$

The last two expressions in Eq. (5)_{2,3} provide then the extension for e in terms of the displacements (u, v) and the slope α :

$$e = \left[\left(1 + u^{(1)} - \cos \alpha \right)^2 + \left(v^{(1)} - \sin \alpha \right)^2 \right]^{1/2}. \quad (6)$$

Using Eq. (4), some convenient variables involving the extension e and the displacement derivatives $(u^{(1)}, v^{(1)})$ are introduced:

$$\mathcal{C}^2 := (1 + e)^2 = \left[1 + u^{(1)} \right]^2 + \left[v^{(1)} \right]^2 \Rightarrow \mathcal{C} = \left\{ \left[1 + u^{(1)} \right]^2 + \left[v^{(1)} \right]^2 \right\}^{1/2} =: \mathcal{K}^{-1}. \quad (7)$$

The traditional elastic axial and bending constitutive relations are:

$$N = EA e, \quad M = EI \alpha^{(1)}. \quad (8)$$

2.1.2 Balance of momenta, non-dimensional form

Referring to Figure 1, the equilibrium of forces and moment of the depicted infinitesimal segment leads to the following expressions.

Balance of linear momentum along X axis:

$$\begin{aligned} \sum F_X = 0 &= \left[(N \cos \alpha)|_{X+dX} - (N \cos \alpha)|_X \right] - \left[(S \sin \alpha)|_{X+dX} - (S \sin \alpha)|_X \right] \\ &+ f_X^{\text{appl}} dX - f_X^{\text{inert}} dX = d(N \cos \alpha) - d(S \sin \alpha) + f_X dX - (\rho A dX) \ddot{u}. \end{aligned} \quad (9)$$

Balance of linear momentum along Y axis:

$$\begin{aligned} \sum F_Y = 0 &= \left[(N \sin \alpha)|_{X+dX} - (N \sin \alpha)|_X \right] - \left[(S \cos \alpha)|_{X+dX} - (S \cos \alpha)|_X \right] \\ &+ f_Y^{\text{appl}} dX - f_Y^{\text{inert}} dX = d(N \sin \alpha) - d(S \cos \alpha) + f_Y dX - (\rho A dX) \ddot{v}. \end{aligned} \quad (10)$$

Balance of angular momentum:

$$\sum M|_a = 0 = -M(X) + M(X + dX) + S(X + dX) d\ell + M_{\text{appl}} - M_{\text{inert}}, \quad (11)$$

$$\text{with } M_{\text{appl}} = O(d\ell^2), \quad M_{\text{inert}} = \rho I_A d\ell \ddot{\mathbf{s}}_v \quad (12)$$

Neglecting higher-order terms in $d\ell$ and the area moment of inertia I_A of the cross section A as customarily done for thin beams without shear deformation, and taking the limit $dX \rightarrow 0$, we obtain

$$0 = \frac{dM}{dX} \frac{dX}{d\ell} + S \Rightarrow 0 = \frac{dM}{dX} + (1 + e)S = M^{(1)} + cS . \quad (13)$$

Non-dimensionalization

Coordinates and displacements, using Eq. (3):

$$\bar{X} = \frac{X}{L} , \quad \bar{x} = \frac{x}{L} = \bar{X} + \bar{u} , \quad \bar{u} = \frac{u}{L} , \quad \bar{y} = \frac{y}{L} = \frac{v}{L} = \bar{v} , \quad (14)$$

$$[\bar{X}] = [\bar{x}] = [\bar{u}] = [\bar{y}] = [\bar{v}] = 1 . \quad (15)$$

Normal force and shear force:

$$\bar{N} = \frac{L^2}{EI} N, \text{ with } \left[\frac{L^2}{EI} \right] = \frac{\mathcal{L}^2}{(\mathcal{F}/\mathcal{L}^2)\mathcal{L}^4} = \frac{1}{\mathcal{F}}, \text{ and } [N] = \mathcal{F}, \text{ so } [\bar{N}] = 1 , \quad (16)$$

$$\bar{S} = \frac{L^2}{EI} S, \text{ and } [\bar{S}] = 1 . \quad (17)$$

In Eq. (16), $[N] = \mathcal{F}$ means the axial force N has the dimension of force, denoted by \mathcal{F} , and similarly for length \mathcal{L} , mass \mathcal{M} , and time \mathcal{T} as used in Eq. (20) below.

Distributed force using Eq. (16):

$$\bar{f} = \frac{L^3}{EI} f, \text{ with } [\bar{f}] = \left[\frac{L^3}{EI} \right] [f] = \frac{\mathcal{L}^3}{\mathcal{F}\mathcal{L}} = 1 \quad (18)$$

Moment:

$$\bar{M} = \frac{L}{EI} M, \text{ since } [\bar{M}] = \left[\frac{L}{EI} \right] [M] = \frac{\mathcal{L}}{\mathcal{F}\mathcal{L}} = 1 . \quad (19)$$

Time:

$$\tau := L^2 \sqrt{(\rho A)/(EI)}; \text{ since } \left[\frac{\rho A}{EI} \right] = \frac{\mathcal{M}/\mathcal{L}}{\mathcal{F}\mathcal{L}^2} = \frac{\mathcal{M}/\mathcal{L}}{(\mathcal{M}\mathcal{L}/\mathcal{T}^2)\mathcal{L}^2} = \frac{\mathcal{T}^2}{\mathcal{L}^4}, \text{ thus } [\tau] = \mathcal{T} , \quad (20)$$

$$\bar{t} = \frac{t}{\tau}, \text{ and } [\bar{t}] = 1 . \quad (21)$$

Balance of momenta

Space derivative of a generic force $F(X)$:

$$F^{(1)} = \frac{dF(X)}{dX} = \frac{d\bar{X}}{dX} \frac{d}{d\bar{X}} \left(\frac{EI}{L^2} \bar{F}(\bar{X}) \right) = \frac{1}{L} \frac{EI}{L^2} \frac{d\bar{F}(\bar{X})}{d\bar{X}} = \frac{EI}{L^3} \bar{F}^{(1)} . \quad (22)$$

Time derivatives of a generic displacement function $x(t)$ with length dimension \mathcal{L} :

$$\dot{x} = \frac{dx}{dt} = \frac{d\bar{t}}{dt} \frac{d[L\bar{x}(\bar{t})]}{d\bar{t}} = \frac{L}{\tau} \frac{d\bar{x}(\bar{t})}{d\bar{t}} = \frac{L}{\tau} \dot{\bar{x}}, \quad (23)$$

$$\ddot{x} = \frac{L}{\tau} \frac{d\bar{t}}{dt} \frac{d^2\bar{x}(\bar{t})}{(d\bar{t})^2} = \frac{L}{\tau^2} \ddot{\bar{x}} = \frac{EI}{\rho AL^3} \ddot{\bar{x}}. \quad (24)$$

Generic balance of linear momentum in non-dimensional form using Eq. (21), Eq. (22) and Eq. (24):

$$F^{(1)} + f = \rho A \ddot{x} \Rightarrow \bar{F}^{(1)} + \bar{f} = \ddot{\bar{x}}. \quad (25)$$

Space derivative of displacements and extension using Eq. (14):

$$\frac{\partial u(X, t)}{\partial X} =: u^{(1)} = \frac{\partial \bar{X}}{\partial X} \frac{\partial [L\bar{u}(\bar{X}, \bar{t})]}{\partial \bar{X}} = \frac{\partial \bar{u}(\bar{X}, \bar{t})}{\partial \bar{X}} =: \bar{u}^{(1)}, \text{ and } v^{(1)} = \bar{v}^{(1)}. \quad (26)$$

Similarly, using Eq. (26) in Eqs. (5)-(6) and Eq. (7), we have:

$$\alpha = \bar{\alpha}, \quad e = \bar{e}, \quad e \cos \alpha = \bar{e} \cos \bar{\alpha}, \quad e \sin \alpha = \bar{e} \sin \bar{\alpha}, \quad c = \bar{c}, \quad k = \bar{k}. \quad (27)$$

Using Eq. (25) in Eq. (9) and Eq. (10), together with Eq. (27)₁, we have the balance of linear momenta along \bar{X} and \bar{Y} as:

$$(\bar{N} \cos \bar{\alpha})^{(1)} - (\bar{S} \sin \bar{\alpha})^{(1)} + \bar{f}_{\bar{X}} = \ddot{\bar{u}}, \quad (\bar{N} \sin \bar{\alpha})^{(1)} + (\bar{S} \cos \bar{\alpha})^{(1)} + \bar{f}_{\bar{Y}} = \ddot{\bar{v}}. \quad (28)$$

Space derivative of moment from Eq. (19) and similar to Eq. (22), we have:

$$M^{(1)} = \frac{EI}{L^2} \bar{M}^{(1)}. \quad (29)$$

Balance of angular momentum. Eq. (13) in non-dimensional form based on Eq. (29), Eq. (17), and Eq. (27)₅:

$$M^{(1)} + cS = 0 \Rightarrow \bar{M}^{(1)} + \bar{c}\bar{S} = 0, \quad (30)$$

which \bar{c} can be expressed in terms of the space derivative of the displacement components (\bar{u}, \bar{v}) as defined in Eq. (7), using Eq. (26).

2.1.3 Constitutive relations, non-dimensional form

Non-dimensional constitutive relation for axial deformation:

$$N = EAe \Rightarrow \frac{EI}{L^2} \bar{N} = EA\bar{e} \Rightarrow \bar{N} = \frac{AL^2}{I} \bar{e} = \mathcal{J} \bar{e}, \quad (31)$$

with non-dimensional slenderness parameter \mathcal{J} and its inverse being the rotundness \mathcal{R}

$$\mathcal{J} := \frac{AL^2}{I} \Leftrightarrow \mathcal{R} := \mathcal{J}^{-1} = \frac{I}{AL^2}. \quad (32)$$

The space derivative of the slope α of the centroidal line is:

$$\alpha^{(1)} = \frac{\partial \alpha}{\partial X} = \frac{\partial \bar{X}}{\partial X} \frac{\partial \bar{\alpha}}{\partial \bar{X}} = \frac{1}{L} \bar{\alpha}^{(1)}. \quad (33)$$

Non-dimensional constitutive relations for bending deformation using Eq. (8), Eq. (19), and Eq. (33):

$$M = EI\alpha^{(1)} \Rightarrow \bar{M} = \bar{\alpha}^{(1)}. \quad (34)$$

2.1.4 Equations of motion, non-dimensional form

The first two terms in each of the non-dimensional balance of linear momentum in \bar{X} and in \bar{Y} direction, respectively, as expressed in Eq. (28) can be written in terms of displacements as follows. Using the axial constitutive relation Eq. (31) and the definition of α in Eq. (5) together with the expressions related to the

finite extension e defined in Eqs. (5)-(6), and again using Eq. (27), we have:

$$\bar{N} \cos \bar{\alpha} = \mathcal{J} \bar{e} \cos \bar{\alpha} = \mathcal{J} \left[1 + \bar{u}^{(1)} - \cos \bar{\alpha} \right], \quad \bar{N} \sin \bar{\alpha} = \mathcal{J} \bar{e} \sin \bar{\alpha} = \mathcal{J} \left[\bar{v}^{(1)} - \sin \bar{\alpha} \right], \quad (35)$$

$$\tan \bar{\alpha} = \frac{\bar{v}^{(1)}}{1 + \bar{u}^{(1)}}, \quad (36)$$

from which the first term as a function of $(\bar{N}, \bar{\alpha})$ with a space derivative, in each equation in Eq. (28) is, respectively:

$$(\bar{N} \cos \bar{\alpha})^{(1)} = \mathcal{J} \left[\bar{u}^{(2)} + \bar{\alpha}^{(1)} \sin \bar{\alpha} \right], \quad (\bar{N} \sin \bar{\alpha})^{(1)} = \mathcal{J} \left[\bar{v}^{(2)} - \bar{\alpha}^{(1)} \cos \bar{\alpha} \right]. \quad (37)$$

Next, using the balance of angular momentum, yielding the moment-shear relation with finite-extension effect, in Eq. (30), the bending constitutive relation in Eq. (34), and the definition of α in Eq. (5), and making use of Eq. (27)₁, we obtain:

$$\bar{S} \sin \bar{\alpha} = -\bar{\kappa} \bar{M}^{(1)} \sin \bar{\alpha} = -\bar{\kappa} \bar{\alpha}^{(2)} \sin \bar{\alpha}, \quad \bar{S} \cos \bar{\alpha} = -\bar{\kappa} \bar{\alpha}^{(2)} \cos \bar{\alpha}. \quad (38)$$

$$-(\bar{S} \sin \bar{\alpha})^{(1)} = -\left(-\bar{\kappa} \bar{\alpha}^{(2)} \sin \bar{\alpha}\right)^{(1)} = \left[\bar{\kappa} \bar{\alpha}^{(2)}\right]^{(1)} \sin \bar{\alpha} + \left[\bar{\kappa} \bar{\alpha}^{(2)}\right] \bar{\alpha}^{(1)} \cos \bar{\alpha} \quad (39)$$

$$+(\bar{S} \cos \bar{\alpha})^{(1)} = \left(-\bar{\kappa} \bar{\alpha}^{(2)} \cos \bar{\alpha}\right)^{(1)} = -\left[\bar{\kappa} \bar{\alpha}^{(2)}\right]^{(1)} \cos \bar{\alpha} + \left[\bar{\kappa} \bar{\alpha}^{(2)}\right] \bar{\alpha}^{(1)} \sin \bar{\alpha}. \quad (40)$$

Using Eq. (37) for the derivative of the terms with $(\bar{N}, \bar{\alpha})$, and Eqs. (39)-(40) for the derivative of the terms with $(\bar{S}, \bar{\alpha})$ in Eq. (28), the non-dimensionalized balance of linear momenta, we obtain the equations of motion in terms of the displacements (u, v) .

Axial equation of motion:

$$\mathcal{J} \left[\bar{u}^{(2)} + \bar{\alpha}^{(1)} \sin \bar{\alpha} \right] + \left[\bar{\kappa} \bar{\alpha}^{(2)} \right]^{(1)} \sin \bar{\alpha} + \left[\bar{\kappa} \bar{\alpha}^{(2)} \right] \bar{\alpha}^{(1)} \cos \bar{\alpha} + \bar{f}_X = \ddot{\bar{u}}, \quad (41)$$

Transversal equation of motion:

$$\mathcal{J} \left[\bar{v}^{(2)} - \bar{\alpha}^{(1)} \cos \bar{\alpha} \right] - \left[\bar{\kappa} \bar{\alpha}^{(2)} \right]^{(1)} \cos \bar{\alpha} + \left[\bar{\kappa} \bar{\alpha}^{(2)} \right] \bar{\alpha}^{(1)} \sin \bar{\alpha} + \bar{f}_Y = \ddot{\bar{v}}, \quad (42)$$

where the slenderness \mathcal{J} was defined in Eq. (32)₁, and $\bar{\kappa}$ in Eq. (27), Eq. (26), and Eq. (7), reproduced here so all relevant terms in the above equations of motion are grouped together for convenience:

$$\mathcal{J} := \frac{AL^2}{I}, \quad (32)$$

$$\bar{\kappa} = \left\{ \left[1 + \bar{u}^{(1)} \right]^2 + \left[\bar{v}^{(1)} \right]^2 \right\}^{-1/2}. \quad (43)$$

2.1.5 Input parameters: Boundary and initial conditions, distributed load

In addition to the slenderness \mathcal{J} defined in Eq. (32) and the input distributed load functions $\bar{f}_X(\bar{X}, \bar{t})$ and $\bar{f}_Y(\bar{X}, \bar{t})$ for Eqs. (41)-(42), respectively, i.e.,

$$\bar{f}_X(\bar{X}, \bar{t}) = \hat{f}_X(\bar{X}, \bar{t}), \quad \bar{f}_Y(\bar{X}, \bar{t}) = \hat{f}_Y(\bar{X}, \bar{t}), \quad (44)$$

there are six input parameters in each of the two sets of boundary conditions considered here: One set for cantilever beam, and another for simply-supported beam.

Cantilever beam

Clamped end: Three input parameters are the prescribed displacements and rotation $\{\widehat{u}, \widehat{v}, \widehat{\alpha}\}$, such that

$$\text{At } \bar{X} = 0, \quad \bar{u}(\bar{X} = 0, \bar{t}) = \widehat{u}, \quad \bar{v}(0, \bar{t}) = \widehat{v}, \quad \bar{\alpha}(0, \bar{t}) = \widehat{\alpha}. \quad (45)$$

Free end: Three input parameters, two algebraic expressions with derivatives (AEDs).

$$\text{At } \bar{X} = 1, \quad s\bar{e}(1, \bar{t}) = \widehat{N}, \quad -\bar{k}(1, \bar{t})\bar{M}^{(1)}(1, \bar{t}) = -\bar{k}(1, \bar{t})\bar{\alpha}^{(2)}(1, \bar{t}) = \widehat{S}, \quad \bar{\alpha}^{(1)}(1, \bar{t}) = \widehat{M}. \quad (46)$$

The three input parameters in Eq. (46) are the prescribed concentrated forces and moment $\{\widehat{N}, \widehat{S}, \widehat{M}\}$, and the two AEDs are Eqs. (46)_{1,2} due to the expression of \bar{e} as a result of Eqs. {(5), (6), (26), (27)₂}, and the expression of \bar{k} in Eq. (43), with both \bar{e} and \bar{k} involving the first-order derivatives $\bar{u}^{(1)}$ and $\bar{v}^{(1)}$. These AEDs together with the differential equations from the balance of momenta form a system of differential-algebraic equations (DAEs).

Simply-supported beam

$$\text{At } \bar{X} = 0, \quad \bar{u}(0, \bar{t}) = \widehat{u}_0, \quad \bar{v}(0, \bar{t}) = \widehat{v}_0, \quad \bar{\alpha}^{(1)}(0, \bar{t}) = \widehat{M}_0. \quad (47)$$

$$\text{At } \bar{X} = 1, \quad s\bar{e}(1, \bar{t}) = \widehat{N}_1, \quad \bar{v}(1, \bar{t}) = \widehat{v}_1, \quad \bar{\alpha}^{(1)}(0, \bar{t}) = \widehat{M}_1. \quad (48)$$

Because of the expression for \bar{e} in Eq. (48)₁, the equations of motion of the simply-supported beam also form a system of DAEs.

Remark 2.1. *AEDs cannot be imposed exactly.* Because “complex” boundary conditions are AEDs, such as Eq. (48)₁, which involve derivatives of the dependent variables, they cannot be imposed exactly by hard constraints. Only “simple” boundary conditions not involving derivatives of dependent variables, such as Eqs.(48)_{2,3}, can be imposed exactly. ■

There are four prescribed functions for the four initial conditions:

$$\bar{u}(\bar{X}, 0) = \widetilde{u}_0(\bar{X}), \quad \dot{\bar{u}}(\bar{X}, 0) = \widetilde{\dot{u}}_0(\bar{X}), \quad (49)$$

$$\bar{v}(\bar{X}, 0) = \widetilde{v}_0(\bar{X}), \quad \dot{\bar{v}}(\bar{X}, 0) = \widetilde{\dot{v}}_0(\bar{X}). \quad (50)$$

2.2 Inconsistency, reduction from geometrically-exact beam with shear

Deformation map of centroidal line [19], which is valid for both geometrically-exact beam without shear (Figure 1) and with shear (Figure 2, is written as:

$$\phi_0(X, t) = [X + u(X, t)] \mathbf{e}_1 + v(X, t) \mathbf{e}_2, \quad (51)$$

where $\{\mathbf{e}_1, \mathbf{e}_2\}$ are the spatial basis vectors. The material basis vectors $\{\mathbf{t}_1, \mathbf{t}_2\}$ attached to the cross section are then in terms of the rotation θ of the cross section

$$\mathbf{t}_1(X, t) = \cos \theta(X, t) \cdot \mathbf{e}_1 + \sin \theta(X, t) \cdot \mathbf{e}_2, \quad \mathbf{t}_2(X, t) = -\sin \theta(X, t) \cdot \mathbf{e}_1 + \cos \theta(X, t) \cdot \mathbf{e}_2. \quad (52)$$

$$\begin{Bmatrix} \mathbf{t}_1 \\ \mathbf{t}_2 \end{Bmatrix} = \begin{bmatrix} \cos \theta & \sin \theta \\ -\sin \theta & \cos \theta \end{bmatrix} \begin{Bmatrix} \mathbf{e}_1 \\ \mathbf{e}_2 \end{Bmatrix} =: \mathbf{\Lambda}^T \begin{Bmatrix} \mathbf{e}_1 \\ \mathbf{e}_2 \end{Bmatrix}. \quad (53)$$

Spatial strains $\{\gamma_1, \gamma_2\}$ and material strain $\{\Gamma_1, \Gamma_2\}$; see Figure 2:

$$\begin{Bmatrix} \gamma_1 \\ \gamma_2 \end{Bmatrix} = \begin{Bmatrix} 1 + u^{(1)} - \cos \theta \\ v^{(1)} - \sin \theta \end{Bmatrix} = \begin{Bmatrix} (1 + e) \cos \alpha - \cos \theta \\ (1 + e) \sin \alpha - \sin \theta \end{Bmatrix}, \quad \begin{Bmatrix} \Gamma_1 \\ \Gamma_2 \end{Bmatrix} = \mathbf{\Lambda}^T \begin{Bmatrix} \gamma_1 \\ \gamma_2 \end{Bmatrix}. \quad (54)$$

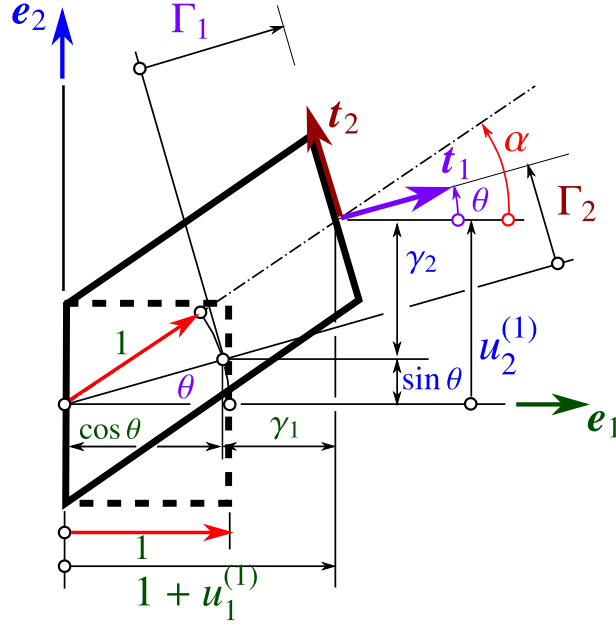


Figure 2: *Geometrically-exact beam with shear deformation.* The deformed configuration (solid line) is superposed on the initial configuration (dotted line) of unit length (which could be multiplied by dX). Shear deformation is the difference between the angle α of the deformed centroidal line and the rotation θ of the cross section. Spatial strains $\{\gamma_1, \gamma_2\}$ and material strains $\{\Gamma_1, \Gamma_2\}$, such that $\gamma = \gamma_1 e_1 + \gamma_2 e_2 = \Gamma_1 t_1 + \Gamma_2 t_2$. See [19] and Figure 1 for geometrically-exact beam with no shear.

Next, using Eq. (4) in Eq. (54), we obtain

$$\begin{Bmatrix} \gamma_1 \\ \gamma_2 \end{Bmatrix} = \begin{Bmatrix} (1+e) \cos \alpha - \cos \theta \\ (1+e) \sin \alpha - \sin \theta \end{Bmatrix}, \quad (55)$$

and in the case where $\theta = \alpha$, we have

$$\begin{Bmatrix} \gamma_1 \\ \gamma_2 \end{Bmatrix} = e \begin{Bmatrix} \cos \alpha \\ \sin \alpha \end{Bmatrix}, \quad \begin{Bmatrix} \Gamma_1 \\ \Gamma_2 \end{Bmatrix} = \mathbf{\Lambda}^T \begin{Bmatrix} \gamma_1 \\ \gamma_2 \end{Bmatrix} = \begin{Bmatrix} e \\ 0 \end{Bmatrix}, \quad (56)$$

which indicates that there is zero shear deformation, and thus zero shear force S , since the material (axial and shear) forces $\{N_1, N_2\} = \{N, S\}$ are computed from the linear constitutive relation [19] as follows:

$$\begin{Bmatrix} N_1 \\ N_2 \end{Bmatrix} = \begin{bmatrix} EA & 0 \\ 0 & GA_s \end{bmatrix} \begin{Bmatrix} \Gamma_1 \\ \Gamma_2 \end{Bmatrix} = \begin{Bmatrix} EAe \\ 0 \end{Bmatrix} = \begin{Bmatrix} N \\ S \end{Bmatrix}. \quad (57)$$

But a non-zero shear force S was introduced in Figure 1 and in the balance of linear momenta to derive the equations of motion as done above.

Remark 2.2. The authors of [19] cited (among other references) [20], where neither the dynamic problem, nor the computational formulation, was considered. It is also noted that the static “Form 4” in [20] was the result of a projection onto the cross-section basis vectors $\{t_1, t_2\}$, whereas the dynamic Form 4 (Section 3.6) considered here remains in the inertial frame. ■

2.3 Small deformation, Euler-Bernoulli

For small axial deformation $e \ll 1$, which includes inextensibility $e = 0$, the moment-shear relation in Eq. (13) is approximated as

$$e \ll 1 \Rightarrow 0 = \frac{dM}{dX} + S, \quad (58)$$

which is the classical relation between moment and shear.

For small slope α and small axial strain $u^{(1)}$, the slope of the centroidal line can be approximated as the slope of the transverse displacement using Eq. (5), i.e.,

$$\alpha < 10^\circ \text{ (small angle) and } u^{(1)} \ll 1 \Rightarrow \alpha \approx v^{(1)} = s_v \Rightarrow \bar{\alpha} \approx \bar{v}^{(1)} = \bar{s}_v. \quad (59)$$

From Eq. (26)₅ on the space-derivative of the transverse displacement, the slope of the deformed centroidal line can be written as

$$s_v(X, t) := \frac{\partial v(X, t)}{\partial X} = v^{(1)}(X, t), \quad \bar{s}_v(\bar{X}, \bar{t}) := \frac{\partial \bar{v}(\bar{X}, \bar{t})}{\partial \bar{X}} = \bar{v}^{(1)}(\bar{X}, \bar{t}), \quad s_v(X, t) = \bar{s}_v(\bar{X}, \bar{t}), \quad (60)$$

and thus the space derivative of the slope is:

$$s_v^{(1)} = \frac{\partial v^{(1)}}{\partial X} = \frac{\partial \bar{X}}{\partial X} \frac{\partial \bar{v}^{(1)}}{\partial \bar{X}} = \frac{1}{L} \bar{s}_v^{(1)}, \quad (61)$$

again using Eq. (26)₅.

Non-dimensional constitutive relations for bending deformation using Eq. (8), Eq. (19), Eq. (34), Eq. (59), and Eq. (61):

$$M = EIs_v^{(1)} = v^{(2)} \Rightarrow \bar{M} = \bar{s}_v^{(1)} = \bar{v}^{(2)}, \quad (62)$$

which is the moment-curvature relation for the Euler-Bernoulli beam.

For the axial equation of motion in Eq. (41), the small-angle approximation in Eq. (59) together with the near-zero slope approximation:

$$\alpha \approx 0 \Rightarrow \sin \alpha \approx 0 \text{ and } \cos \alpha \approx 1, \quad (63)$$

lead to the standard axial equation of motion with distributed load:

$$\mathcal{J} \bar{u}^{(2)} + \bar{f}_X \approx \ddot{\bar{u}}. \quad (64)$$

Without applied axial distributed load, the axial Eq. (64) becomes the standard 1-D wave equation:

$$\mathcal{J} \bar{u}^{(2)} = \ddot{\bar{u}} \Rightarrow \bar{u}^{(2)} = \bar{u}^{(2)}, \quad (65)$$

with the square-root of the slenderness, i.e., $\sqrt{\beta}$, as the non-dimensionalized wave speed. The more slender (i.e., the less rotund) the bar is, the faster the wave propagates along the axial direction.

For the transverse equation of motion in Eq. (42), the approximations in Eq. (59) (small angle) and Eq. (63) (near-zero slope) lead to:

$$\mathcal{J} [\bar{v}^{(2)} - \bar{\alpha}^{(1)} \cos \bar{\alpha}] \approx 0, \quad [\bar{k} \bar{\alpha}^{(2)}] \bar{\alpha}^{(1)} \sin \bar{\alpha} \approx 0, \quad - [\bar{k} \bar{\alpha}^{(2)}]^{(1)} + \bar{f}_Y \approx \ddot{\bar{v}}, \quad (66)$$

which, upon using the approximation $\bar{k} \approx 1$ together with the small-angle approximation in Eq. (59), leads to the standard Euler-Bernoulli beam equation of motion with fourth space derivative on the transverse displacement \bar{v} :

$$-\bar{v}^{(4)} + \bar{f}_Y \approx \ddot{\bar{v}}. \quad (67)$$

Eq. (64) and Eq. (67) form the system of non-dimensionalized PDEs that describes the dynamics of small-

deformation Euler-Bernoulli beam.

3 PINN formulations

Several forms of the equations of motion of the Kirchhoff rod—starting from the lower level (Form 1) to the higher level (Form 4)—are provided below with significant consequences on the corresponding PINN implementation and computational efficiency.

3.1 Inputs

$$\text{Inputs: } \mathcal{J} := \frac{AL^2}{I} \quad (32), \quad \bar{f}_X(\bar{X}, \bar{t}) = \hat{f}_X(\bar{X}, \bar{t}), \quad \bar{f}_X(\bar{X}, \bar{t}) = \hat{f}_X(\bar{X}, \bar{t}) \quad (44)$$

3.2 Form 1: No operator splitting

Form 1: No operator splitting

$$\mathcal{J} \left[\bar{u}^{(2)} + \bar{\alpha}^{(1)} \sin \bar{\alpha} \right] + \left[\bar{\kappa} \bar{\alpha}^{(2)} \right]^{(1)} \sin \bar{\alpha} + \left[\bar{\kappa} \bar{\alpha}^{(2)} \right] \bar{\alpha}^{(1)} \cos \bar{\alpha} + \bar{f}_X = \ddot{\bar{u}}, \quad (41)$$

$$\mathcal{J} \left[\bar{v}^{(2)} - \bar{\alpha}^{(1)} \cos \bar{\alpha} \right] - \left[\bar{\kappa} \bar{\alpha}^{(2)} \right]^{(1)} \cos \bar{\alpha} + \left[\bar{\kappa} \bar{\alpha}^{(2)} \right] \bar{\alpha}^{(1)} \sin \bar{\alpha} + \bar{f}_Y = \ddot{\bar{v}}, \quad (42)$$

$$\tan \bar{\alpha} = \frac{\bar{v}^{(1)}}{1 + \bar{u}^{(1)}} \quad (36), \quad \bar{\kappa} = \left\{ \left[1 + \bar{u}^{(1)} \right]^2 + \left[\bar{v}^{(1)} \right]^2 \right\}^{-1/2} \quad (43)$$

Dependent variables: 4

$\{\bar{u}, \bar{v}, \bar{\alpha}\}, \bar{\kappa}$.

In principle, the number of dependent variables could be reduced from 4 to 3 by substituting the expression for $\bar{\kappa}$ in Eq. (43) into the balance of linear momenta in Eqs. (41)-(42). Due to the space derivative on $\bar{\kappa}$, it would be simpler and computationally more efficient to use Form 1 above to avoid complex expressions and multiple computations of the derivatives $\bar{u}^{(1)}$ and $\bar{v}^{(1)}$.

Similarly, while it is possible to further reduce the number of dependent variables from 3 to 2, because of the derivative $\bar{\alpha}^{(1)}$, it is simpler and more efficient to use Form 1 above, while paying attention to avoid multiple computation of $\sin \bar{\alpha}$ and $\cos \bar{\alpha}$.

Remark 3.1. *Form 1, pinned-pinned bar: Time shift and early stopping.* A characteristic of Form 1 is the floating/shifting computed time history when there is convergence in the optimization process. Time shift examples are shown in Figures 20 and 21 for the axial motion of a pinned-pinned elastic bar; see Eq. (85) for the definition of the pinned boundary conditions.

Another characteristic of Form 1 is “early stopping,” i.e., the lowest loss value occurs well before the end of the optimization process (see, e.g., [1]), which may diverge for large learning rates, and which could be *stopped earlier*. See Remark 5.18 and examples therein. ■

Remark 3.2. *Form 1, pinned-free bar: Static solution.* For sufficiently large learning rate, a static solution could manifest in the training process; see Remark 5.19. ■

3.3 Form 2a: Split time derivatives

Form 2a: Split only time derivatives to reduce to first order.

$$\mathcal{J} \left[\bar{u}^{(2)} + \bar{\alpha}^{(1)} \sin \bar{\alpha} \right] + \left[\bar{\kappa} \bar{\alpha}^{(2)} \right]^{(1)} \sin \bar{\alpha} + \left[\bar{\kappa} \bar{\alpha}^{(2)} \right] \bar{\alpha}^{(1)} \cos \bar{\alpha} + \bar{f}_X = \dot{\bar{p}}_X, \quad \dot{\bar{u}} = \bar{p}_X \quad (68)$$

$$\mathcal{J} \left[\bar{v}^{(2)} - \bar{\alpha}^{(1)} \cos \bar{\alpha} \right] - \left[\bar{k} \bar{\alpha}^{(2)} \right]^{(1)} \cos \bar{\alpha} + \left[\bar{k} \bar{\alpha}^{(2)} \right] \bar{\alpha}^{(1)} \sin \bar{\alpha} + \bar{f}_Y = \dot{\bar{p}}_Y, \quad \dot{\bar{v}} = \bar{p}_Y \quad (69)$$

$$\tan \bar{\alpha} = \frac{\bar{v}^{(1)}}{1 + \bar{u}^{(1)}} \quad (36), \quad \bar{k} = \left\{ \left[1 + \bar{u}^{(1)} \right]^2 + \left[\bar{v}^{(1)} \right]^2 \right\}^{-1/2} \quad (43)$$

Dependent variables: 6

$\{\bar{u}, \bar{v}, \bar{\alpha}\}, \bar{k}, \{\bar{p}_X, \bar{p}_Y\}$.

The number of dependent variables could be reduced from 6 to 4 by substituting the expressions for $\bar{\alpha}$ in Eq. (36) and for \bar{k} in Eq. (43) into the balance of linear momenta in Eqs. (68)-(69) at the cost of repetitive evaluations and thus a loss of efficiency.

Remark 3.3. *Form 2a: Static solution.* Under the right conditions, a static solution could occur in Form 2a for both the pinned-pinned bar and the pinned-free bar. Examples are given in Remark 5.20 with methods to avoid the static solution mentioned. Static solution could also be found in Form 1 for the pinned-free bar; see Remark 3.2, Remark 5.19. ■

3.4 Form 2b: Split space derivatives

Form 2b: Split only space derivatives to reduce to first order.

$$\mathcal{J} \left[\bar{s}_u^{(1)} + \bar{\alpha}^{(1)} \sin \bar{\alpha} \right] - \bar{S}^{(1)} \sin \bar{\alpha} - \bar{S} \bar{\alpha}^{(1)} \cos \bar{\alpha} + \bar{f}_X = \ddot{\bar{u}}, \quad (70)$$

$$\mathcal{J} \left[\bar{s}_v^{(1)} - \bar{\alpha}^{(1)} \cos \bar{\alpha} \right] + \bar{S}^{(1)} \cos \bar{\alpha} - \bar{S} \bar{\alpha}^{(1)} \sin \bar{\alpha} + \bar{f}_Y = \ddot{\bar{v}}, \quad (71)$$

$$\bar{u}^{(1)} = \bar{s}_u, \quad \bar{\alpha}^{(1)} = \bar{M}, \quad (72)$$

$$\bar{v}^{(1)} = \bar{s}_v, \quad \bar{M}^{(1)} = -\bar{c} \bar{S}, \quad (73)$$

$$\tan \bar{\alpha} = \frac{\bar{v}^{(1)}}{1 + \bar{u}^{(1)}} \quad (36), \quad \bar{c} = \left\{ \left[1 + \bar{u}^{(1)} \right]^2 + \left[\bar{v}^{(1)} \right]^2 \right\}^{1/2} \quad (7), (27)$$

Dependent variables: 7

$\{\bar{u}, \bar{v}, \bar{\alpha}\}, \bar{c}, \bar{M}, \{\bar{s}_u, \bar{s}_v\}$

3.5 Form 3: Split time and space derivatives

Form 3: Split both time and space derivatives to reduce to first order.

$$\mathcal{J} \left[\bar{s}_u^{(1)} + \bar{\alpha}^{(1)} \sin \bar{\alpha} \right] - \bar{S}^{(1)} \sin \bar{\alpha} - \bar{S} \bar{\alpha}^{(1)} \cos \bar{\alpha} + \bar{f}_X = \dot{\bar{p}}_X, \quad (74)$$

$$\mathcal{J} \left[\bar{s}_v^{(1)} - \bar{\alpha}^{(1)} \cos \bar{\alpha} \right] + \bar{S}^{(1)} \cos \bar{\alpha} - \bar{S} \bar{\alpha}^{(1)} \sin \bar{\alpha} + \bar{f}_Y = \dot{\bar{p}}_Y, \quad (75)$$

$$\bar{u}^{(1)} = \bar{s}_u, \quad \dot{\bar{u}} = \bar{p}_X, \quad \bar{\alpha}^{(1)} = \bar{M}, \quad (76)$$

$$\bar{v}^{(1)} = \bar{s}_v, \quad \dot{\bar{v}} = \bar{p}_Y, \quad \bar{M}^{(1)} = -\bar{c} \bar{S}, \quad (77)$$

$$\tan \bar{\alpha} = \frac{\bar{v}^{(1)}}{1 + \bar{u}^{(1)}} \quad (36), \quad \bar{c} = \left\{ \left[1 + \bar{u}^{(1)} \right]^2 + \left[\bar{v}^{(1)} \right]^2 \right\}^{1/2} \quad (7), (27)$$

Dependent variables: 9

$$\{\bar{u}, \bar{v}, \bar{\alpha}\}, \bar{c}, \bar{M}, \{\bar{p}_X, \bar{p}_Y\}, \{\bar{s}_u, \bar{s}_v\}$$

The number of dependent variables can be reduced from 9 to 8 by substituting the expression for \bar{c} only once in the expression relating moment to shear in Eq. (76)₃, without repetitive computation. On the other hand, further reducing the number of dependent variable from 8 to 7 by substituting the expression for $\bar{\alpha}$ in Eq. (36) into the balance of linear momenta Eqs. (74)-(75) would be inefficient due to repetitive computation of $\bar{\alpha}$.

3.6 Form 4: Balance of momenta with no substitution

Form 4: Balance of momenta with first-order derivatives.

$$\bar{N}_X^{(1)} - \bar{S}_X^{(1)} + \bar{f}_X = \dot{\bar{p}}_X, \quad \bar{N}_Y^{(1)} + \bar{S}_Y^{(1)} + \bar{f}_Y = \dot{\bar{p}}_Y \quad (78)$$

$$\bar{N}_X = \mathcal{J} \left[1 + \bar{u}^{(1)} - \cos \bar{\alpha} \right], \quad \bar{S}_X = -\bar{k} \bar{M}^{(1)} \sin \bar{\alpha}, \quad (79)$$

$$\bar{N}_Y = \mathcal{J} \left[\bar{v}^{(1)} - \sin \bar{\alpha} \right], \quad \bar{S}_Y = -\bar{k} \bar{M}^{(1)} \cos \bar{\alpha}, \quad (80)$$

$$\bar{\alpha}^{(1)} = \bar{M}, \quad \dot{\bar{u}} = \bar{p}_X, \quad \dot{\bar{v}} = \bar{p}_Y, \quad (81)$$

$$\tan \bar{\alpha} = \frac{\bar{v}^{(1)}}{1 + \bar{u}^{(1)}} \quad (36), \quad \bar{k} = \left\{ \left[1 + \bar{u}^{(1)} \right]^2 + \left[\bar{v}^{(1)} \right]^2 \right\}^{-1/2} \quad (43)$$

Dependent variables: 11

$$\{\bar{u}, \bar{v}, \bar{\alpha}\}, \bar{k}, \bar{M}, \{\bar{p}_X, \bar{p}_Y\}, \{\bar{N}_X, \bar{N}_Y, \bar{S}_X, \bar{S}_Y\}$$

The number of dependent variables can be reduced from 11 to 9 by substituting the expressions for $\bar{\alpha}$ in Eq. (36) and for \bar{k} in Eq. (43) into the expressions for normal and shear force components (\bar{N}_X, \bar{N}_Y) and (\bar{S}_X, \bar{S}_Y) in Eq. (79)₂ and Eq. (80)₂, respectively. But the repetitive computations of the same quantities (e.g., $\bar{\alpha}$ in four different expressions, and \bar{k} in two different expressions) could make such substitution inefficient.

4 Generic PDEs, auxilliary conditions, loss function

For short, boundary conditions and initial conditions are together referred to as *auxilliary* conditions. The system in all of the above forms $k = 1, \dots, 4$ —PDEs and the associated auxilliary conditions—can be generically written as a series of representative *dynamic* nonlinear differential operators $\mathcal{D}_i^{(k)}$ as follows:

$$\mathcal{D}_i^{(k)}(\{\partial_X^p u_j, \partial_X^{p-1} u_j, \dots, \partial_X^1 u_j\}, \{\partial_t^q u_j, \partial_X^{q-1} u_j, \dots, \partial_t^1 u_j\}, u_j, t) = \mathcal{D}_i^{(k)}(\mathbf{u}(X, t), t) = 0,$$

$$\text{with } k = 1, \dots, 4, \quad i = 1, \dots, n_i^{(k)}, \quad j = 1, \dots, n_j^{(k)}, \quad p = 1, \dots, n_p^{(k)}, \quad q = 1, \dots, n_q^{(k)}, \quad (82)$$

where $u_j(X, t)$ are the dependent variables, and $\partial_X^p u_j(X, t)$ is the p th partial derivative of u_j with respect to X , and similarly for $\partial_t^q u_j(X, t)$. When $n_q^{(k)} = 0$, there are no terms with time derivatives, as in the static case. For convenience, the following dynamic-operator array, which will be used later, is defined:

$$\mathcal{D}^{(k)} = \left\{ \mathcal{D}_i^{(k)}, i = 1, \dots, n_i^{(k)} \right\}, \quad k = 0, \dots, 3. \quad (83)$$

The loss function for Form k to minimize is

$$J^{(k)} = \sum_{i=1}^{i=n_i^{(k)}} w_i^{(k)} \left[\mathcal{D}_i^{(k)} \right]^2, \quad (84)$$

where w_i is the weight associated with the differential operator $\mathcal{D}_i^{(k)}$, for $i = 1, \dots, n_i^{(k)}$, playing the role of an “error” function.

5 Numerical examples

At first, to set up PINN problems of structural dynamics, we opted to use the DeepXDE (abbreviated as “DDE”) framework [2], which was likely the most well-documented open-source software for PINN, with many examples to guide users and a forum for open discussions of problems users encountered. Specifically, since performance depends on the DDE version used, we provide this information. In the present paper, we use DDE v1.9.2 or v1.9.3 with the TensorFlow backend, which together is abbreviated as, e.g., DDE-T v1.9.3, or simply **DDE-T**, since DDE v1.9.3 is mostly used in this paper.³

In using **DDE-T**, we encountered many problems such as shift and amplification in the dynamic solution, static-solution time history, in addition to the difficulty in designing appropriate learning-rate schedules, mostly by trial-and-error and accumulated experience that we want to convey to readers, to arrive at good solutions. Along the way, we devised various strategies to solve these pathological problems, such as different forms of the governing PDE system to solve the shift and amplification problem, and the barrier function to avoid static solutions. Even then, a significant amount of time was devoted to get these methods to work, compared to our script based on the **JAX** framework, the *High-Performance Array Computing* by GoogleMind, which did not manifest any of these pathological problems; see Remarks 5.10, 5.19.

Since **DDE-T** is accessible to the public, the detailed documentation of the **DDE-T** pathological problems, our proposed solutions and results, would not only be useful for the general readers, but also for the developers.

Because of the large number of parameters, resulting in many different cases, and to allow for convenient, frequent back-referencing in figure captions and elsewhere in the text, the sections below are organized as a series of remarks, each addressing a specific issue/topic with immediate reference to the corresponding figures/results for illustration where applicable.⁴

Remark 5.1. *Colab GPU time.* Even though we did use a dedicated Linux machine with Nvidia GPU (Graphics Processing Units) for script development, all results presented here were obtained using **Google Colab**’s Nvidia Tesla K80 GPU with 12 GB RAM (free). See the GPU time in, e.g., Figure 15. ■

Remark 5.2. *RunID.* At the end of the caption of a figure, there is a RunID, such as “23723R1d-1,” to indicate which run produced that figure: (two images): “23723” being the date 2023 Jul 23, “R1d” being “Run 1d,” the order of the DeepXDE script file executed on that date, and “-1” being the first figure (two images) coming from that run, from which the final result in Figure 21 with RunID 23723R1d-4 (Step 200,000) is presented in the paper body, Section 5.3.1 to illustrate the time shift in Form 1 (Remark 5.17, Section 5.3.1).

³For example, Figure 12, RunID 23726R5c-1, was obtained with “deepxde-1.9.2 pyaml-23.7.0 scikit-optimize-0.9.0”, whereas Figure 22, RunID 2394R1a-1, was obtained with “deepxde-1.9.3 pyaml-23.9.1 scikit-optimize-0.9.0”. In the follow-up paper, we will report a significant GPU time difference between DDE-T v1.10.0 and DDE-T v1.10.1.

⁴The remarks are important integral parts of the text. It is recommended, particularly for readers not familiar with PINN and its training process, not to skip, but to read through all remarks so to be familiar with the corresponding illustrative examples on the remark topics. The ultimate objective is to solve nonlinear PDEAs, after developing an experience with the training process using **DDE-T** and **JAX** to solve standard linear PDEs using the proposed novel PINN formulations through a normalization/standardization presented in this paper.

A reason for introducing the RunID is because, even though “stochastically reproducible,” the results are “deterministically irreproducible,” unless we run under deterministic mode, which is slower, as explained in Remark 5.15. For this reason, we kept a large majority of the executed scripts (run under non-deterministic mode), the results from a small number of which are presented here. ■

5.1 Network architecture, data-point grids

Remark 5.3. *Computational-domain, network variables, dynamic results.* To shortened the description, the following parameter symbols are used. For bars and beams, the domain for the space coordinate x is the interval $[0, 1]$, the domain for time coordinate is $[0, T]$, and the rectangular space-time *computational domain* is $[0, 1] \times [0, T]$, with N being the number of data points on one of its sides. The data points, with a total number of $N \times N$, are used to evaluate the loss functions. For the network architecture, n_{inp} is the number of inputs, W the width of a hidden layer, H the number of hidden layers, and n_{out} the number of outputs.

Network inputs: For static problems, $n_{\text{inp}}=1$ (for the data-point x -coordinates), whereas for dynamic problems, $n_{\text{inp}}=2$ (for the data point (x, t) coordinates). Since the value of n_{inp} is clear from the context, it will not be listed in figure captions; see, e.g., Figure 34.

Network outputs: The number of dependent variables of the PDE(s) depends on the Form used. For example, Form 4 of the Kirchhoff-Love rod (Section 3.6) has $n_{\text{out}}=11$ outputs; see, e.g., Figure 34 for Form 2a of a pinned-pinned bar, with $n_{\text{out}}=2$.

For results related to dynamic problems, the phrase “time history” is omitted in figure captions for conciseness, since the meaning is clear from the context. For example, in Figure 34, the shape (left) and the midspan displacement (right) are time histories, with the shape having “x1” as the space x axis and “x2” the time t axis, which is also the horizontal axis of the midspan displacement. ■

Remark 5.4. *Total parameters of dense networks.* As an example, Form 1 of the axial motion of a pinned-pinned elastic bar (Section 5.3.1) and a network with $n_{\text{inp}}=2$ inputs (x, t) , $W=64$ neurons per hidden layer, $H=4$ hidden layers, $n_{\text{out}}=1$ output $u(x, t)$ lead to 12,737 parameters (weights and biases), Figure 3, obtained as follows.

From the 2 inputs to the 64 neurons in hidden layer 1, there are 64×2 weights (connections) and 64 biases, thus in total $(64 \times 2 + 64) = 192$ parameters. From hidden layer 1 to hidden layer 2, there are 64×64 weights (connections) and 64 biases, thus in total $(64 \times 64 + 64) = 1460$ parameters.

Similarly for the two subsequent pairs of hidden layers, the number of weights and biases is 1460 per pair, thus in total $(64 \times 64 + 64) \times 3 = 12480$ parameters for all three pairs of hidden layers. From the hidden layer 4 to the one output layer, there are 64×1 weights (connections) and 1 bias, thus in total $(64 + 1) = 65$ parameters. Summing up, there are 12,737 parameters (weights and biases) in total, Figure 3.

In the model-summary output of the DeepXDE framework [2], Figure 3, the term “layer” is used to designate “layer of connections,” which is formed by two “layers of neurons” as used here, and the type of connections mentioned above is termed “dense,” i.e., each neuron in the 1st layer is connected to all neurons in the 2nd layer. ■

Remark 5.5. *Data-point grids.* For the evaluation of the loss functions. We essentially used three types of grids: Regular grid, fixed-random grid, and varying-random grid.

For a *regular* grid with $N \in \{11, 21, 31, 41, 51\}$ as the number of points⁵ on, say one side of the space-time domain $[0, 1] \times [0, T]$, containing the space-time point (x, t) with $x \in [0, 1]$ and $t \in [0, T]$,

⁵ Meaning, the number N of points could take any value in the set $\{11, 21, 31, 41, 51\}$, with 51 as the default number in the normalization (or standardization) of the presentation of our results. To alleviate the notation, we also omit the overbar on (\bar{x}, \bar{t}) to write simply as (x, t) .

Model: "fnn"

Layer (type)	Output Shape	Param #
dense (Dense)	multiple	192
dense_1 (Dense)	multiple	4160
dense_2 (Dense)	multiple	4160
dense_3 (Dense)	multiple	4160
dense_4 (Dense)	multiple	65

=====

Total params: 12,737
Trainable params: 12,737
Non-trainable params: 0

Figure 3: [DDE-T](#). *Pinned-pinned elastic bar, axial motion*. Model summary. Feedforward neural network (fnn). Remark 5.4. Section 5.3.1, Form 1. Dense-connection layers, each between two consecutive layers of neurons. *Network:* Remark 5.3, $n_{\text{inp}}=2$, $W=64$, $H=4$, $n_{\text{out}}=1$, 12737 parameters. Six neuron layers (1 input, 4 hidden, 1 output), five connection layers (pairs of consecutive neuron layers). (23721R1-1)

where for example $T \in \{2, 4, 8\}$, there is an even number of intervals on each side (space or time), i.e., $\{10, 20, 30, 40, 50\}$, respectively, with $N \times N$ as the total number of data points, such that one data point is at the center of the space-time domain. Figure 34 shows the shape (left) and midspan-displacement (right) time histories of the axial motion of pinned-pinned elastic bar using Form 2a (Section 5.3.2), a model with N51 W64 H4, having 12,802 parameters, a regular grid, and $\text{init_lr}=0.001$. By default, $N = 51$ is used when the value of N is not mentioned in a figure caption. Figure 29 shows a static solution obtained using [DDE-T](#) with Form 2a, the same network and number of parameters and regular grid, but with an $\text{init_lr}=0.01$ (ten times larger). Figure 40 shows good shape and midspan displacement using Form 3 (Section 5.3.4), a model with N51 W32 H2, having 1,251 parameters, and a regular grid.

For a *random* grid, $N \times N$ data points are randomly distributed in the space-time (x, t) domain, while ensuring that (1) there are N randomly distributed points along the time (t) axis for each of the two boundary locations $x = 0$ and $x = 1$, and (2) there are N randomly distributed points on the space (x) axis for the initial time $t = 0$. A *fixed* random distribution is always generated with the seed 42 [21] so to obtain the same pseudo-random N points for every execution. For a *varying* random grid, no seed is used.

As an example of a random grid, see Figure 35, which corresponded to one of the lowest total loss $0.537\text{e-}06$ for Form 2a. Two reruns of the same exact script that produced Figure 35 yielded the total loss of $0.626\text{e-}06$ (RunID 2384R2b) and $0.518\text{e-}06$ (RunID 2384R2c), both at Step 192,000, respectively. Figure 36 shows that stopping earlier at Step 146,000 at which the total loss of $7.22\text{e-}06$ was lowest in Cycle-4, with quasi-perfect midspan displacement and GPU time 442 sec, is a good trade-off. To give more information, the loss function was shown in Figure 36, since the random grid is similar to that in Figure 35. An even better trade-off is given in Figure 39, with a total loss of $1.179\text{e-}06$, a quasi-perfect midspan displacement with $\text{damping}\%=0.1\%$ and GPU time 278 sec. For an additional example of random grids, see also Figures 42-44.

Switching from a regular grid to a *random* grid, while keeping all other parameters the same, could lower the total loss; see Remark 5.9 on “Extended learning-rate schedule” (ELRS) for an example. ■

5.2 Training (optimization) learning-rate scheduling.

The Adam optimizer is used in all examples in the present paper, with learning-rate decay over N_{steps} , the total number of steps, which is divided into n_{cycles} , the number of decay cycles, each of which contains $n\text{-steps}_{\text{cycle}}$, the number of steps per cycle. This $n\text{-steps}_{\text{cycle}}$ may vary from cycle to cycle, and is subdivided into n_{periods} , the number of decay periods, each of which contains $n\text{-steps}_{\text{period}}$, the number of steps per

period; see Figure 4. This $n\text{-steps}_{\text{period}}$ is generally fixed when compiling a model with decay, with the $n\text{-steps}_{\text{cycle}}$ chosen as a multiple of $n\text{-steps}_{\text{period}}$.

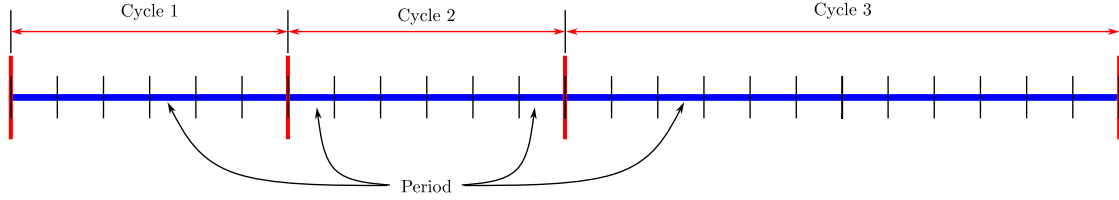


Figure 4: Optimization learning-rate scheduling. Section 5.2. Cycles and periods.

After an initial-learning rate for a number of cycles was chosen, e.g., $\text{init_lr} = 0.001$, in any given period (p) within a cycle, the learning rate $\epsilon_{(p-1)}$ at the end of the previous period (p-1) is decayed to the value $\epsilon_{(p)} = \ell_{\text{decay}} \cdot \epsilon_{(p-1)}$, with ℓ_{decay} being a decay factor less than one, following a decay function, such as the “inverse time” function.

After each cycle and at the beginning of the subsequent cycle, the learning rate is reset to the initial-learning rate, similar to cyclic annealing, for which a detailed explanation can be found in [1].

As an example, we could set in a cycle $n\text{-steps}_{\text{cycle}} = 50,000$, $n\text{-steps}_{\text{period}} = 2,500$, so that $n_{\text{periods}} = 20$, and $\ell_{\text{decay}} = 0.9$.

The number of cycles n_{cycles} and the total number of steps N_{steps} vary depending on the convergence properties of an execution. With $n\text{-steps}_{\text{cycle}} = 50,000$ and $n\text{-steps}_{\text{period}} = 2,500$, we could set $n_{\text{cycles}} = 4$ and $N_{\text{steps}} = 200,000$ to “run all” these cycles one after another at once, or we could also set $n\text{-steps}_{\text{cycle}} = 25,000$ then run only the first cycle to examine the solution obtained to decide whether to stop (in the case of reaching a static solution in a dynamic problem, as shown in Figure 48 right and Figure 49 left) or to continue the optimization process, possibly with different values for $n\text{-steps}_{\text{cycle}}$, n_{cycles} , and N_{steps} .

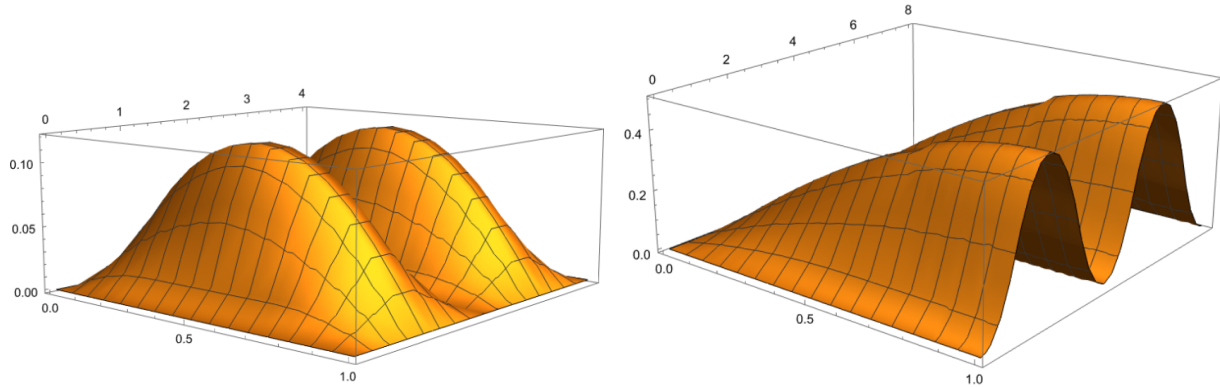


Figure 5: Axial motion of elastic bar. Section 5.3. Mathematica solutions. Eq. (64) with slenderness $\beta = 1$ and distributed load $\bar{f}_X = 1/2$. Two vibration periods for each set of boundary conditions. *Left:* Pinned-pinned bar, with $\bar{X} \in [0, 1]$ and $\bar{t} \in [0, 4]$. *Right:* Pinned-free bar, with $\bar{X} \in [0, 1]$ and $\bar{t} \in [0, 8]$.

Remark 5.6. *Learning-rate schedule 1 (LRS 1).* Cyclic annealing (CA) with same learning rate. To allow for a systematic comparison of the PINN results, LRS 1 is set to consist of $n_{\text{cycles}} = 5$ cycles, with Cycles 1 and 2 having $n\text{-steps}_{\text{cycle}} = 25,000$ steps, totaling 50,000 steps at the end of cycle 2, whereas Cycles 3, 4, 5, each has $n\text{-steps}_{\text{cycle}} = 50,000$ steps, making a total of $N_{\text{steps}} = 200,000$ steps over these 5 cycles. Computational results (loss function, deformed shape, GPU time) would be gathered at the end of these

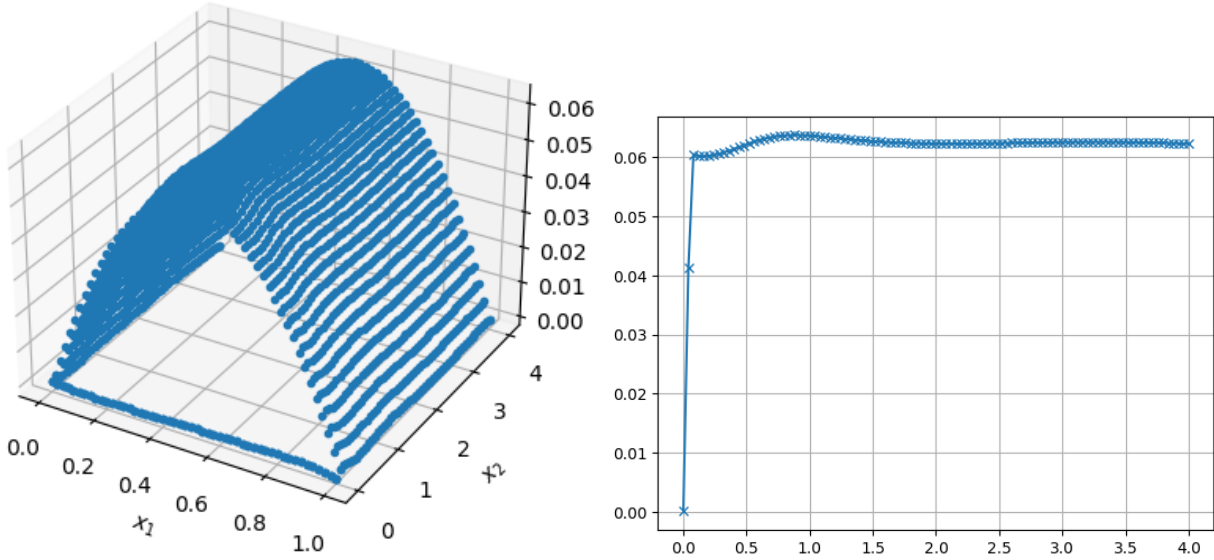


Figure 6: DDE-T. Pinned-pinned bar, cyclic annealing (CA). Static-shape (left), static midspan displacement (right), Step 50,000. ★ Section 5.3.2, Form 2a. Remarks 3.3 (Static solution), 5.20 (How to avoid). Network: ★ Remarks 5.3, 5.5, $T=4$, $W=32$, $H=2$, $n_{out}=2$, He-uniform initializer, 1,218 parameters, regular grid. Training: ★ Remark 5.6, LRS 1, $init_lr=0.07$, $n_cycles=2$, $N_steps=50,000$. ● Figure 7, NCA, same model and $init_lr=0.07$, waves, damping. ▷ Figure 5, reference solution to compare. (23817R10a-1)

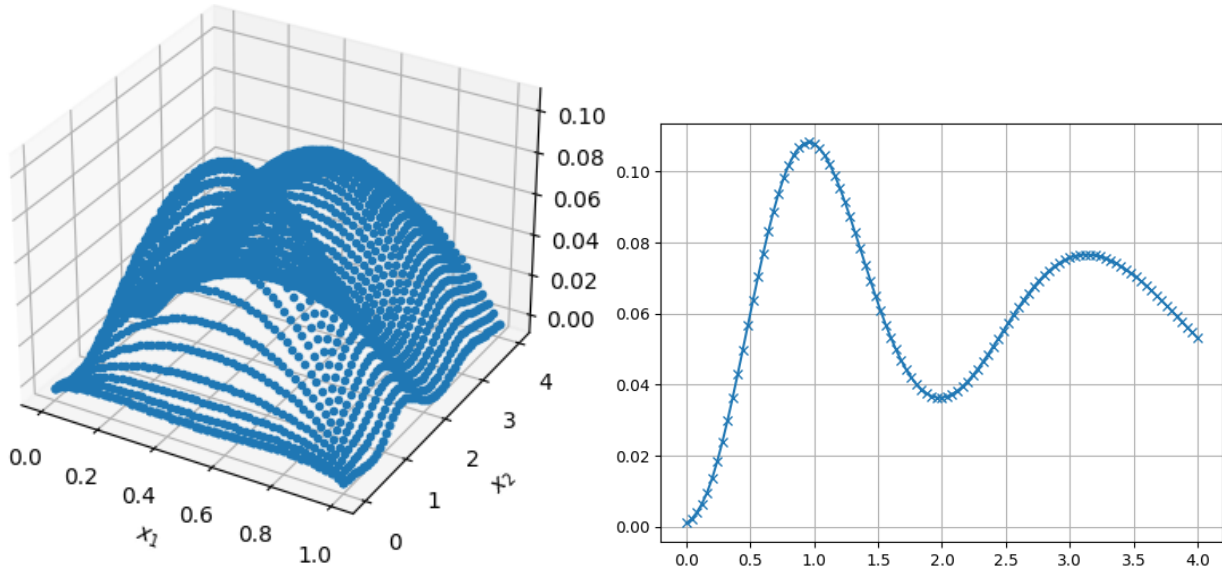


Figure 7: DDE-T. Pinned-pinned bar, No cyclic annealing (NCA). Shape (left), midspan displacement (right), Step 50,000, waves with damping. ★ Section 5.3.2, Form 2a. Remark 5.14, Damping. Network: ★ Remarks 5.3, 5.5, $T=4$, $W=32$, $H=2$, $n_{out}=2$, He-uniform initializer, 1,218 parameters, regular grid. Training: Remark 5.8, LRS 3, $init_lr=0.07$, $n_cycles=2$, $N_steps=50,000$. ● Figure 6, CA, same model and $init_lr=0.07$, static solution. Figures 10 (Form 2a, 1,218 parameters), 40-41 (Form 3, 1,251 parameters), VCA, low damping. Figures 42-44, Form 3, 1,251 parameters, random grid, quasi-perfect solution. (23817R10b-1)

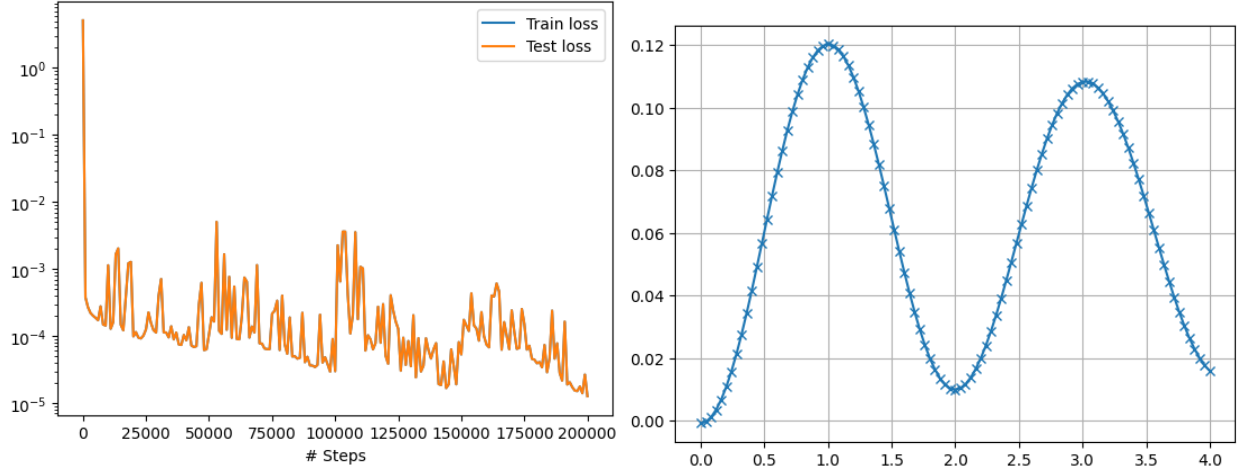


Figure 8: DDE-T. Pinned-pinned bar, cyclic annealing (CA). Loss function (left), midspan displacement, Step 200,000 (right), waves with damping. ★ Section 5.3.2, Form 2a. Network: ★ Remarks 5.3, 5.5, $T=4$, $W=64$, $H=2$, $n_{\text{out}}=2$, He-uniform initializer, 4,482 parameters, ★ regular grid. Training: ★ Remark 5.6, LRS 1 (CA), $\text{init_lr}=0.03$. ● Figure 9, 1,218 parameters, CA, $\text{init_lr}=0.04$, static solution. ▷ Figure 5, reference solution to compare. (23815R3b-1) ● The train-loss history in blue coincides with the test-loss history in orange, and is not visible in the plot. The same situation occurs in subsequent loss-history figures.

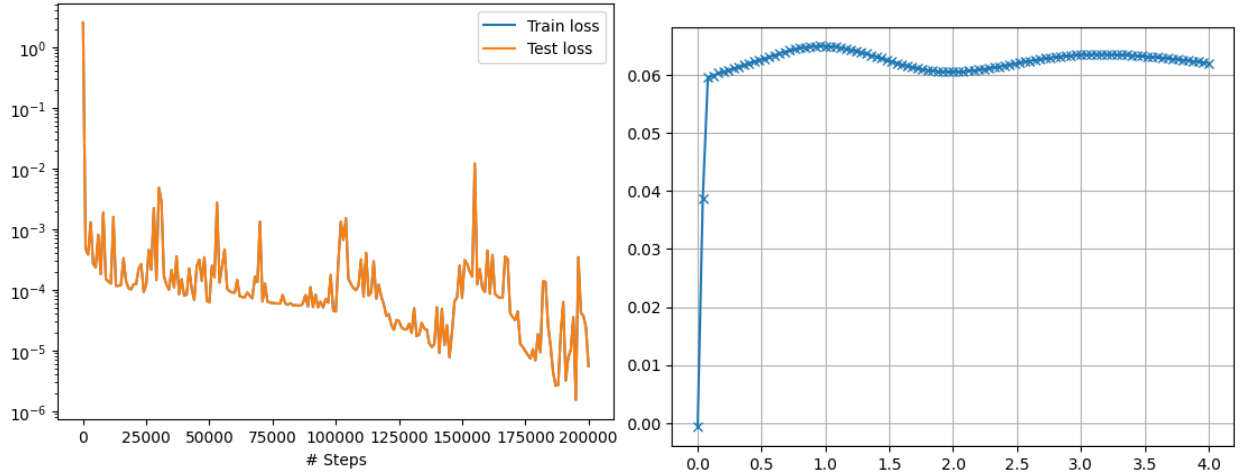


Figure 9: DDE-T. Pinned-pinned bar, cyclic annealing (CA). Loss function (left), midspan displacement, Step 200,000 (right), static solution. ★ Section 5.3.2, Form 2a. Network: ★ Remarks 5.3, 5.5, $T=4$, $W=32$, $H=2$, $n_{\text{out}}=2$, He-uniform initializer, 1,218 parameters, ★ regular grid. Training: ★ Remark 5.6, LRS 1 (CA), $\text{init_lr}=0.04$. ● Figure 8, 4,482 parameters, CA, $\text{init_lr}=0.03$, waves, damping. Figure 10, VCA, Form 2a, same model, waves, small damping. (23813R4b-1)

5 cycles. Each period is kept at a constant $n\text{-steps}_{\text{period}} = 2,500$ steps, and has a learning-rate decay to $\ell_{\text{decay}} = 90\%$ by inverse time.⁶

Any deviation from the LRS 1 would be clearly indicated. For example, we may run a case using only two cycles, $n\text{-cycles}=2$, $\text{init_lr}=0.07$, and then stop the execution after $N\text{-steps}=50,000$, such as in Figure 6.

Using **DDE-T**, while CA led to waves with damping as in Figure 8 (4,482 parameters, $\text{init_lr}=0.03$, regular grid), but CA could also lead to a static solution as in Figure 6 and Figure 9 (1,218 parameters, $\text{init_lr}=0.04$, regular grid). For the counterpart with “no cyclic annealing” (NCA), see Remark 5.8 on LRS 3.

It is important to note that the static solution is one of the pathological problems we encountered with using **DDE-T** (Figure 27), but did not appear when using **JAX** (Figure 28); see Remarks 5.10, 5.19.

A characteristic of CA is the jump in the loss function after each resetting of the initial learning rate at the beginning of each cycle; see the left subfigures of Figures 8-9. ■

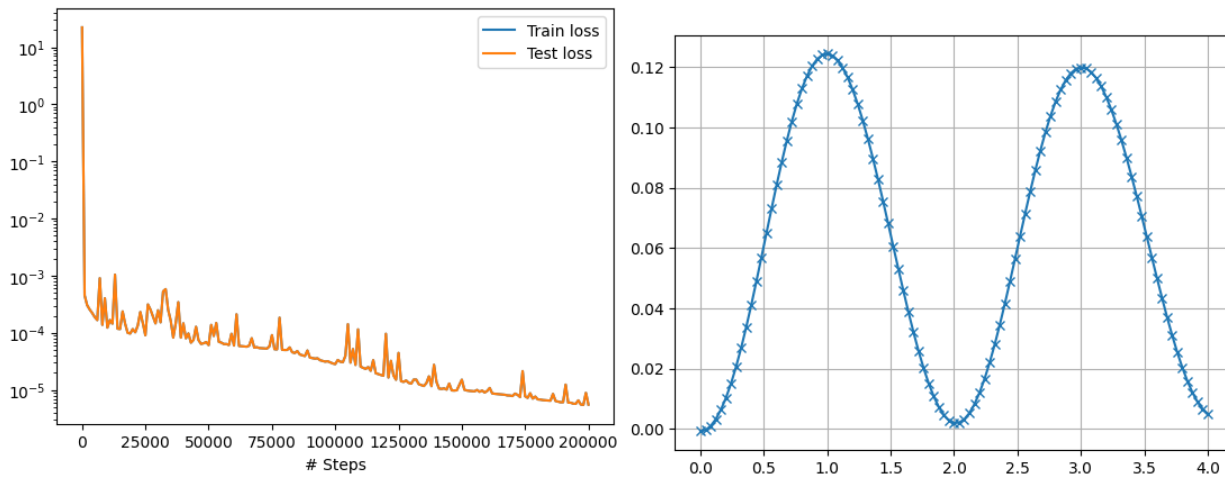


Figure 10: **DDE-T**. Pinned-pinned bar, Varying init_lr cyclic annealing (VCA). Loss function (left), midspan displacement (right), Step 200,000, waves, small damping. Section 5.3.2, Form 2a. ★ Remark 5.14, Damping. Network: Remarks 5.3, 5.5, $T=4$, $W=32$, $H=2$, $n_{\text{out}}=2$, He-uniform initializer, 1,218 parameters, regular grid. Training: ★ Remark 5.7, LRS 2 (VCA), $\text{init_lr}=[0.04, 0.03, 0.02, 0.01, 0.005]$. ● Figure 9, CA, Form 2a, same model, $\text{init_lr}=0.04$, static solution. ▷ Figure 40, VCA, Form 3, same model and init_lr sequence, waves, small damping. ▷ Figure 5, reference solution to compare. (23821R1a-1)

Remark 5.7. Learning-rate schedule 2 (LRS 2). Varying initial-learning-rate cyclic annealing (VCA). Each cycle has its own learning rate, which may (or may not) vary in the subsequent cycles. An example would be to use the same parameters as in LRS 1 (Remark 5.6), except for the different initial learning rate at the beginning of each cycle as prescribed by the list $\text{init_lr} = [0.02, 0.02, 0.02, 0.01, 0.005]$, with decreasing initial learning rates, such that $\text{init_lr} = 0.02$ is used for Cycle 1, 2, 3, $\text{init_lr} = 0.01$ for Cycle 4, and $\text{init_lr} = 0.005$ for Cycle 5.

Figure 10, VCA with Form 2a, Figures 40-41, VCA with Form 3, the same model as in Figure 9 (N51 W32 H2, 1,218 parameters, regular grid), and init_lr sequence $[0.04, 0.03, 0.02, 0.01, 0.005]$ led to waves with small damping. ■

⁶The learning rate at the end of a period is equal to 90% of the learning rate at the beginning of that period.

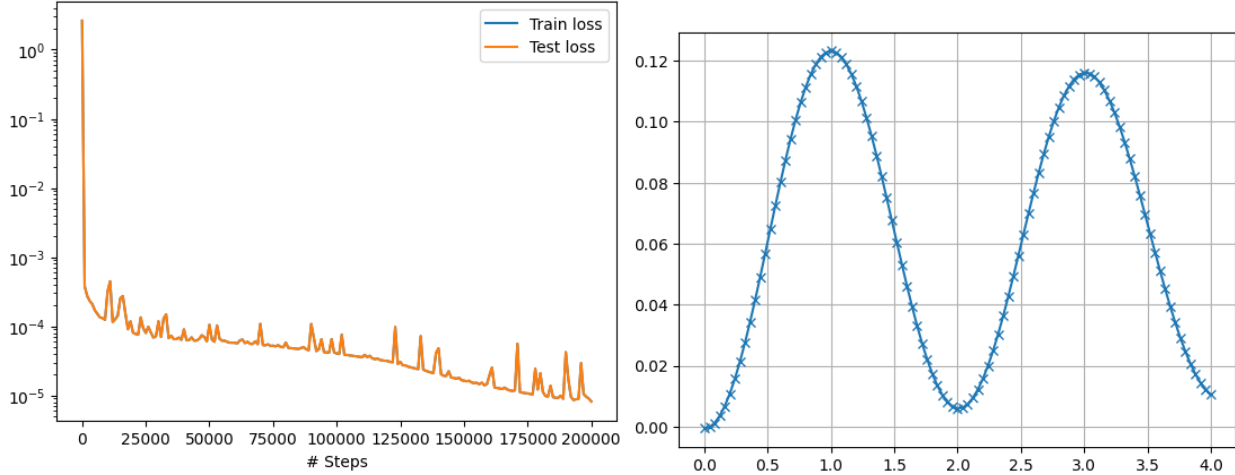


Figure 11: *DDE-T. Pinned-pinned bar, NO cyclic annealing (NCA). Loss function (left), midspan displacement, Step 200,000 (right), waves with damping. ★ Section 5.3.2, Form 2a. Network: ★ Remarks 5.3, 5.5, $T=4$, $W=32$, $H=2$, $n_{\text{out}}=2$, He-uniform initializer, 1,218 parameters, ★ regular grid. Training: ★ Remark 5.8, LRS 3 (NCA), $\text{init_lr}=0.04$. ● Figure 9, CA, same model, static solution. Figure 32, NCA, model with 4,482 parameters, static solution. ▷ Figure 5, reference solution to compare. (23813R4a-1)*

Remark 5.8. *Learning-rate schedule 3 (LRS 3). No cyclic annealing (NCA), i.e., no resetting of the learning rate at the beginning of each cycle, unlike LRS 1 in Remark 5.6. The number of cycles are just breakpoints to plot intermediate results. For example, a training with $n_{\text{cycles}}=1$ and $N_{\text{steps}}=200,000$ correspond to one breakpoint at Step 200,000, whereas a training with $n_{\text{cycles}}=5$ and $N_{\text{steps}}=200,000$ has five breakpoints. The initial learning rate init_lr set at the beginning of Cycle 1 decreases with inverse-time decay without being reset to init_lr at the beginning of each subsequent cycle—unlike LRS 1 in Remark 5.6 and LRS 2 in Remark 5.7— $n_{\text{steps_period}}=2500$, $\ell_{\text{decay}} = 0.9$, and N_{steps} set to either 25,000, 50,000, 100,000, or 200,000 steps for standardization.*

Figure 7, model with N51 W32 H2, having 1,218 parameters, shows waves with damping in the midspan displacement at Step 50,000 when using NCA with $\text{init_lr}=0.07$.

Figure 11, NCA with $\text{init_lr}=0.04$ and a model having 1,218 parameters led to waves with damping. Figure 32, NCA with $\text{init_lr}=0.03$ and a model having 4,482 parameters led to static solution. To avoid the static solution, reduce the initial learning rate init_lr for the same model capacity, or reduce the model capacity (with a possible increase in initial learning rate as done in Figure 11); see Remark 5.13. ■

Remark 5.9. *Extended learning-rate schedule (ELRS).* In some examples, N_{steps} may be extended beyond 200,000, such as 400,000. The extension could be in CA mode (Remarks 5.6-5.7) or in NCA mode (Remark 5.8).

In NCA mode, the learning rate simply continues to decay from the end of Cycle 5 without being reset. Doing so is equivalent to extend $n_{\text{steps_cycle}}$ for Cycle 5 from 50,000 steps to 250,000 steps. This Cycle 5 extension is applicable to both LRS 1 in Remark 5.6 and LRS 2 in Remark 5.7. An example of Cycle-5 extension for Form 2a and a low-capacity model N51 W32 H2 with 1,218 parameters is given in Figure 12, loss function and shape time history at Step 400,000; Figure 13, midspan-displacement time histories at Step 200,000 and at Step 300,000; Figure 14, velocity and *quasi-perfect* midspan-displacement time histories at Step 400,000. The loss function in Figure 12, together with the midspan-displacement time histories in Figures 13-14 gives an idea of the gradual improvement of the solution during the optimization process.

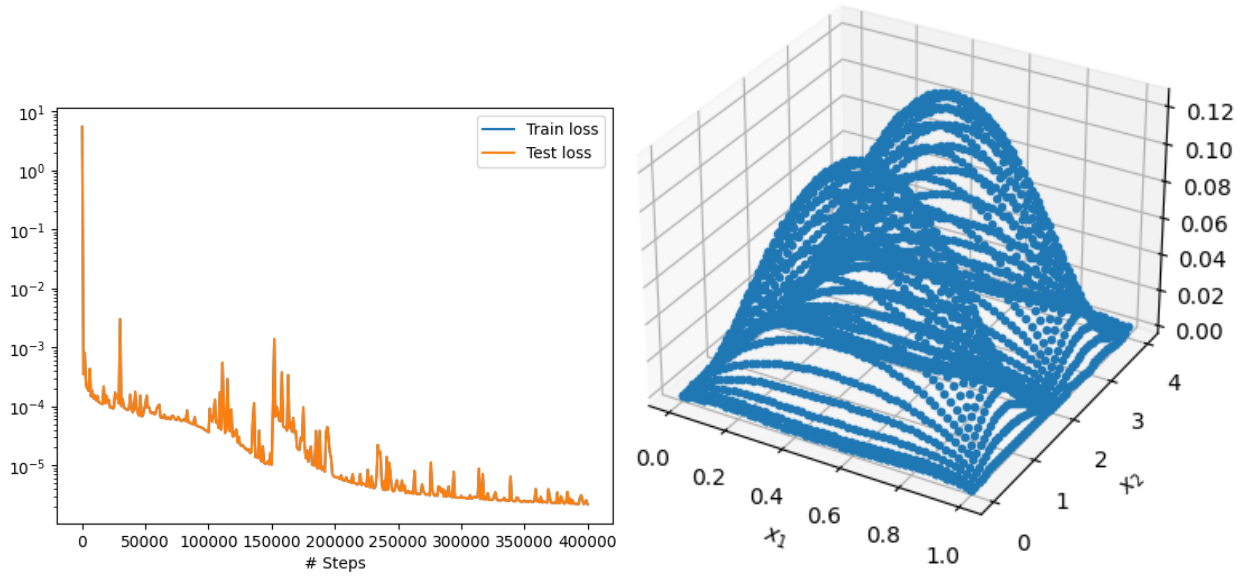


Figure 12: DDE-T. Pinned-pinned bar, Extended learning-rate schedule (ELRS). Loss function (left), shape, Step 400,000 (right). ★ Section 5.3.2, Form 2a. Network: ★ Remarks 5.3, 5.5, $T=4$, $W=32$, $H=2$, $n_{\text{out}}=2$, He-uniform initializer, 1,218 parameters, ★ *regular* grid. Training: ★ Remarks 5.6 (LRS 1), 5.9 (ELRS), $\text{init_lr}=0.02$, Cycles 1-5 (CA), Cycles 6-9 (NCA), $N_{\text{steps}}=400,000$. ★ Lowest total loss $2.19\text{e-}06$, Step 400,000 (sum of 6 losses). ● Figure 13, midspan displacements, Steps 200,000 & 300,000. Figure 14, velocity, *very-good* midspan displacement, Step 400,000. ▷ Figure 5, reference solution to compare. (23726R5c-1)

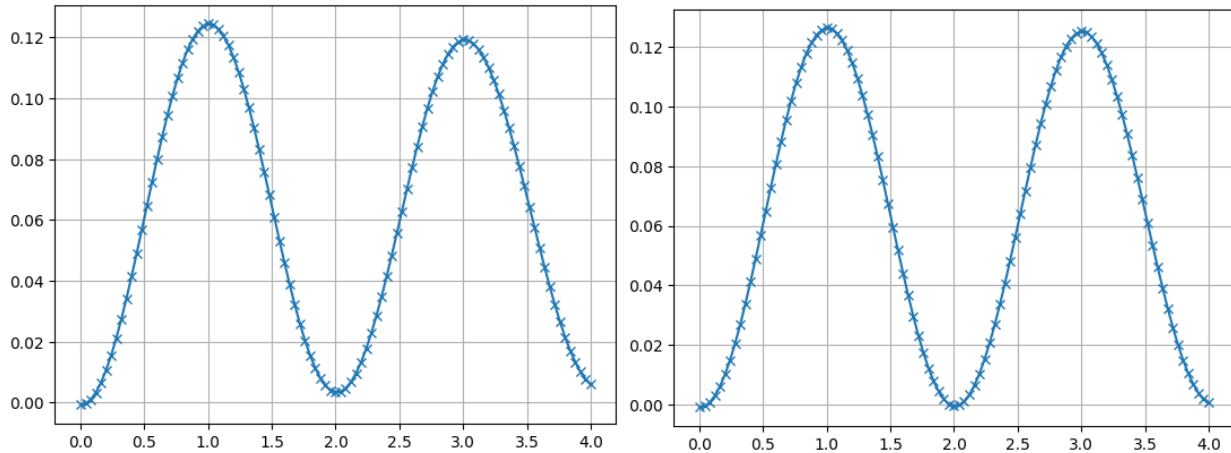


Figure 13: DDE-T. Pinned-pinned bar, ELRS. Midspan displacements: Step 200,000 (left), Step 300,000 (right). Section 5.3.2, Form 2a. Network: ★ Remarks 5.3, 5.5, $T=4$, $W=32$, $H=2$, $n_{\text{out}}=2$, He-uniform initializer, 1,218 parameters, ★ *regular* grid. Training: ★ Remarks 5.6 (LRS 1), 5.9 (ELRS), $\text{init_lr}=0.02$, $n_{\text{cycles}}=9$, Cycles 1-5 (CA), Cycles 6-9 (NCA), $N_{\text{steps}}=400,000$. ● Figure 12, loss function, shape, Step 400,000. Figure 14, velocity, *very-good* solution, Step 400,000. (23726R5c-2)

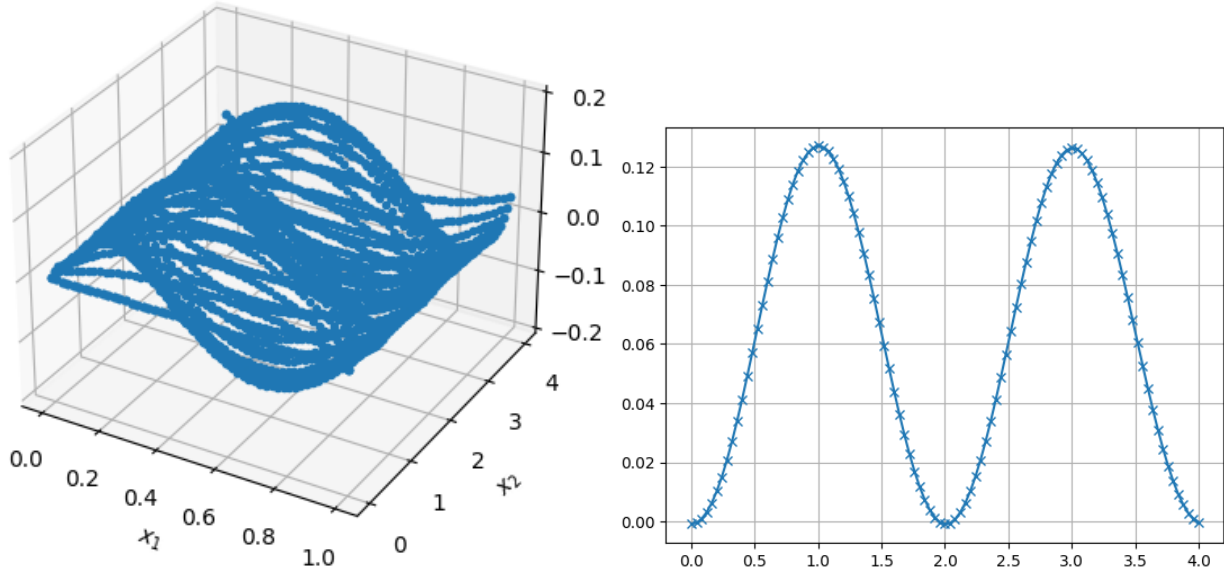


Figure 14: **DDE-T.** Pinned-pinned bar, ELRS. Velocity (left) and **very-good** midspan displacement (right), Step 400,000. ★ Section 5.3.2, Form 2a. Network: ★ Remarks 5.3, 5.5, $T=4$, $W=32$, $H=2$, $n_{\text{out}}=2$, He-uniform initializer, 1,218 parameters, **regular** grid. Training: ★ Remarks 5.6, (LRS 1), 5.9 (ELRS), $\text{init_lr}=0.02$, $n\text{-cycles}=9$, Cycles 1-5 (CA), Cycles 6-9 (NCA), $N_{\text{steps}}=400,000$. ● Figure 12, loss function, shape, Step 400,000. Figure 13, midspan displacements, Steps 200,000 & 300,000. Figure 35, Form 2a, 12,802 parameters, random grid, *quasi-perfect* solution. ▷ Figure 5, reference solution to compare. (23726R5c-3)

The smallest total loss at Step 400,000 was $2.19\text{e-}06$, which was the sum of six losses: PDE, momentum, two boundary conditions, and two initial conditions.

Switching from regular grid to *random* grid, maintaining all other parameters the same, could lower the total loss. For example, using Form 3 with the model N51 W32 H2 having 1,251 params, and init_lr sequence $[0.04, 0.03, 0.02, 0.01, 0.01, 0.005]$ for Cycles 1-6 (VCA), and then Cycles 7-9 (NCA), using a regular grid yielded a total loss of $2.56\text{e-}06$, the sum of seven losses for Form 3, whereas using a random grid yielded a smaller total loss of $1.25\text{e-}06$, both at the same last Step 400,000. ■

Remark 5.10. *Piecewise-constant learning-rate schedule.* (LRS 4) While the inverse-time decay is used in LRS 1 (Remark 5.6), LRS 2 (CA, Remark 5.7), LRS 3 (NCA, Remark 5.8), in our PINN script written using the JAX framework, due to time constraint,⁷ we only implemented the **piecewise-constant schedule** of the Optax gradient processing and optimization library for JAX.

An example of LRS 4 would be: $\text{init_lr}=0.003$, with $\text{factor_lr}=[0.9, 0.8, 0.7, 1, 1]$, so that the learning rate decays as follows: 0.003 in Cycle 1 (up to Step 25,000), $(0.003 * 0.9) = 2.7\text{e-}03$ in Cycle 2 (from Step 25,000+1 to 50,000), $(2.7\text{e-}03 * 0.8) = 2.16\text{e-}03$ in Cycle 3 (from 50,000+1 to 100,000), $(2.16\text{e-}03 * 0.7) = 1.512\text{e-}03$ in Cycle 4 (from 100,000+1 to 150,000), $1.512\text{e-}03$ in Cycle 5 (from 150,000+1 to 200,000), $1.512\text{e-}03$ in Cycle 6 (from 200,000+1 to 250,000).

Hence LRS 4 is also a NCA schedule as LRS 3 (Remark 5.8), and can be extended beyond 200,000 steps as in the above example. Figure 28 depicts the motion of a pinned-free bar under constant distributed

⁷The main reason was the time constraint due to the approaching deadline for this special issue, as we only started developing our JAX script after spending a significant amount of time with DDE-T without satisfactory results, and had our JAX script in working order as the deadline was already looming close. There is no technical reason for not implementing the inverse time decay or any other time decay methods.

axial load (Figure 5) obtained with JAX and LRS 4. See also Remark 5.19, [DDE-T](#) vs [JAX](#), which exhibits none of the [DDE-T](#) pathological problems. ■

Remark 5.11. *Initializer: “He uniform” vs. “Glorot uniform.”* The *He-uniform* initializer is equivalent to a larger learning rate, compared to the *Glorot-uniform* initializer. As a result, the He-uniform initializer may help the training converge faster, but could push the iterate to a static solution, depending on the PDE and its form.

Consider Form 2a of a pinned-free bar, using a network with N51 W64 H4, 12,802 parameters, and the learning-rate scheduling LRS 3 (no cyclic annealing), and init_lr=0.005. Figure 37 uses the *He-uniform* initializer, with regular grid, yielded a *static* solution. Switching from regular grid to random grid (Remark 5.20), keeping the same network architecture and number of data points, i.e., 12,802 parameters, Figure 38, also using the *He-uniform* initializer, yielded a *quasi-perfect* solution.

From the pre-static solution of a pinned-free bar shown in SubFigs 45a-45b obtained with Form 3, He-uniform initializer, and initial learning rate init_lr=0.005, simply switching from He-uniform to Glorot-uniform initializer, which is equivalent to reducing the learning rate (even though init_lr remained at 0.005), resulted in a very-good free-end displacement shown in SubFigs 45g-45h. ■

Remark 5.12. *Rule of thumb for learning rate.* A quick way to assess whether a learning rate would lead to the convergence to a solution (even though the converged solution may not be the one desired), is to run a script with *zero applied force* to see how the optimization converge to the *zero solution*. ■

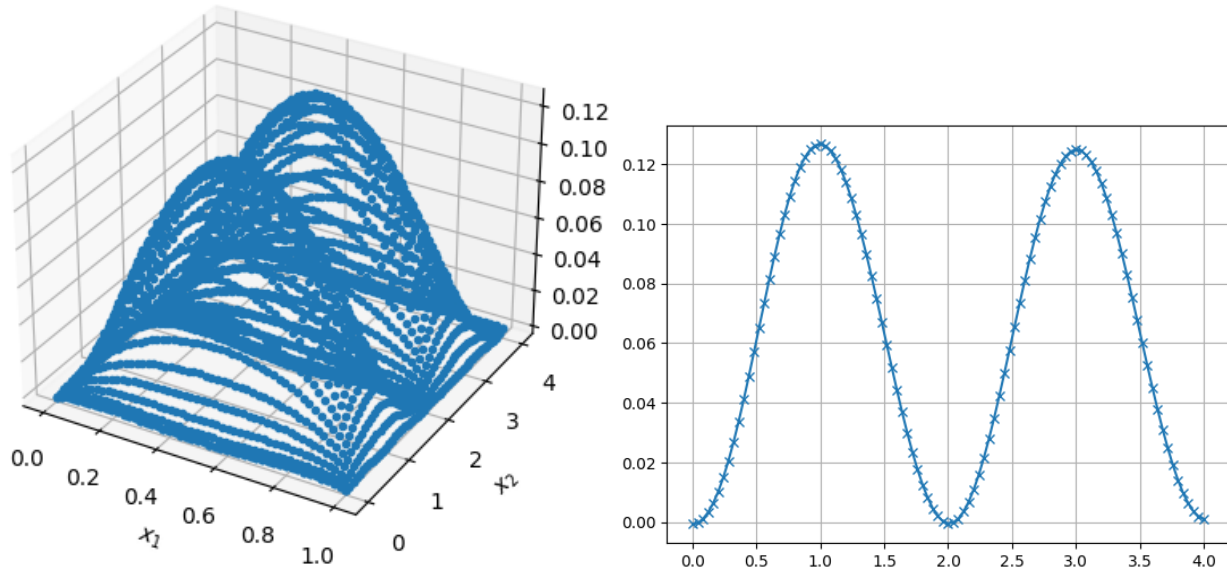


Figure 15: [DDE-T](#). Pinned-pinned bar, lower-capacity network 1. Shape (left), midspan displacement (right), Step 200,000. ★ Remark 5.13, *Optimal capacity*. Remark 5.16, *Unstable solution*. Section 5.3.2, Form 2a. Network: ★ Remarks 5.3, 5.5, T=4, W=64, H=2, n_out=2, He-uniform initializer, 4,482 parameters, ★ regular grid. Training: Remark 5.6 (LRS 1), init_lr=0.01. ★ Lowest loss value 2.12e-06, Step 200,000. Total GPU time 392 sec. ● Figure 34, Form 2a, 12,802 parameters, regular grid, small damping, and Figure 35, random grid, visually *quasi-perfect* solution. Figure 16, Form 2a, 1,218 parameters, regular grid, damping. Figures 42, 43, 44, Form 3, 1,251 parameters, visually *quasi-perfect* solution. ▷ Figure 5, reference solution to compare.

(23816R1a-1)

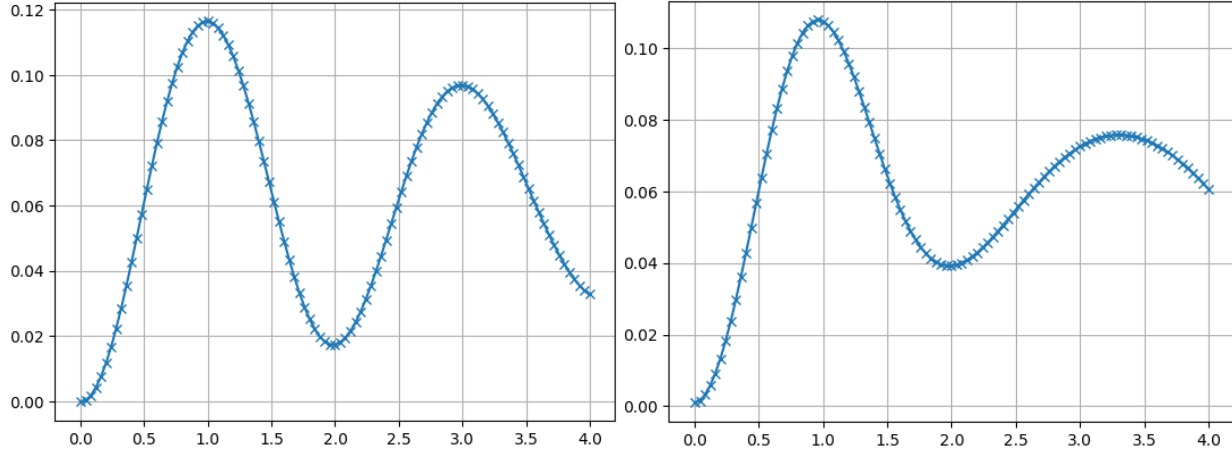


Figure 16: **DDE-T**. Pinned-pinned bar, lower-capacity network 2. Midspan displacement, damping, Step 200,000. ★ Remark 5.13, Optimal capacity. Section 5.3.2, Form 2a. Network: Remark 5.3, 5.5, $T=4$, $W=32$, $H=2$, $n_{\text{out}}=2$, He-uniform initializer, 1,218 parameters, *regular* grid. Training: $\text{init_lr}=0.01$. Left: Remark 5.6, LRS 1 (CA) (23816R2a-1); Right: Remark 5.8, LRS 3 (NCA) (23816R2b-1). ● *Quasi-perfect solutions*: Figure 35, Form 2a, 12,802 parameters, random grid. Figure 15, Form 2a, 4,482 parameters, regular grid; Remark 5.16, *Unstable* solution. Figures 42-44, Form 3, 1,251 parameters, random grid. Figure 14, Form 2a, 1,218 parameters, regular grid.

Remark 5.13. *Optimal network capacity.* Figure 35 shows a *quasi-perfect* solution using the network N51 W64 H4, with 12,802 parameters: Lowest total loss $0.537\text{e-}06$, Step 192,000; Total GPU time 640 sec. A question would be could a network with smaller capacity (fewer parameters) achieve the same (or similar) results? Recall Remark 5.8, in which Figure 11, NCA with $\text{init_lr}=0.04$ and a model having 1,218 parameters led to waves with damping.

Figure 15 shows a much lower-capacity model with roughly one third the number of parameters, namely 4,482, and yet also produced similarly excellent results: Lowest loss value $2.12\text{e-}06$, Step 200,000; Total GPU time 392 sec. Could the model capacity be further reduced?

Figure 16 shows a model with even lower capacity at 1,218 parameters, for which *damping* in the time histories was clearly significant, less damping with cyclic annealing (Remark 5.6, LRS 1), and more damping without cyclic annealing (Remark 5.8, LRS 3). But is it possible to reduce damping and lower the loss value with 1,218 parameters? Yes, indeed, see Figure 42-43: 1,251 parameters; Lowest total loss $1.25\text{e-}06$, Step 400,000; Total GPU time 598 sec; *quasi-perfect* solution.

Of the above three models, the second model with 4,482 parameters is the best for the axial motion of a pinned-pinned bar. See Remark 5.14 on how to avoid damping in low-capacity models using varying initial-learning-rate cyclic-annealing (VCA) (Remark 5.7) and extension of learning-rate schedule (ELRS) (Remark 5.9).

For the pinned-free bar, in Figure 28, the network with N51 W32 H2, with 1,185 parameters, has the optimal capacity, providing low total loss (lowest among these four cases), quasi-perfect damping% in the free-end displacement, and lowest GPU time. ■

Remark 5.14. *Damping in low-capacity models.* For a pinned-pinned bar using Form 2a and a model with N51 W32 H2, having 1,218 parameters, stopping at $N_{\text{steps}}=200,000$, the lowest damping was obtained around the initial learning rate $\text{init_lr}=0.03$, which yielded a ratio of 1st peak to 2nd peak around $0.12 / 0.11 = 1.09$; Figure 17 (shape, midspan displacement, Step 200,000), Figure 18 (loss function, velocity, Step 200,000). Several simulations using this same model and a wide range of initial learning rate, from 0.001

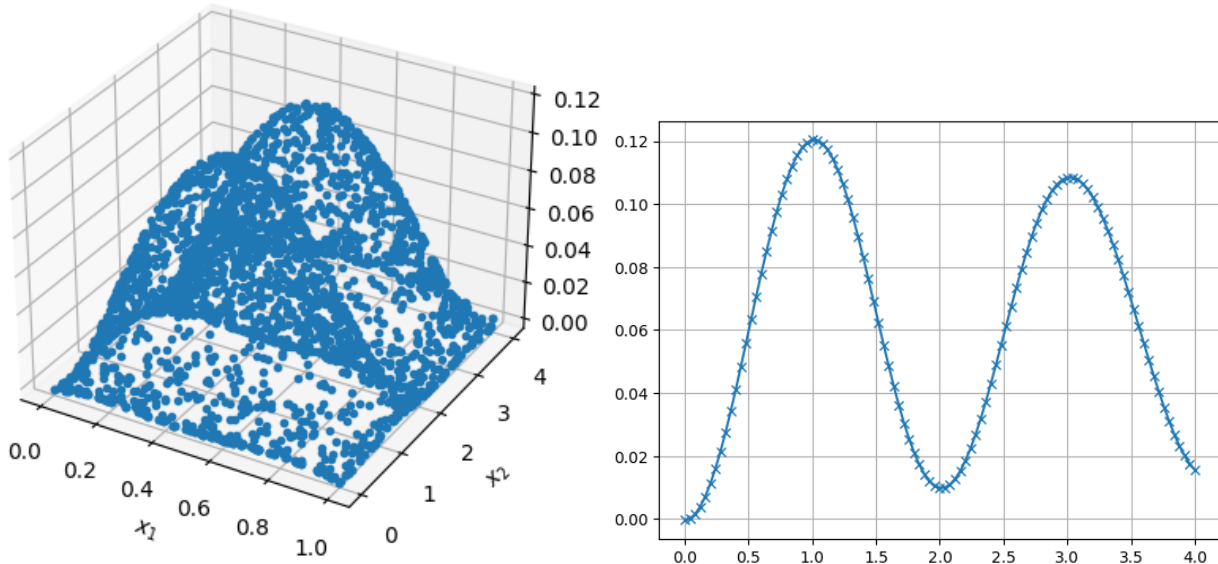


Figure 17: DDE-T. Pinned-pinned bar, damping in low-capacity networks. Shape (left), midspan displacement (right, *damping*), Step 200,000. ★ Remark 5.14, *Damping*. Section 5.3.2, Form 2a. Network: Remarks 5.3, 5.5, $T=4$, $W=32$, $H=2$, $n_{\text{out}}=2$, He-uniform initializer, 1,218 parameters, random grid. Training: Remark 5.6, LRS 1, $\text{init_lr}=0.03$. ● Figure 18, loss function, velocity, Step 200,000. Figure 19, midspan displacements, $\text{init_lr}=0.001$ and $\text{init_lr}=0.1$. ▷ Figure 5, reference solution to compare. (23817R3a-1)

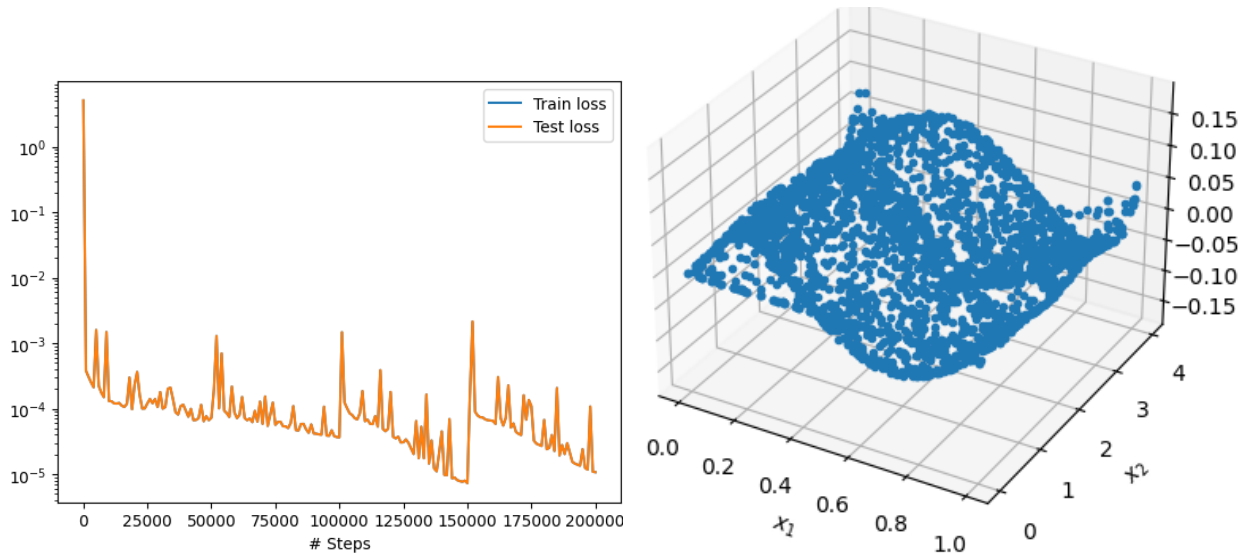


Figure 18: DDE-T. Pinned-pinned bar, damping in low-capacity networks. Loss function (left), velocity (right), Step 200,000. Remark 5.14, *Damping*. ★ Section 5.3.2, Form 2a. Network: Remarks 5.3, 5.5, $T=4$, $W=32$, $H=2$, $n_{\text{out}}=2$, He-uniform initializer, 1,218 parameters, random grid. Training: ★ Remark 5.6, LRS 1, $\text{init_lr}=0.03$. ● Figure 17, shape, midspan displacement, Step 200,000. Figure 19, midspan displacements, $\text{init_lr}=0.001$ & $\text{init_lr}=0.1$. (23817R3a-2)

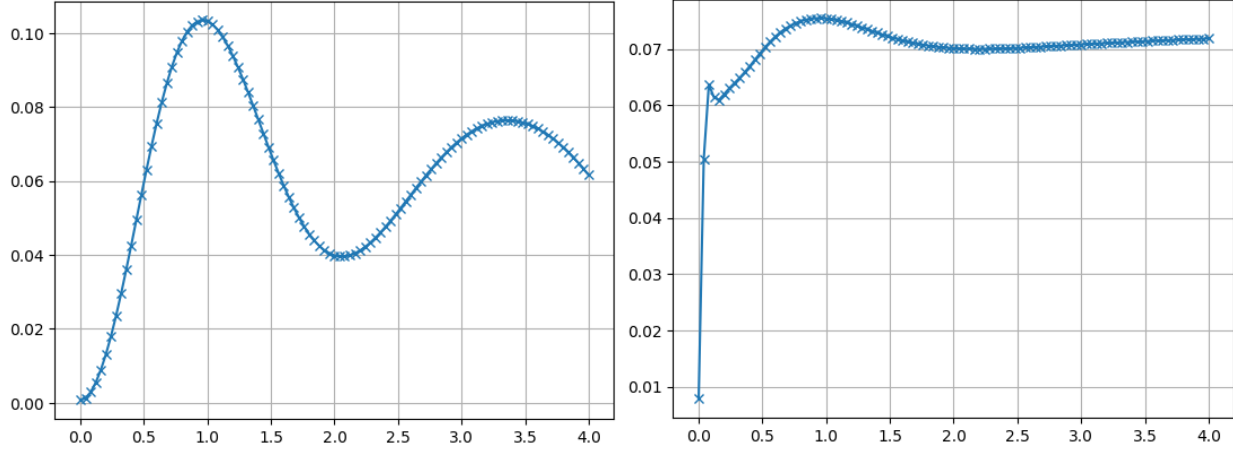


Figure 19: **DDE-T**. Pinned-pinned bar, damping in low-capacity networks. *Left:* Waves, damping, Step 200,000. *Right:* Static solution, Step 50,000. ★ Remark 5.14, Damping. Section 5.3.2, Form 2a. Network: Remarks 5.3, 5.5, $T=4$, $W=32$, $H=2$, $n_{\text{out}}=2$, He-uniform initializer, 1,218 parameters, random grid (left), regular grid (right). Training: ★ Left: Remark 5.6, LRS 1, $\text{init_lr}=0.001$ (23817R2-1). Right: Remark 5.8, LRS 3, $\text{init_lr}=0.1$, $n\text{-cycles}=2$, $N\text{-steps}=50,000$ (23817R11-1).

(Figure 19, left) to 0.1 (Figure 19, right), damping was inescapable in the results. Note that the damping with the smaller $\text{init_lr}=0.001$ was more pronounced than the damping with the 30 times larger $\text{init_lr}=0.03$.

So at first, *damping* appeared to be a characteristic of low-capacity models with $N\text{-steps}$ below 200,000 until we tried the varying initial-learning-rate cyclic annealing (VCA) mentioned in Remark 5.7 and Figure 10 (Form 2a, 1,218 parameters), and Figures 40-41 (Form 3, 1,251 parameters), yielding much lower damping compared to that in Figure 17 and Figure 19, left.

Damping can further reduced after VCA scheduling by extension of learning-rate scheduling (ELRS) to, say, Step 400,000. An example is given in Figures 42-44, Form 3, 1,251 parameters, random grid, *quasi-perfect* solution. See also Remark 5.16, Unstable solution for another example of VCA-ELRS leading to *quasi-perfect* solution. ■

Remark 5.15. *Stochastic reproducibility.* The results are only reproducible in the stochastic sense, i.e., the results could vary a little, even though qualitatively similar, when rerunning the same identical DeepXDE script, with exactly the same parameters. There are several sources of stochasticity: (1) The stochastic optimization initializer, i.e., either “Glorot uniform” or “He uniform” [1] (2) the density and probabilistic distribution of the data points in the (random) grid for the evaluation of the loss function. In other words, the results while stochastically reproducible are *deterministically irreproducible*.

DDE-T allows for setting the `random_seed` to a number, such as “42” (see *fixed random grid* in Remark 5.5), in its configuration to produce *deterministically reproducible* results at the cost of slowing down the computation, and therefore this setting should be used only for debugging.⁸ As an example, using the same model with 4,482 parameters and 200,000 steps as in Figure 15 resulted in a 10% increase in computational time. See Remark 5.23 regarding the opposite for our **JAX** script, for which the deterministic mode is more efficient than the non-deterministic mode, an unexpected surprise.⁹ ■

⁸For **DDE-T**, see the function definition `def set_random_seed(seed)` in **Source code for deepxde.config**, and the command `dde.config.set_random_seed(42)` is used for determinism.

⁹For **JAX**, the commands `os.environ["XLA_FLAGS"] = "--xla_gpu_deterministic_ops=true"` and `key = jax.random.PRNGKey(42)` are used for determinism.

Remark 5.16. *Unstable solution and method to fix.* Sometimes, the solution could be unstable in the sense that it could not be hardly be recovered as if it occurred by chance such as that in Figure 15, which could never again be reproduced. Rerunning the exact same script again several times, from which Figure 15 was obtained, led to pre-static or static solutions. That's *stochastically irreproducible*.

When such situation occurs, gradually reducing the initial learning rate with cyclic annealing, using Remark 5.7 (VCA), and extending the learning-rate schedule, Remark 5.9 (ELRS), would usually help. For the case of Figure 15 with lowest total loss of 2.12e-06 at Step 200,000, using VCA for Cycles 1-5 with $\text{init_lr} = [0.01, 0.009, 0.008, 0.007, 0.006]$ and NCA for Cycles 6-9, and $N_{\text{steps}} = 400,000$ steps, yielded a *quasi-perfect* solution with lowest total loss 0.793e-06 at Step 400,000 with total GPU time 748 sec (RunID 23831R2c). This VCA-ELRS solution is *stochastically reproducible*, i.e., *stable* in the sense that rerunning the script several times led to stochastically equivalent solutions.

Hence with the above VCA-ELRS, a good trade-off would be at Step 200,000 with 4,482 parameters, lowest total loss 1.92e-06 at Step 200,000, total GPU time 401 sec (RunID 23831R2c), and a *quasi-perfect* solution not distinguishable from that in Figure 35, which was obtained with 12,802 parameters, lowest total loss 0.537e-06 at Step 192,000, total GPU time 640 sec. ■

5.3 Axial motion of elastic bar

5.3.1 Form 1: Shift, amplification, early stopping, static solution

The numerical evidence presented below shows that our JAX script solves many problems encountered with DDE-T, specifically:

- For the pinned-pinned bar, DDE-T produced shift and amplification in the solution, whereas our JAX script shows no such problems. To solve these particular DDE-T problems (shift and amplification), we devised several methods (Form 2a, Form 3, Form 4) before writing our own JAX script.
- For the pinned-free bar, DDE-T produced a static-solution time history, i.e., not dynamic solution, regardless of the size of the learning rate or the network capacity, whereas our JAX script shows no such problem. To solve this particular DDE-T problem (static solution), we devised several methods (barrier function, reduced network capacity, different learning-rate schedules) before writing our own JAX script.

Form 1. The Form 1 of the axial equation of motion of an elastic bar is a particular case of the Form 1 for the Kirchhoff-Love rod in Section 3.2, and was given above in Eq. (64), reproduced below for convenience:

$$\mathcal{J}\bar{u}^{(2)} + \bar{f}_X = \ddot{\bar{u}}, \quad (64)$$

where $\mathcal{J} = 1$ is the slenderness of the bar, defined in Eq. (32), $\bar{f}_X = \frac{1}{2}$, with the following two types of prescribed boundary conditions:

Pinned-pinned bar, using Eq. (47)₁ for $\bar{X} = 0$ and a similar one for $\bar{X} = 1$:

$$\bar{u}(\bar{X} = 0, \bar{t}) = \bar{u}(\bar{X} = 1, \bar{t}) = 0 \quad (85)$$

Pinned-free bar, using Eq. (47)₁ and Eq. (48)₁, and the extension \bar{e} from Eq. (6) and Eq. (27):

$$\bar{u}(\bar{X} = 0, \bar{t}) = \hat{\bar{u}} = 0, \quad \bar{e}(\bar{X} = 1, \bar{t}) = \bar{u}^{(1)}(1, \bar{t}) = \frac{1}{\mathcal{J}}\hat{N} = 0 \quad (86)$$

The prescribed initial conditions, using Eq. (49), are:

$$\bar{u}(\bar{X}, 0) = \tilde{\bar{u}}_0(\bar{X}) = 0, \quad \dot{\bar{u}}(\bar{X}, 0) = \tilde{\dot{\bar{u}}}_0(\bar{X}) = 0. \quad (87)$$

The reference solutions for the pinned-pinned bar and for the pinned-free bar are given in Figure 5.

Since both the strain $\bar{u}^{(1)}$ and the velocity $\dot{\bar{u}}$ are not explicit outputs in Form 1, these boundary and initial

conditions cannot be explicitly enforced using hard constraints, but have to be imposed after computing the derivatives of the outputs using backpropagation and then included as additional squared errors in the overall loss function (soft constraints).

Remark 5.17. *DDE-T vs JAX, Form 1, pinned-pinned bar: Time shift, amplification, damping percentage.* *DDE-T* with Form 1 produced a shift and amplification in the solution and larger errors in boundary conditions with derivatives (Neumann type). JAX does not exhibit these pathological problems.

For a pinned-pinned elastic bar subjected to a constant distributed axial load, Figure 20 shows two vibration periods of the deformed-shape time history and the midspan-displacement time history, shifted to the right, at training Step 100,000 obtained from a *regular* grid, whereas Figure 21 shows the same output variables at Step 200,000 obtained from a *fixed random* grid. Also for the same pinned-pinned bar, Figures 22-23 show the shift (time and vertical) and amplification parameters increase continuously with training step number, as the training progressed to the final Step 400,000.

Using JAX, Figure 24 shows no shift since the times of the local maxima were exactly where they should be, and so were the times for the local minima. There was no amplification, except for a small damping. For results obtained with JAX, the quality of a response curve is measured by the damping percentage (damping% for short) defined by the ratio of the 1st local maximum over the 2nd local maximum minus one, with amplification% = $1 - \text{damping\%} > 0$. For example, the midspan displacement of a pinned-pinned bar in Figure 24 has a damping% of 1.7%, which is discernible. The quality of the response is classified by the damping% as follows:

- | damping% | < 0.5% : Quasi-perfect, damping/amplification is not discernible by naked eyes.
- | damping% | $\in [0.5\%, 1.5\%)$: Very good, small damping, could be discernible by naked eyes.
- | damping% | $\in [1.5\%, 3.0\%)$: Good, significant damping, discernible by naked eyes.
- | damping% | $\geq 3.0\%$: High damping, easily visible.

■

Remark 5.18. *DDE-T vs JAX, Form 1, pinned-pinned bar: Early stopping and divergence.* After the lowest loss was reached earlier in the training process, and the loss function stopped to decrease after this lowest value, the training process can then be stopped earlier. Depending on the behavior of the loss function after the lowest loss, the training could diverge. See also “early stopping” in [1].

Using DDE-T, Figure 25 shows the loss function (left) with the lowest value of $2.30\text{e-}05$ remaining at Step 24,000 as the training progressed to Step 100,000, with plateaus at loss value of 0.25, many orders of magnitude above the lowest loss, showing divergence. Once a plateau appears, there is no need to continue further, and stop the training process early, e.g., at Step 50,000 (or before). On the right subfigure is the shape time history at Step 24,000 (the lowest loss).

Figure 26 (DDE-T) shows a good midspan displacement with damping at Step 25,000, the last step at the end of Cycle 1 (left) and zero midspan displacement at Step 100,000 (divergence).

Using JAX, a similar behavior of “early stopping” was also observed.

■

Remark 5.19. *DDE-T vs JAX, Form 1, pinned-free bar: Static solution.* Our DDE-T script for Form 1 produced a static-solution time history in every case. Our JAX script does not exhibit this pathological problem. For the pinned-free bar subjected to a constant distributed axial load, DDE-T produced a static solution regardless of the size of the learning rate and the network capacity (Figure 27), whereas JAX produced **no** static solution, but the expected waves with two vibration periods (Figure 28), as obtained with Mathematica in Figure 5.

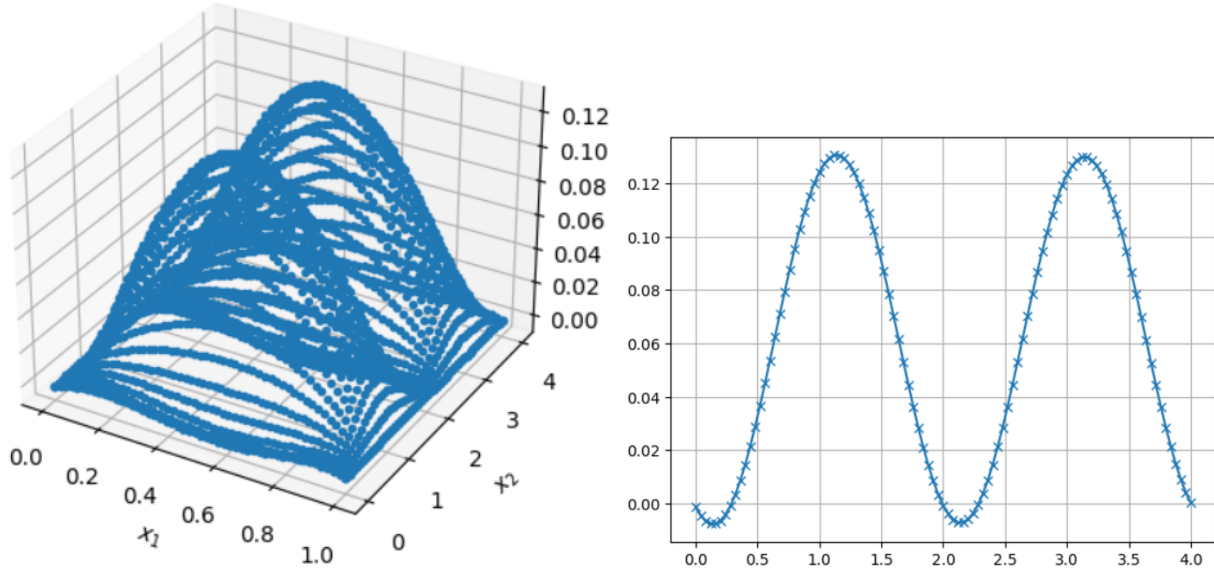


Figure 20: DDE-T. Pinned-pinned bar. Shape (left), midspan displacement *shifted to the right with small amplification* (right), Step 100,000. ★ Section 5.3.1, **Form 1**. Network: Remarks 5.3, 5.5, $T=4$, $W=64$, $H=4$, $n_{\text{out}}=1$, Glorot-uniform initializer, 12,737 parameters, *regular grids*. Training: ★ Remark 5.8, **LRS 3 (NCA)**, $\text{init_lr}=0.001$, $n\text{-cycles}=3$, $N_{\text{steps}}=100,000$. ★ PDE loss $2.20\text{e-}06$, Cycle 3 GPU time 154 sec. ▷ Figure 5, reference solution to compare. (23722R1-1)

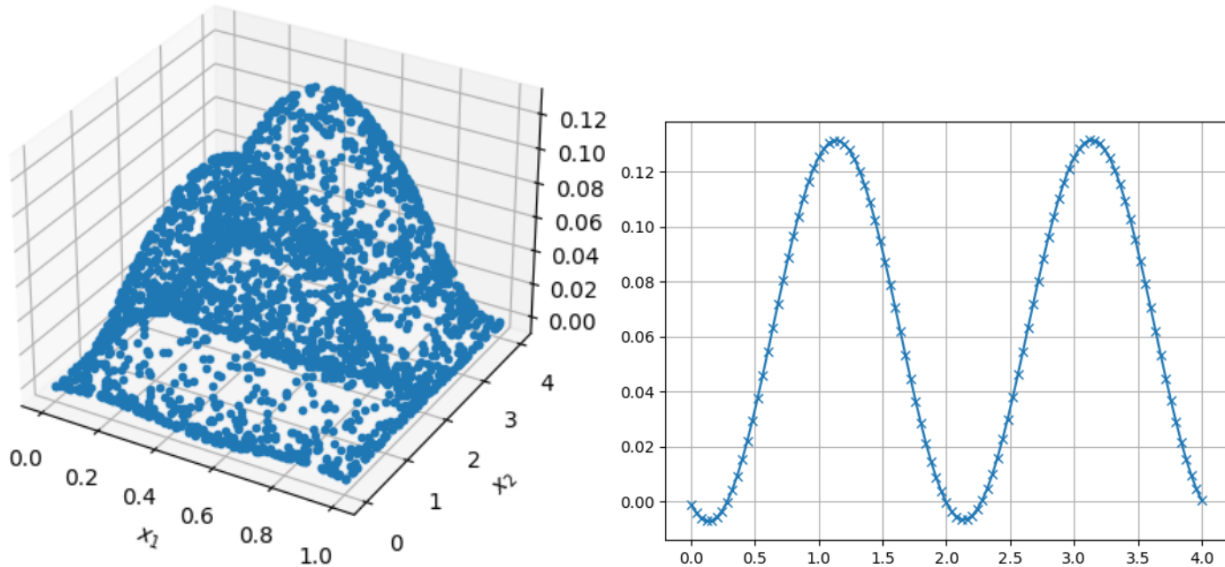


Figure 21: DDE-T. Pinned-pinned bar. Shape (left), midspan displacement *shifted to the right with small amplification* (right), Step 200,000. ★ Section 5.3.1, **Form 1**. Network: Remarks 5.3, 5.5, $T=4$, $H=4$, $W=64$, $n_{\text{out}}=1$, Glorot-uniform initializer, **12,737** parameters *fixed random grid*. Training: ★ Remark 5.6, **LRS 1 (CA)**, $\text{init_lr}=0.001$. ★ Lowest total loss $4.31\text{e-}06$, Step 200,000 (sum of 5 losses). ★ Total GPU time **621 sec**. ● Figures 42-44, **Form 3**, VCA-ELRS, **1,251** parameters, *quasi-perfect* solution (no shift), lowest total loss $1.25\text{e-}06$, total GPU time **598 sec**. ▷ Figure 5, reference solution to compare. (23723R1d-4)

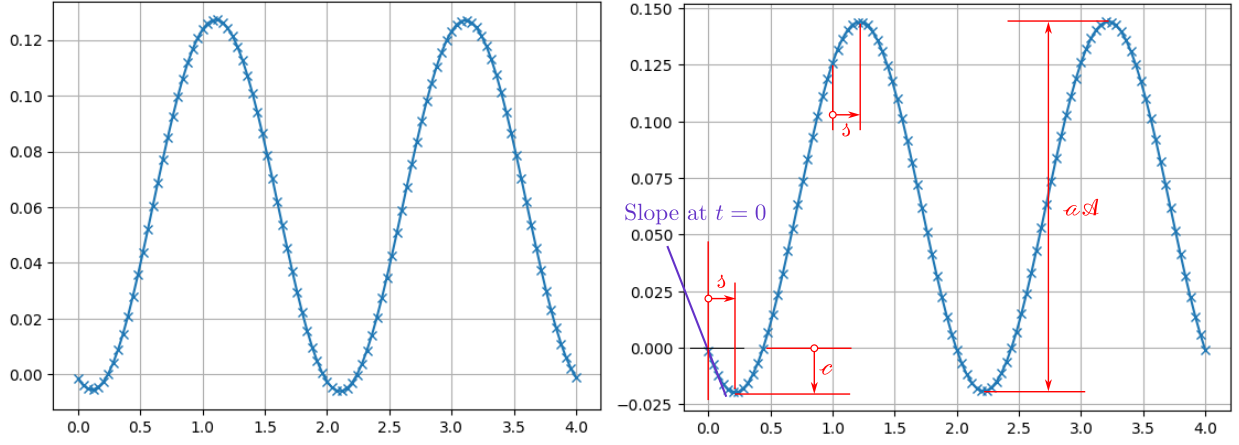


Figure 22: DDE-T. Pinned-pinned bar, *continued shift & amplification*. ★ Midspan displacements: Step 50,000 (left), Step 400,000 (right). ★ Section 5.3.1, **Form 1**: Hidden parameters (δ , c , a), time shift δ , vertical shift c , amplification a , quasi-perfect peak-to-peak amplitude A . *Network*: Remarks 5.3, 5.5, $T=4$ $W=64$, $H=4$, $n_{\text{out}}=1$, He-uniform initializer, 12,737 parameters, regular grid. *Training*: Remark 5.6, **LRS 3 (NCA)**, $\text{init_lr}=0.005$, $N_{\text{steps}}=400,000$.
 ● Figure 23, shift-amplification parameters increase with training step number. (2394R1a-1)

Form 1, pinned-pinned bar: Shift and amplification

Time shift, Minimum (vertical shift), Peak-to-peak amplitude, Initial slope (velocity)

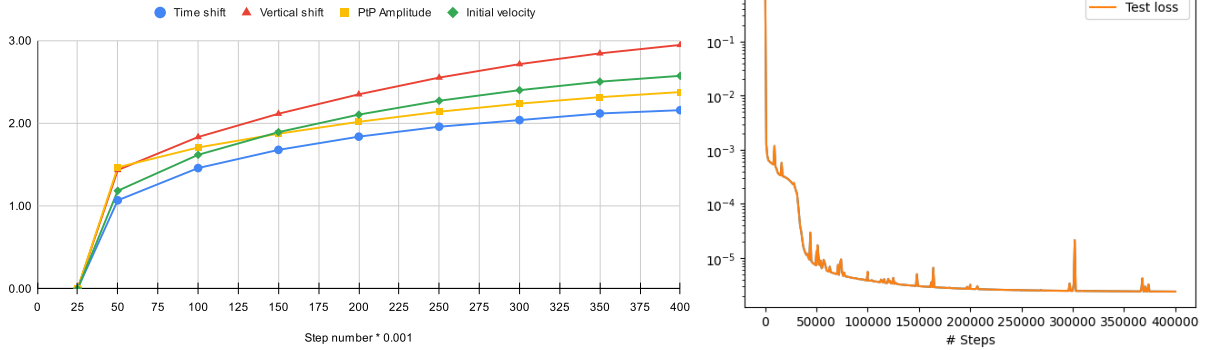


Figure 23: DDE-T. Pinned-pinned bar. **Form 1**. Appendix 1, *Analysis*. Scaled shift-amplification parameters (δ , c , a) and initial velocity increase with training step number (left), while the Total loss continues to decrease (right). All parameters p , such as time shift δ , vertical shift c , amplification factor a and thus peak-to-peak amplitude aA , and initial velocity, were scaled to fit in the chart. ● Table 2, *unscaled* values of δ , c , a and computed initial velocity, scaling method. Figure 22, midspan displacements, Steps 50000 & 400000. (2394R1d-2)

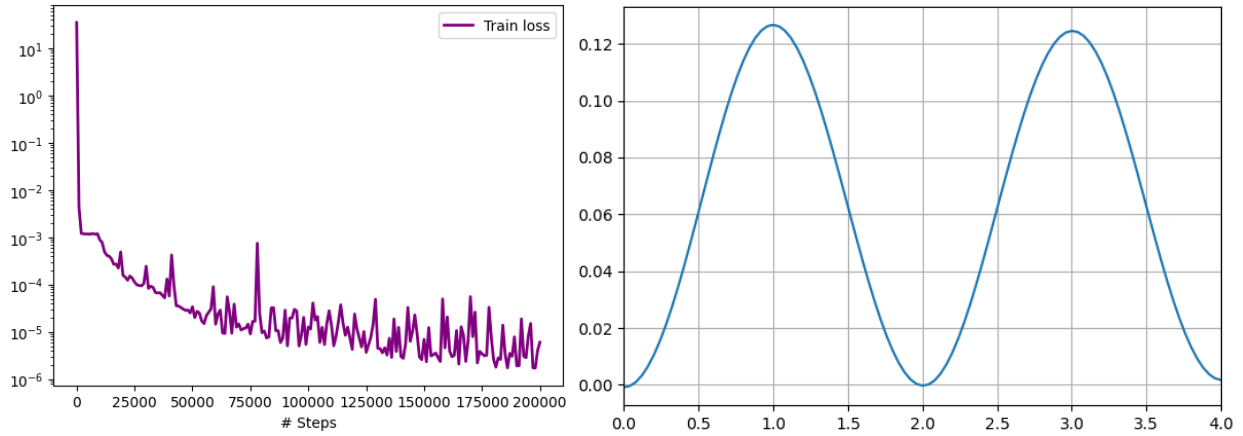


Figure 24: [JAX](#). Pinned-pinned bar, *No shift & amplification*, Remark 5.17. ★ Left: Loss function. Right: Step 198,000, lowest loss $1.724\text{e-}06$, midspan displacement, times at local maxima (1., 3.), times at local minima (0., 2., 4.), damping%=1.7%, Quality: Good. ★ Section 5.3.1, Form 1. Network: Remarks 5.3, 5.5, $T=4$, $W=64$, $H=4$, Uniform initializer, 12,737 parameters, random grid. Training: Remark 5.10, LRS 4, $\text{init_lr}=0.002$, $\text{factor_lr}=[0.9, 0.9, 0.9, 0.8, 0.8]$, $n\text{-cycles}=5$, $N\text{-steps}=200,000$. Total GPU time 564 sec. • Figure 21, [DDE-T](#), shift and amplification. Figure 22, [DDE-T](#), shift-amplification parameters. Figure 23, [DDE-T](#), shift-amplification parameters increase with training step number. ▷ Figure 35, [DDE-T](#), Form 2a, visually quasi-perfect midspan displacement. (23917R1d-1)

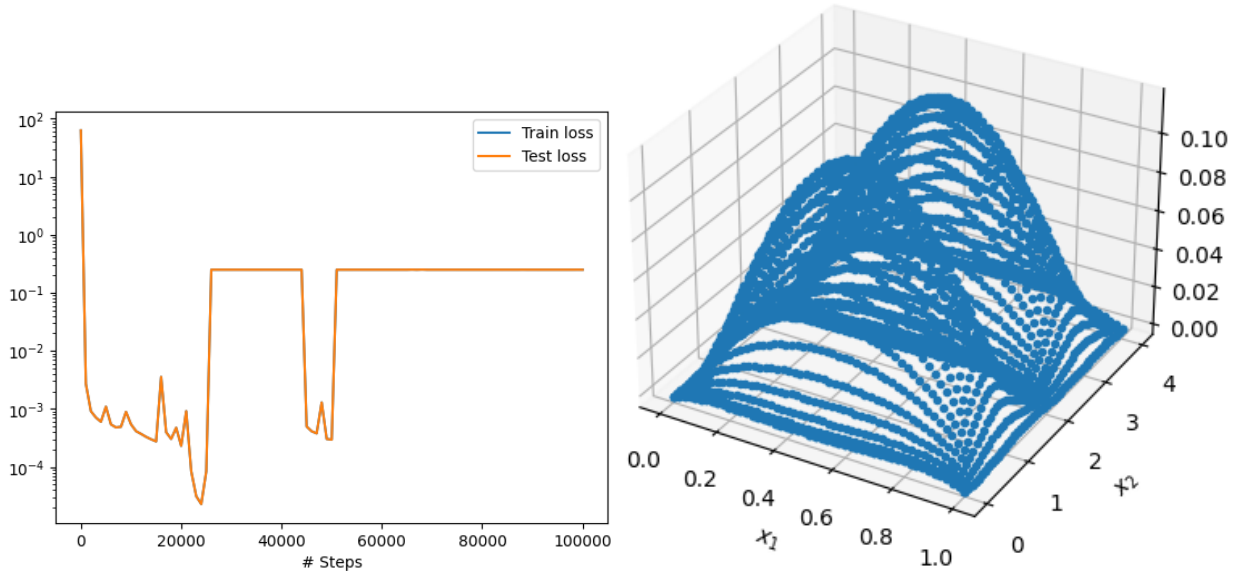


Figure 25: [DDE-T](#). Pinned-pinned bar, *early stopping*. ★ Left: Loss function, *lowest* value $2.30\text{e-}05$ at Step 24,000, value 0.25 at Step 100,000, *divergence*. Right: Shape, Step 24,000. ★ Section 5.3.1, Form 1. Network: Remarks 5.3, 5.5, $T=4$, $W=64$, $H=4$, $n\text{-out}=1$, He-uniform initializer, 12,737 parameters, regular grid. Training: Remark 5.6, LRS 1 (CA), $\text{init_lr}=0.03$. • Figure 26, midspan displacement, Step 25,000, and zero midspan displacement, Step 100,000 (divergence). ▷ Figure 5, reference solution to compare. (2386R2b-1)

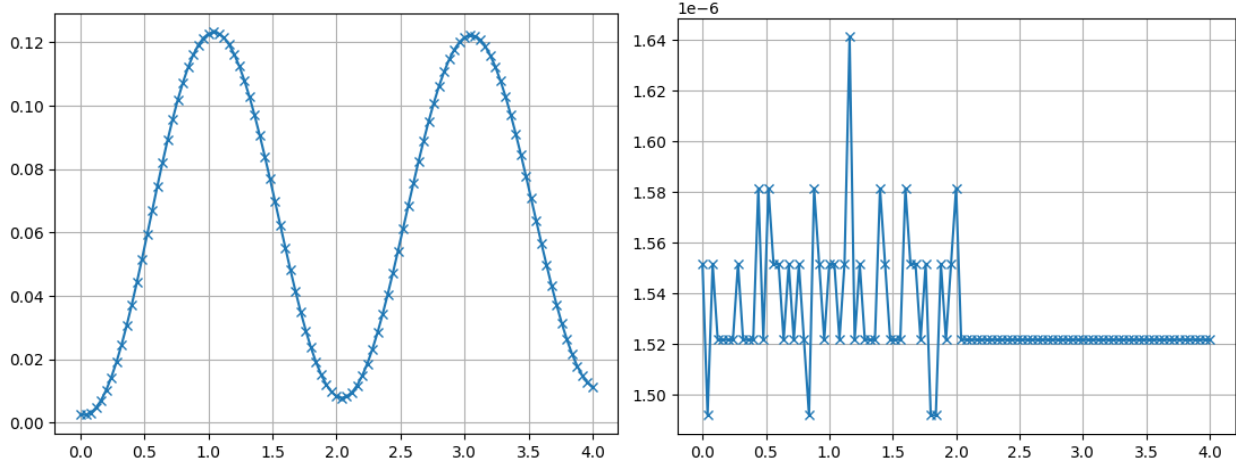


Figure 26: **DDE-T**. *Pinned-pinned bar*. Midspan displacement, damping, Step 25,000 (left), zero midspan displacement, Step 100,000 (divergence, right). Section 5.3.1, **Form 1**. *Network*: Remarks 5.3, 5.5, $T=4$, $W=64$, $H=4$, $n_{\text{out}}=1$, He-uniform initializer, 12,737 parameters, regular grid. *Training*: Remark 5.6, LRS 1 (CA), $\text{init_lr}=0.03$. • Figure 25, loss function and shape, Step 24,000 with lowest loss. (2386R2b-2)

Using DDE-T, several different sets of parameters were considered with the number of network parameters varying from 12,737 down to 33, and with two initial learning rates, 0.001 and 0.0001. The results from four different network-parameter numbers (from 12,737 down to 105) and with the initial learning rate of 0.001 are given in Figure 27, in which all subfigures had these common parameters, which are not repeated in the figure caption: $T=8$, $N_{\text{out}}=1$, Glorot-uniform initializer, random grid. Identical results (i.e., static solutions) were also obtained with the smaller initial learning rate 0.0001. ■

5.3.2 Form 2a: No time shift, static solution, efficiency

The PINN Form 2a for the axial equation of motion of an elastic bar is a particular case of the PINN Form 2a for the Kirchhoff-Love rod in Section 3.3.

$$\mathcal{A}\bar{u}^{(2)} + \bar{f}_X = \dot{\bar{p}}_X, \quad \dot{\bar{u}} = \bar{p}_X, \quad (88)$$

with the initial conditions:

$$\bar{u}(X, 0) = \bar{u}_0, \quad \bar{p}_X(X, 0) = \dot{\bar{u}}_0. \quad (89)$$

In the numerical examples, we use homogeneous initial conditions:

$$\bar{u}(X, 0) = 0, \quad \bar{p}_X(X, 0) = 0. \quad (90)$$

Remark 5.20. *Static solution, methods to avoid. Pinned-pinned bar.* Using **DDE-T** Form 2a (time-derivative splitting) and a *regular* grid, Figure 29 show the loss function and a static-shape time history (or “static solution” for short, Remark 3.3), with the velocity and midspan-displacement time histories shown in Figure 30, all figures were from Step 50,000 of the same run. A sharp jump with a flat plateau along the time axis in the time history, such as in the right subfigure of Figure 30, is a telltale sign of a static solution.

Because of the perfect alignment of the data points along the time axis, *regular* grids would lead to *static* solutions easier than random grids.

A *pre-static* time history is a solution at an early optimization step (e.g., 25,000) having the characteristic (a jump with a wavy plateau) that portend a static time history at subsequent optimization steps, and thus is a sign to stop the optimization process early (no need to continue further). Two pre-static midspan-

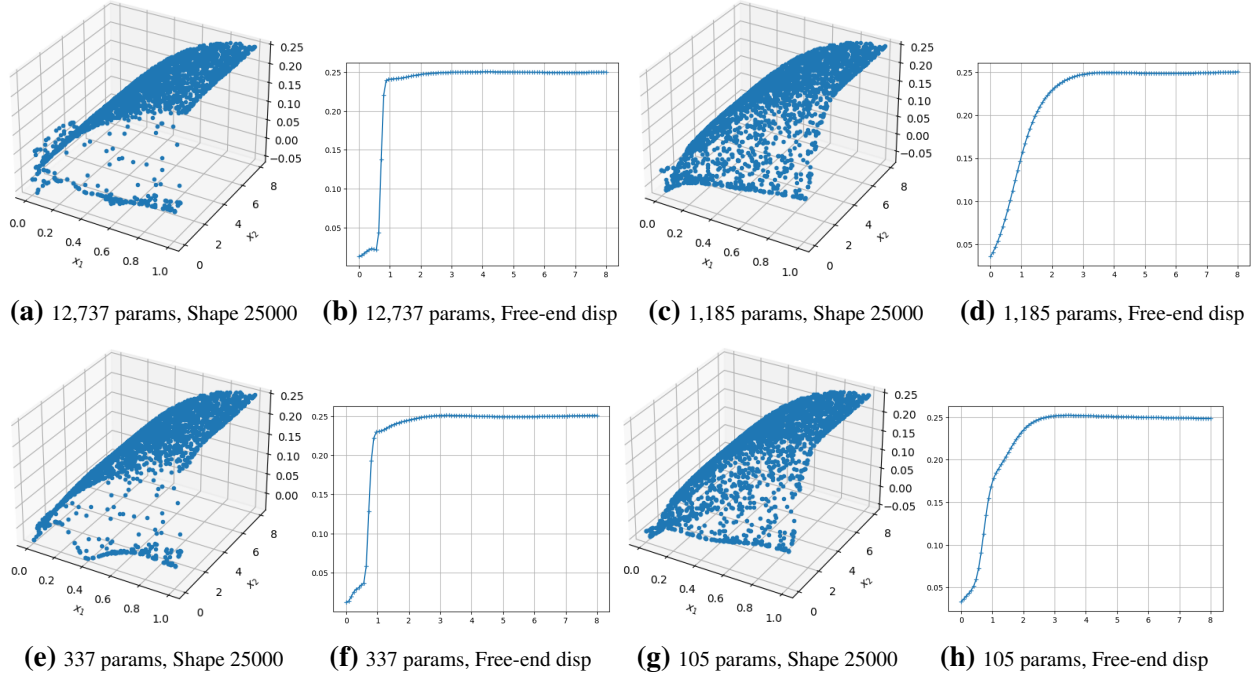


Figure 27: *DDE-T, Form 1, pinned-free bar, static solutions* (Remark 5.19, Section 5.3.1).

- SubFigs. 27a-27b: Shape, free-end displacement, Step 25000; GPU time 655 sec (Deterministic mode) for 200,000 steps. (2398R2a). Shape, free-end disp, step number for other pairs: (27c-27d) (2398R2b), (27e-27f) (2398R2c), (27g-27h) (2398R2d).
- *Network*: Remarks 5.3, 5.5, $T=8$, $W=64$, $H=2$, $n_{out}=1$, Glorot-uniform initializer, random grid. *Training*: Remark 5.6 LRS 1, $init_lr=0.001$, $N_steps=25000$.
- Figure 28, using our JAX script, no static solution. ▷ Figure 38, Form 2a, GPU time 605 sec for 200,000 steps. Figure 45, Form 3, GPU time 537 sec for 200,000 steps. ▷ Figure 5, reference solution to compare. ▷ Appendix 2, Figure 50, barrier-function effects.

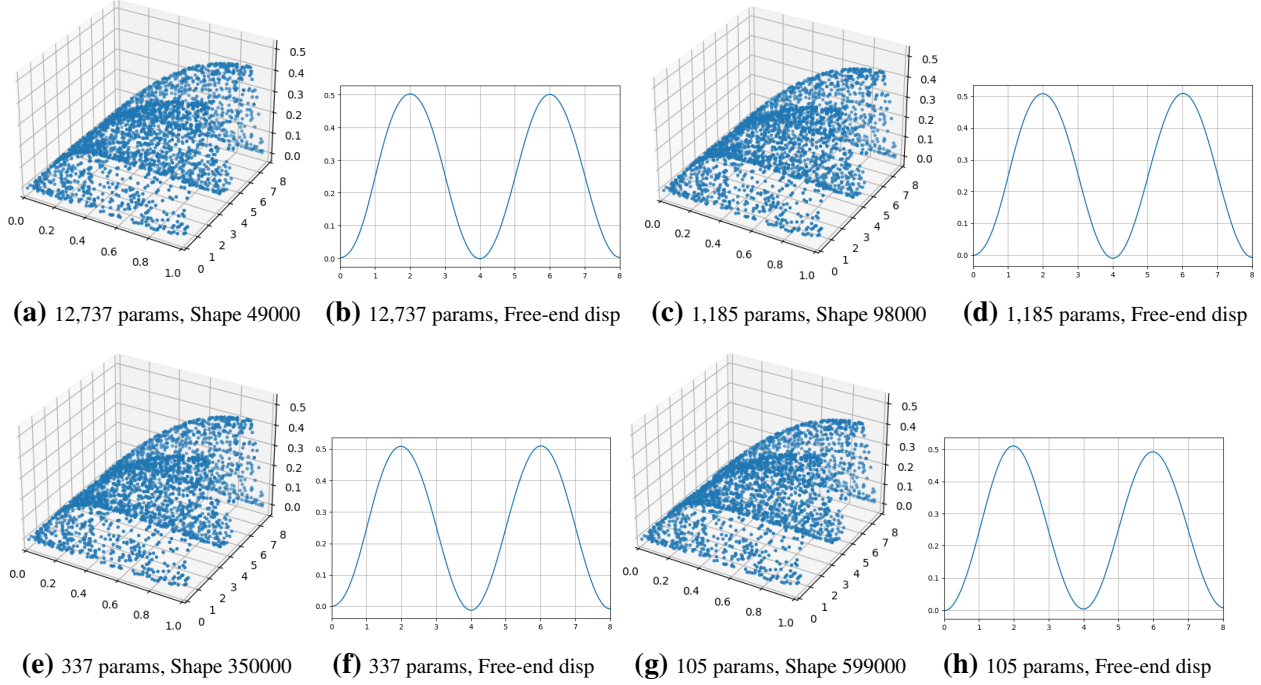


Figure 28: JAX. Form 1, pinned-free bar. Remark 5.10 (LRS 4). • SubFigs 28a-28b: 12,737 params, Step 49,000, Cycle 2 lowest loss $5.324\text{e-}06$, damping%=0.25%, Quasi-perfect, GPU time 161 sec. Network: Remarks 5.3, 5.5, T=8, W=64, H=2, n_out=1, Uniform initializer, random grid. Training: Remark 5.10 LRS 4, init_lr=0.002, factor_lr=[0.9, 0.9, 0.9, 0.8, 0.8, 1, 1, 1, 1]. (23916R1a.4). ★ SubFigs 28c-28d: Cycle 3 lowest loss $4.381\text{e-}06$, damping%=0.2%, Quasi-perfect, GPU time 107 sec (23916R1b.1). • SubFigs 28e-28f: Cycle 8 lowest loss $5.445\text{e-}06$, damping%=0.0014%, Quasi-perfect, GPU time 335 sec (23916R1c.2.2). • SubFigs 28g-28h: Cycle 13 lowest loss $2.749\text{e-}05$, damping%=3.7%, High damping, GPU time 505 sec (23916R1d.2.3). • Figure 27, using DDE-T, static solutions. ▷ Figure 5, reference solution to compare.

displacement time histories at Step 25,000 are shown in Figure 31, both with $\text{init_lr}=0.03$. The optimization for the left subfigure continues to Step 200,000 to exhibit a clear static solution shown in Figures 32-33, whereas the optimization for the right subfigure, where the jump at time $t = 0$ is already sure sign of a static solution, stopped at Step 25,000.

Several methods below (or a combination of these) could be used to avoid the static solution: (1) Use *random* grid (Figure 35) instead of regular grid (Figures 29-30), (2) Reduce the initial learning rate init_lr (see below), (3) Reduce network capacity (number of network parameters) (see below), (4) Use barrier function (see Appendix 2).

Using the same Form 2a and network with 12,802 parameters as in Figures 29, and reduce init_lr from 0.01 to various values below. Reducing the initial learning rate by 100 times to $\text{init_lr}=0.0001$ with NCA produced un-accentuated waves with high damping at Step 200,000. On the other hand, reducing by 10 times to $\text{init_lr}=0.001$ with CA, and extending Step 5 to 250000 with NCA (Remark 5.9), resulted in a good solution with small damping, Figure 34. See also Remark 5.16, *Unstable solution*.

Reducing the network capacity would allow using a much larger learning rate for similar results. Figure 6 shows a static solution using a network with only 1,218 parameters (ten times smaller) with $\text{init_lr}=0.07$ (seven times larger) compared to Figures 29-30 using a network with 12,802 parameters and $\text{init_lr}=0.01$. Figure 39 shows a solution obtained with DDE-T Form 3 using a network with 12,867 parameters, $\text{init_lr}=0.01$, NCA, resulting in the Cycle 3 lowest loss of $1.179\text{e-}06$ at Step 88,000, and a **quasi-perfect** midspan displacement of a pinned-pinned bar.

Pinned-free bar. The static solutions in DDE-T Form 1 in Figure 27 are totally avoided by using DDE-T Form 2a (Figure 38), and of course DDE-T Form 3 (SubFigs 45i-45l). ■

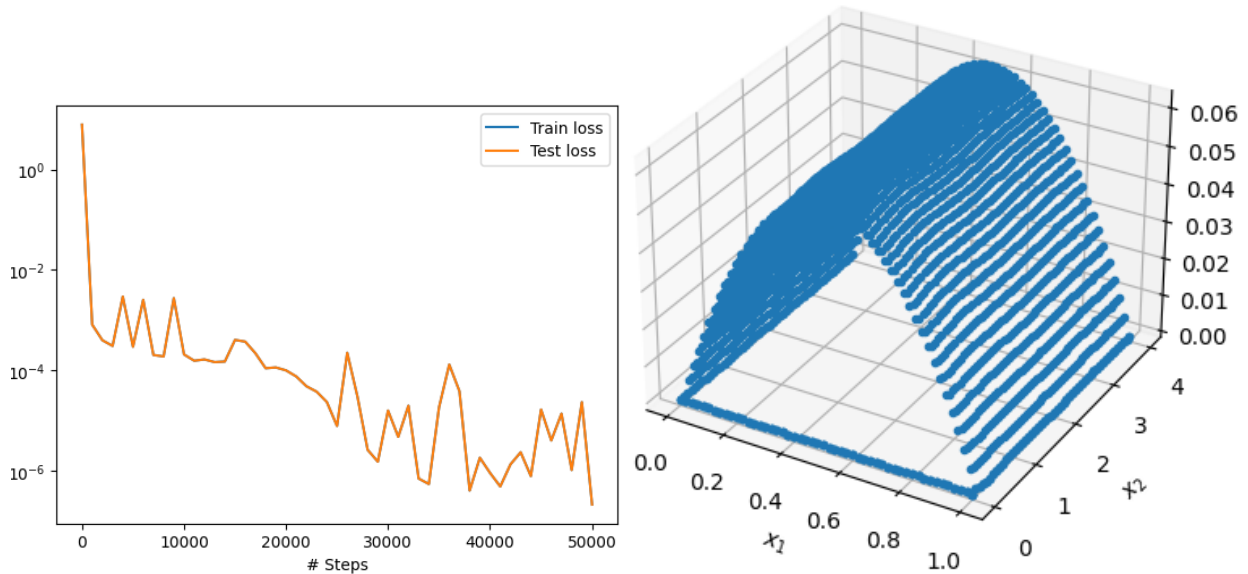


Figure 29: DDE-T. Pinned-pinned bar, static solution. Loss function (left), static solution (right), Step 50,000, end of Cycle 2. ★ Remark 3.3, Static solution; Remark 5.20, How to avoid. Section 5.3.2, Form 2a. Network: Remarks 5.3, 5.5, $T=4$, $W=64$, $H=4$, $n_{\text{out}}=2$, He-uniform initializer, 12,802 parameters, ★ regular grid. Training: Remark 5.8, LRS 3, $\text{init_lr}=0.01$, $n_{\text{cycles}}=2$, $N_{\text{steps}}=50,000$. • Figure 30, velocity, midspan displacement. ▷ Figure 34, regular grid, smaller $\text{init_lr}=0.001$. Figure 35, random grid, no static solution (same LRS 3 and init_lr). (23725R1-1)

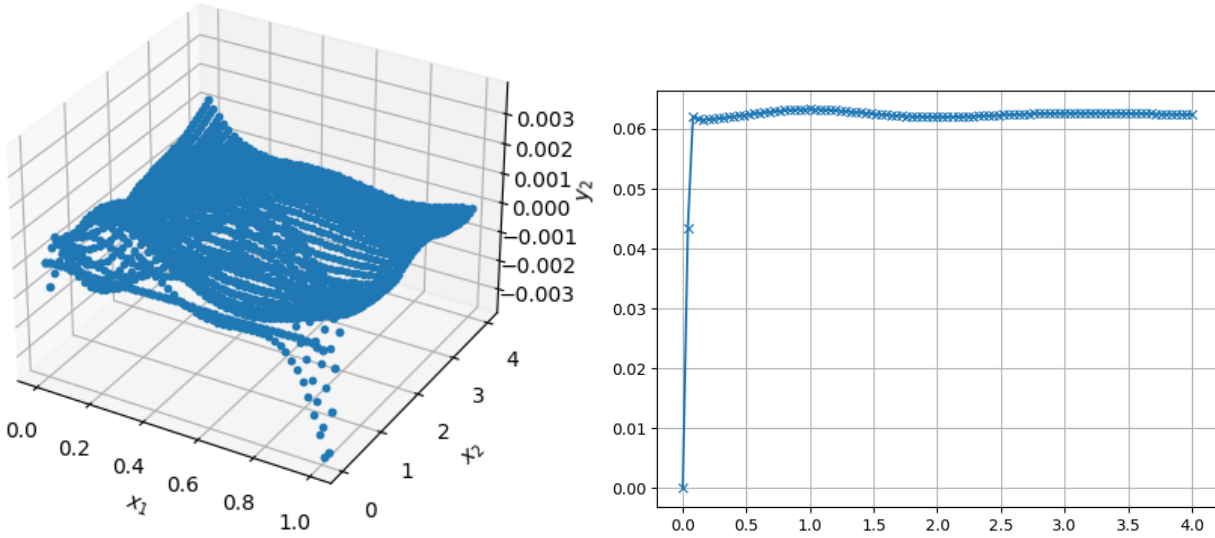


Figure 30: DDE-T. Pinned-pinned bar, static solution. Essentially-zero velocity (left); static midspan displacement (right), Step 50,000, end of Cycle 2. ★ Remark 3.3, Static solution; Remark 5.20, How to avoid. Section 5.3.2, Form 2a. Network: Remarks 5.3, 5.5, $T=4$, $W=64$, $H=4$, $n_{\text{out}}=2$, He-uniform initializer, 12,802 parameters, ★ regular grid. Training: Remark 5.8, LRS 3, $\text{init_lr}=0.01$, $n\text{-cycles}=2$, $N_{\text{steps}}=50,000$. ● Figure 29, loss function, shape. ▷ Figure 34, regular grid, smaller init_lr . Figure 35, random grid, no static solution (same LRS 3 and init_lr). (23725R1-2)

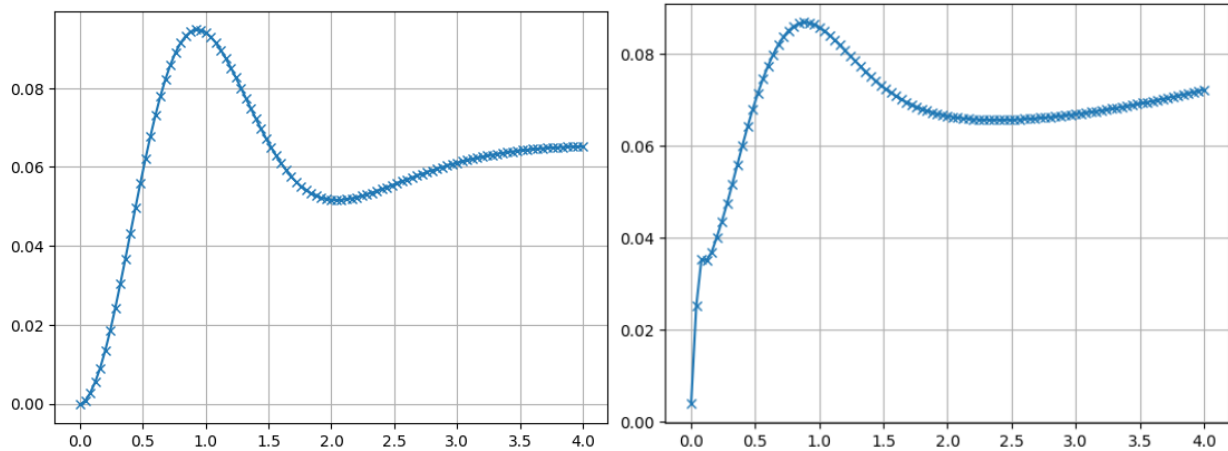


Figure 31: DDE-T. Pinned-pinned bar. Pre-static midspan-displacement time histories at Step 25,000 (end of Cycle 1). ★ Remarks 3.3, 5.20. Section 5.3.2, Form 2a. ★ Network: Remark 5.3, 5.5, $T=4$, $W=64$, $H=2$, $n_{\text{out}}=2$, He-uniform initializer, 4,482 parameters, regular grid. Training: Remark 5.8, LRS 3, $\text{init_lr}=0.03$. ★ Left: $n\text{-cycles}=5$, $N_{\text{steps}}=200,000$; Figures 32-33, Step 200,000. (23815R3a-1). ★ Right: $n\text{-cycles}=1$, $N_{\text{steps}}=25,000$, jump at $t=0$. (2389R2-1).

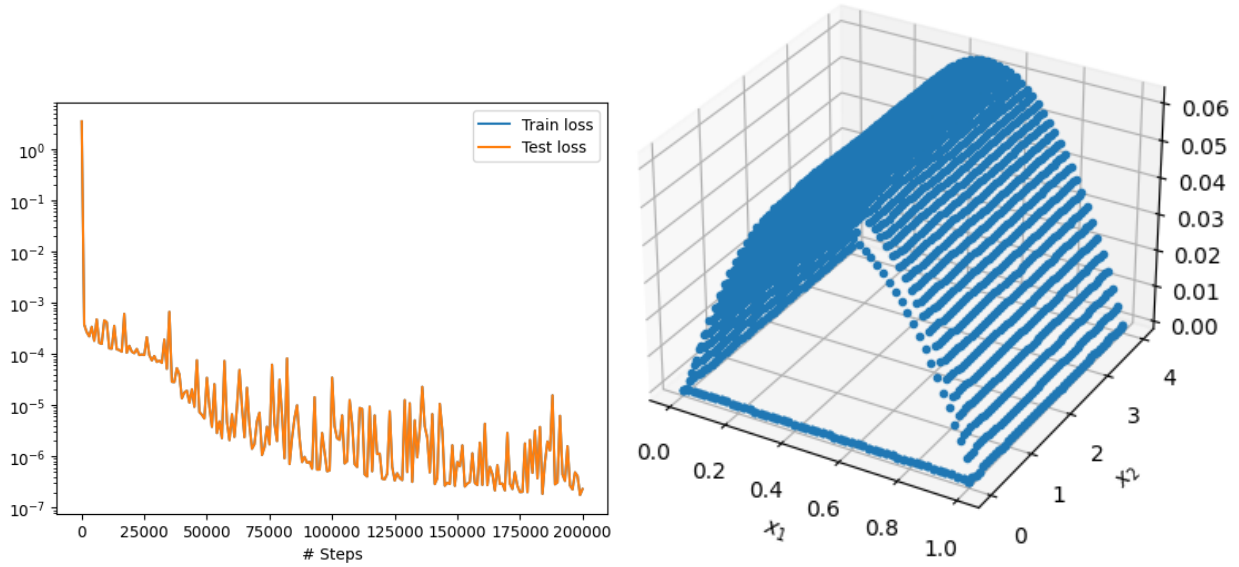


Figure 32: [DDE-T](#). Pinned-pinned bar, no cyclic annealing (NCA). Loss function (left) and static-shape (right), Step 200,000. ★ Remarks 3.3, 5.20. Section 5.3.2, Form 2a. Network: Remarks 5.3, 5.5, $T=4$, $W=64$, $H=2$, $n_{out}=2$, He-uniform initializer, 4,482 parameters, regular grid. ★ Training: Remark 5.8, LRS 3, $init_lr=0.03$. ● Figure 31, left, midspan displacement, Step 25,000. Figure 33, velocity, midspan displacement, Step 200,000. (23815R3a-2)

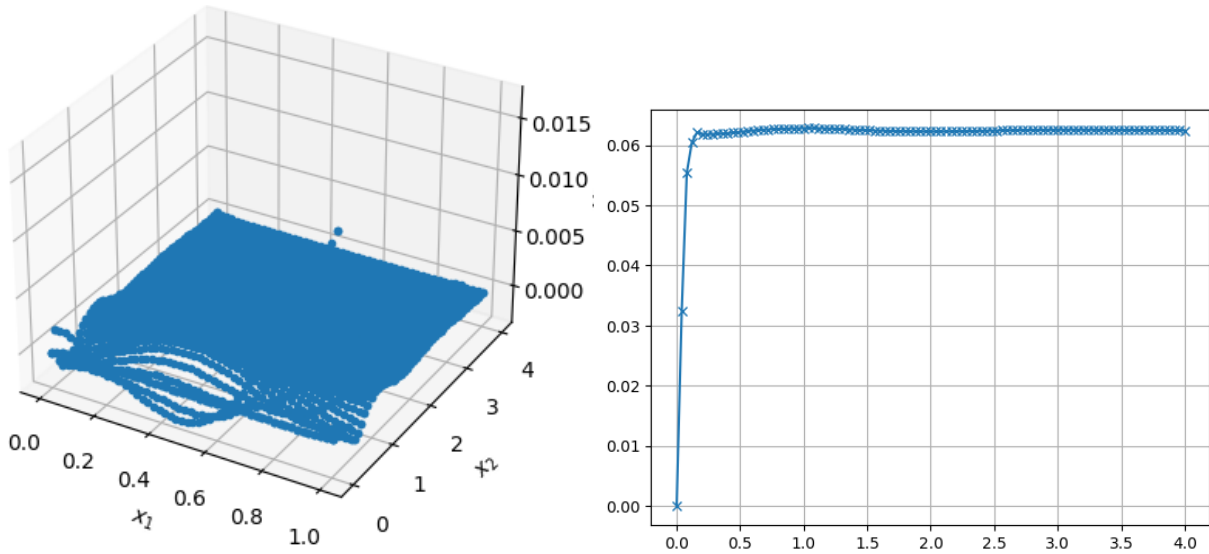


Figure 33: [DDE-T](#). Pinned-pinned bar, no cyclic annealing (NCA). ★ Essentially-zero Velocity (left), static midspan displacement (right), Step 200,000. ★ Remarks 3.3, 5.20. Section 5.3.2, Form 2a. Network: Remarks 5.3, 5.5, $T=4$, $W=64$, $H=2$, $n_{out}=2$, He-uniform initializer, 4,482 parameters, regular grid. Training: Remark 5.8, LRS 3, $init_lr=0.03$. ● Figure 31, left, midspan displacement, Step 25,000. Figure 32, loss function, static shape, Step 200,000. (23815R3a-3)

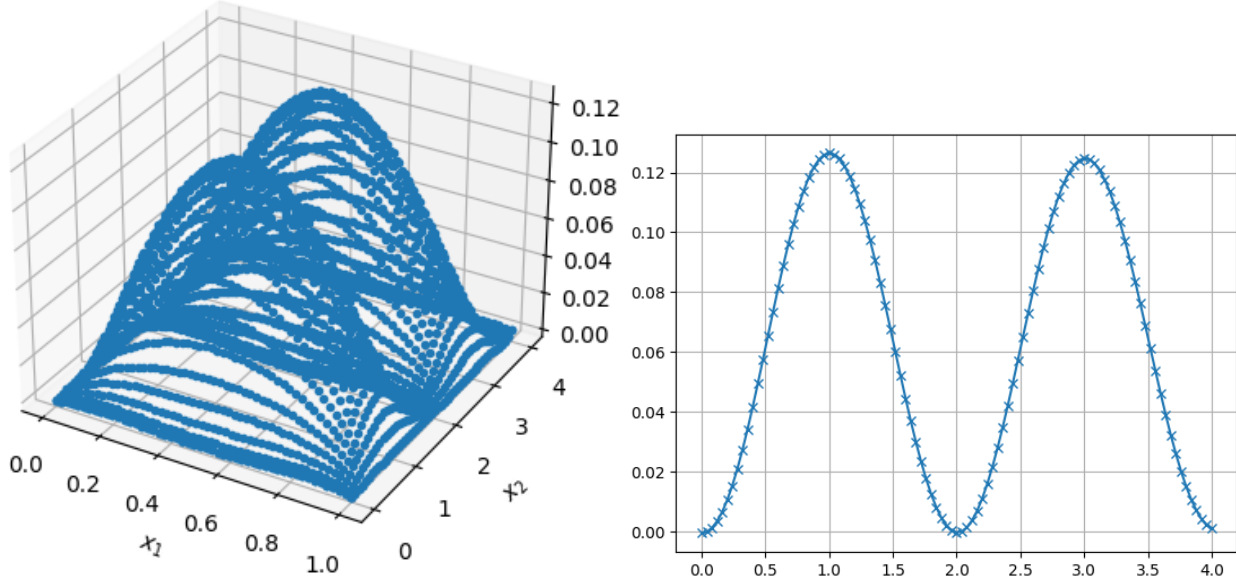


Figure 34: **DDE-T.** Pinned-pinned bar. Shape (left), midspan displacement (right), small damping, Step 250,000. ★ Section 5.3.2, Form 2a. Network: Remarks 5.3, 5.5, T=4, W=64, H=4, n_out=2, He-uniform initializer, 12,802 parameters, regular grid. Training: ★ Remarks 5.6 (LRS 1), 5.9 (ELRS), init_lr=0.001, Cycles 1-5 (CA), Cycle 6 (NCA), N_steps=250,000. ★ Lowest total loss 2.55e-06, Step 250,000 (sum of 6 losses). ● Figures 29-30, init_lr=0.01, static solution. Figure 15, 4,802 parameters, good solution. ▷ Figure 5, reference solution to compare. (23822R3b-1)

5.3.3 Form 2b: Same issues as Form 1

Form 2b for the axial equation of motion of an elastic bar is a particular case of Form 2b for the Kirchhoff-Love rod in Section 3.4:

$$\mathcal{J}\bar{s}_u^{(1)} + \bar{f}_X = \ddot{\bar{u}}, \quad \bar{u}^{(1)} = \bar{s}_u, \quad (91)$$

with the initial conditions

$$\bar{u}(X, 0) = \bar{u}_0, \quad \dot{\bar{u}}(X, 0) = \dot{\bar{u}}_0, \quad \bar{s}_u(X, 0) = \bar{s}_{u0}. \quad (92)$$

In the numerical examples, we use homogeneous initial conditions:

$$\bar{u}(X, 0) = 0, \quad \dot{\bar{u}}(X, 0) = 0, \quad \bar{s}_u(X, 0) = 0. \quad (93)$$

Form 2b (splitting the space derivative operator) does not resolve the shift and amplification like Form 2a (splitting the time derivative operator). For example, using the same parameters as in Figure 20 for the pinned-pinned bar, shift and amplification, albeit with a different magnitude, still persisted.

Form 2b also yielded the same static solutions as those in Figure 27.

5.3.4 Form 3 (or 4): No space/time shift, static solution, efficiency

Form 3 (or 4) for the axial equation of motion of an elastic bar is a particular case of Form 3 (or 4) for the Kirchhoff-Love rod in Section 3.5 (or 3.6):

$$\mathcal{J}\bar{s}_u^{(1)} + \bar{f}_X = \dot{\bar{p}}_X, \quad \bar{u}^{(1)} = \bar{s}_u, \quad \dot{\bar{u}} = \bar{p}_X, \quad (94)$$

with the initial conditions

$$\bar{u}(X, 0) = \bar{u}_0, \quad \bar{s}_u(X, 0) = \bar{s}_{u0}, \quad \bar{p}_X(X, 0) = \dot{\bar{u}}_0. \quad (95)$$

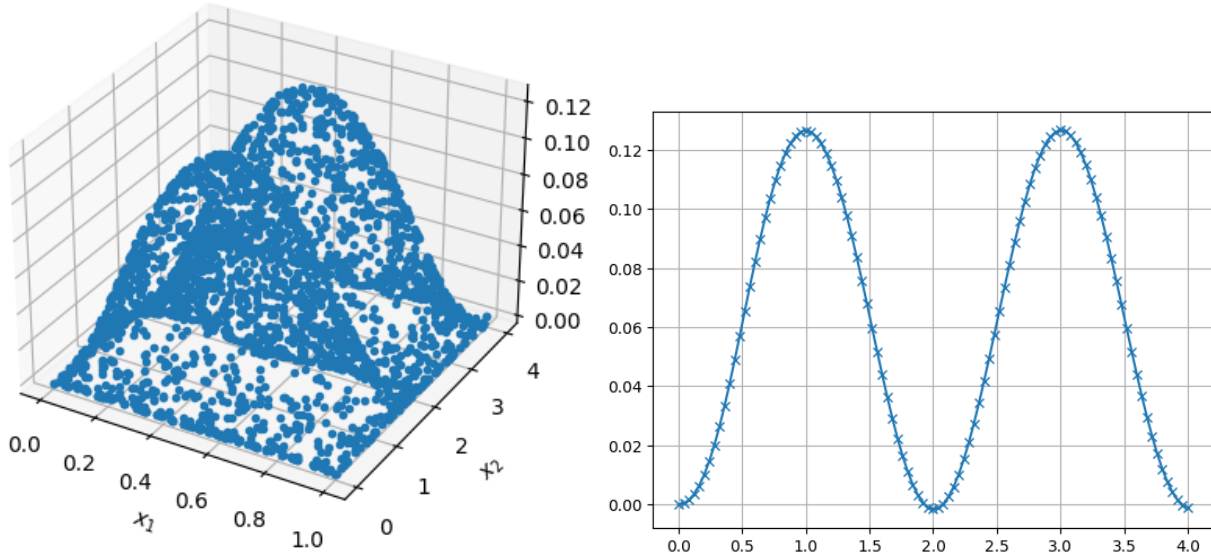


Figure 35: DDE-T. Pinned-pinned bar. Step 200,000: Shape (left), midspan displacement (right), visually quasi-perfect. ★ Remark 5.13, Optimal capacity. Remark 5.16, Unstable solution. Remark 5.20, Avoiding static solution. Section 5.3.2, Form 2a. Network: ★ Remarks 5.3, 5.5, $T=4$, $W=64$, $H=4$, $n_{out}=2$, He-uniform initializer, 12,802 parameters, ★ random grid. Training: ★ Remark 5.8 LRS 3 (NCA), $init_lr=0.01$. $n_cycles=1$, $N_steps=200,000$. ★ Lowest total loss $0.537e-06$, Step 192,000 (sum of 6 losses). Total GPU time 640 sec. ● Figure 36, early stopping at Step 146,000, good trade-off. ▷ Figures 29-30, regular grid, static solution (same LRS 3 and $init_lr$). Figure 15, 4,802 parameters, good solution. Figure 14, 1,218 parameters, very-good solution. (2384R2a-1)

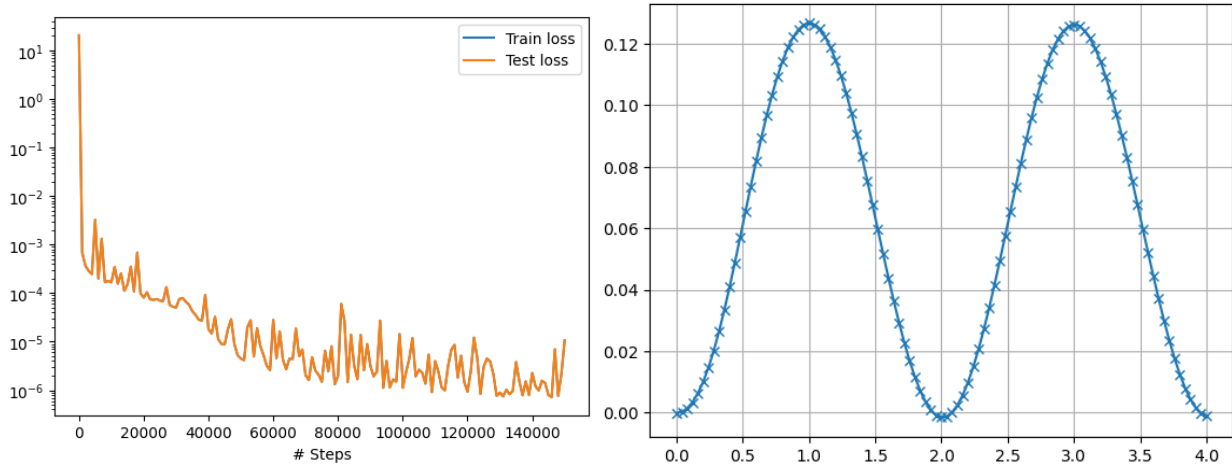


Figure 36: DDE-T. Pinned-pinned bar. Left: Loss function. Right: Step 146,000, midspan displacement (right), $damping\%=0.3\%$, Quasi-perfect. ★ Section 5.3.2, Form 2a. Network: ★ Remarks 5.3, 5.5, $T=4$, $W=64$, $H=4$, $n_{out}=2$, He-uniform initializer, 12,802 parameters, ★ random grid. Training: ★ Remark 5.8 LRS 3 (NCA), $init_lr=0.01$. ★ Total loss $0.722e-06$, Step 146,000 (sum of 6 losses). Total GPU time 442 sec. ● Figure 35, running through to Step 200,000. ▷ Figures 29-30, regular grid, static solution (same LRS 3 and $init_lr$). Figure 15, 4,802 parameters, good solution. Figure 14, 1,218 parameters, very-good solution. ▷ Figure 5, reference solution to compare. (2384R2d-1)

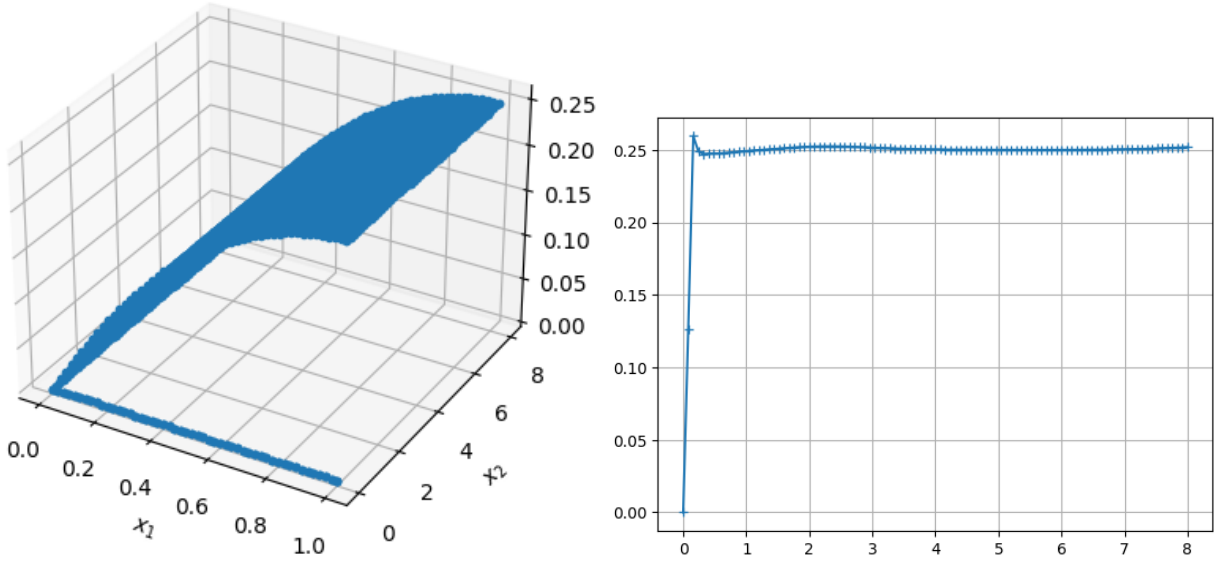


Figure 37: DDE-T. Pinned-free bar. He-uniform initializer. ★ Static shape (left), free-end displacement (right), Step 25,000, end of Cycle 1. Section 5.3.2, Form 2a. Network: Remarks 5.3, 5.5, $T=8$, $W=64$, $H=4$, $n_{out}=2$, He-uniform initializer, 12,802 parameters, regular grid. Training: Remark 5.8, LRS 3, $init_lr=0.005$. ● Figure 38, same model, LRS 3, $init_lr=0.005$, random grid, quasi-perfect solution. (2395R3a-1)

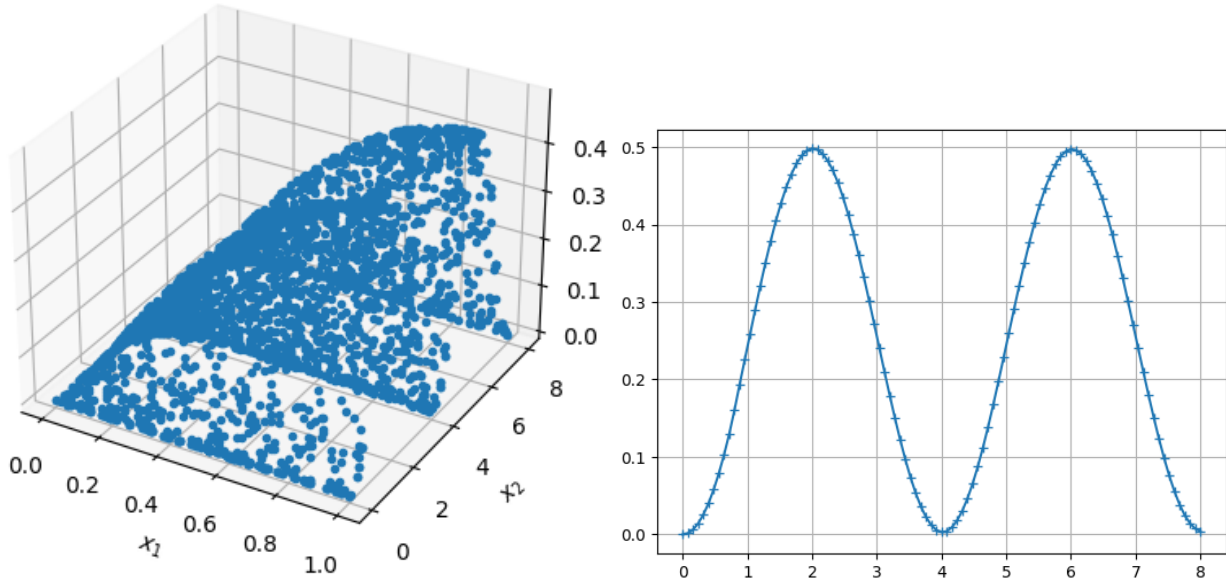


Figure 38: DDE-T. Pinned-free bar. He-uniform initializer. ★ Step 100,000: Shape (left), free-end displacement (right), damping%=0.14%, Quasi-perfect. Section 5.3.2, Form 2a. Network: Remarks 5.3, 5.5, $T=8$, $W=64$, $H=4$, $n_{out}=2$, He-uniform initializer, 12,802 parameters, random grid. Training: Remark 5.8, LRS 3, $init_lr=0.005$, Cycle 3 lowest loss $2.472e-06$, GPU time 318 sec. (2395R3b-1) ● (Cycle 5 lowest loss $1.268e-06$, GPU time 605 sec (Deterministic mode). (2395R3b.3)) Figure 37, same model, LRS 3, $init_lr=0.005$, regular grid, static solution. ▷ Figure 27 Form 1, static solutions. Figure 45, Form 3, static and quasi-perfect solutions. ▷ Figure 5, reference solution to compare.

In the numerical examples, we use homogeneous initial conditions:

$$\bar{u}(X, 0) = 0, \quad \bar{s}_u(X, 0) = 0, \quad \bar{p}_X(X, 0) = 0. \quad (96)$$

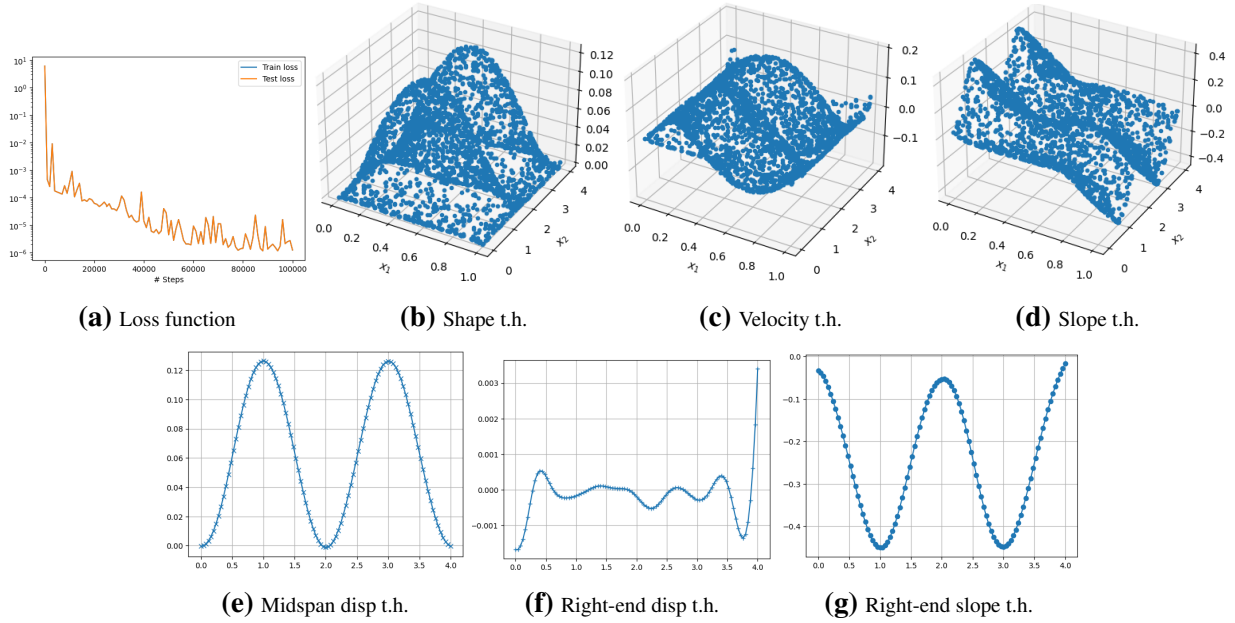


Figure 39: **DDE-T**. Pinned-pinned bar. Step 88,000: “t.h.” = time history. SubFig. 39e, midspan displacement t.h., damping%=0.1%, *Quasi-perfect*. ★ Section 5.3.2, Form 3. Network: ★ Remarks 5.3, 5.5, T=4, W=64, H=4, n_out=3, He-uniform initializer, 12,867 parameters, ★ random grid. Training: ★ Remark 5.8 LRS 3 (NCA), init_lr=0.01. ★ Total loss 1.179e-06, (sum of 7 losses). Total GPU time 278 sec. • The above is a good trade-off with the results in Figures 35-36. ▷ Figure 5, reference solution to compare. (2384R2e-1)

Figures 40-41 for the axial motion of a *pinned-pinned bar* were obtained using Form 3, VCA (Remark 5.7), network with 1,251 parameters, regular grid, for 200,000 steps, and resulted in the lowest total loss of 4.31e-06 and GPU time of 309 sec.

For the same pinned-pinned bar, Form 3, network with 1,251 parameters, but VCA with ELRS (Remark 5.9) and random grid for 400,000 steps, Figures 42, 43, 44, yielded a solution with a total loss of 1.25e-06 (3 times smaller compared to 4.31e-06 in Figures 40-41) and total GPU time of 598 sec (less than 2 times longer than 309 sec in Figures 40-41). See Remark 5.5 regarding the lowest total loss achieved, 0.518e-06, for axial motion of a pinned-pinned bar.

While *symmetry* can be observed in the *quasi-perfect* midspan-displacement time history in Figure 42, a lack of symmetry was revealed in the computed slope (space derivative) time history of the right pinned-end in Figure 44, which showed a shift downward by 0.03 (since the slope must be zero at time $t = 0$) and a clear departure from symmetry near time $t = 4$.

Compared to Form 1 used in Figure 21, with a network of 12,737 parameters, CA (Remark 5.6) over 200,000 steps, with a total GPU time of 621 sec, Form 3 used in Figure 42 with 1,251 parameters and a total GPU time of 598 sec is still 4% more efficient, despite running over twice the number of steps to 400,000.

Remark 5.21. Switching from Form 2a to Form 3, **DDE-T**. To obtain results using Form 3 in **DDE-T**, the starting point was to use the same parameters (with init_lr=0.005, He-uniform initializer) used for Form 2a in **DDE-T** that resulted in Figure 38, with only Form 2a changed to Form 3; the result was a pre-static

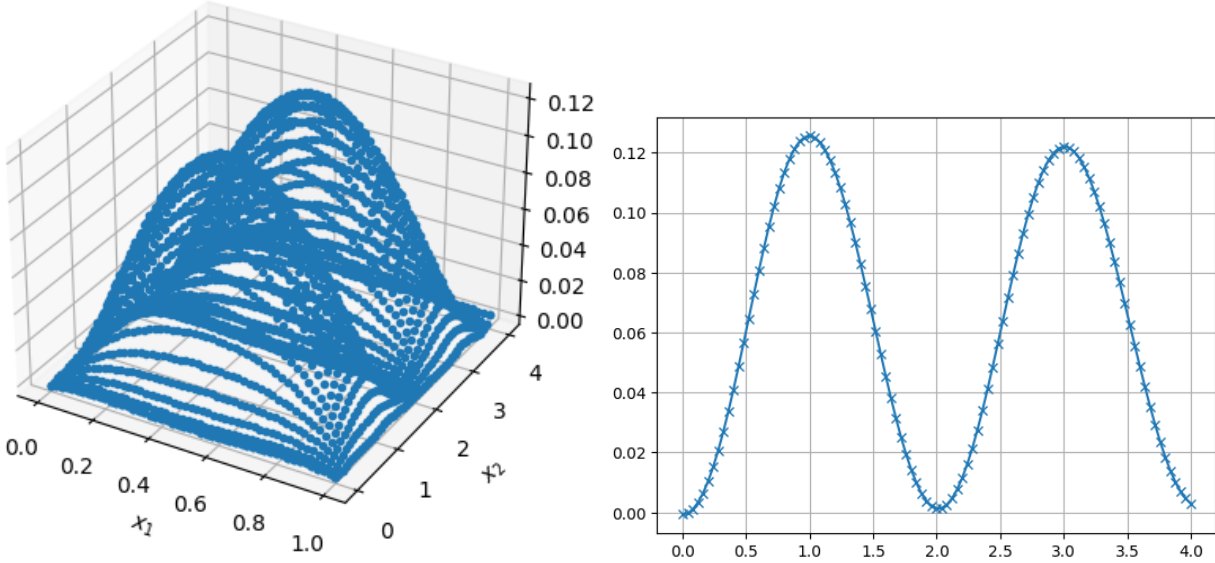


Figure 40: DDE-T. Pinned-pinned bar, VCA. Shape (left), midspan displacement, Step 200,000 (right), waves, small damping. ★ Section 5.3.4, Form 3. Remark 5.14, Damping. Network: Remarks 5.3, 5.5, $T=4$, $W=32$, $H=2$, $n_{out}=2$, He-uniform initializer, 1,251 parameters, ★ regular grid. Training: ★ Remark 5.7, LRS 2 (VCA), $init_lr=[0.04, 0.03, 0.02, 0.01, 0.005]$. ★ Lowest total loss $4.31e-06$, Step 200,000 (sum of 7 losses). ★ Total GPU time 309 sec. ● Figure 41, velocity, slope. ▷ Figure 9, CA, Form 2a, same model and $init_lr=0.04$, static solution. Figure 10, VCA, Form 2a, same model and $init_lr$ sequence, waves, small damping. (23821R1c-1)

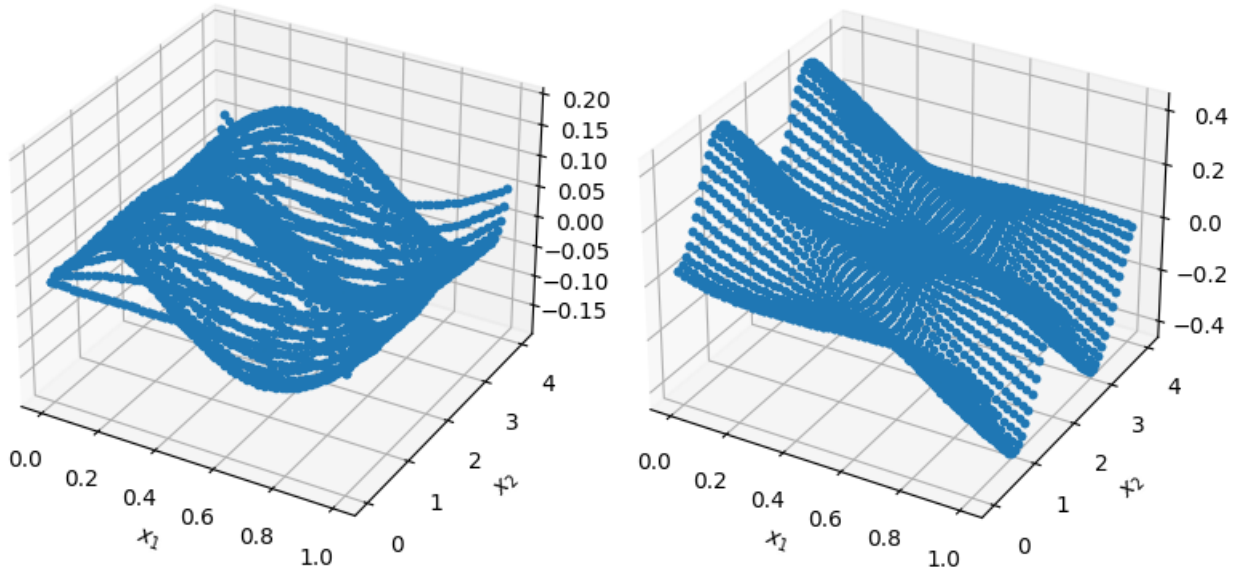


Figure 41: DDE-T. Pinned-pinned bar, VCA. Velocity (left), slope (right), Step 200,000, waves, small damping. ★ Section 5.3.4, Form 3. Network: ★ Remarks 5.3, 5.5, $T=4$, $W=32$, $H=2$, $n_{out}=2$, He-uniform initializer, 1,251 parameters, ★ regular grid. Training: ★ Remark 5.7, LRS 2 (VCA), $init_lr=[0.04, 0.03, 0.02, 0.01, 0.005]$. ● Figure 40, VCA, Form 3, same model and $init_lr$ sequence, waves with small damping. ▷ Figure 9, CA, Form 2a, same model, $init_lr=0.04$, static solution. Figure 10, VCA, Form 2a, waves with small damping. (23821R1c-2)

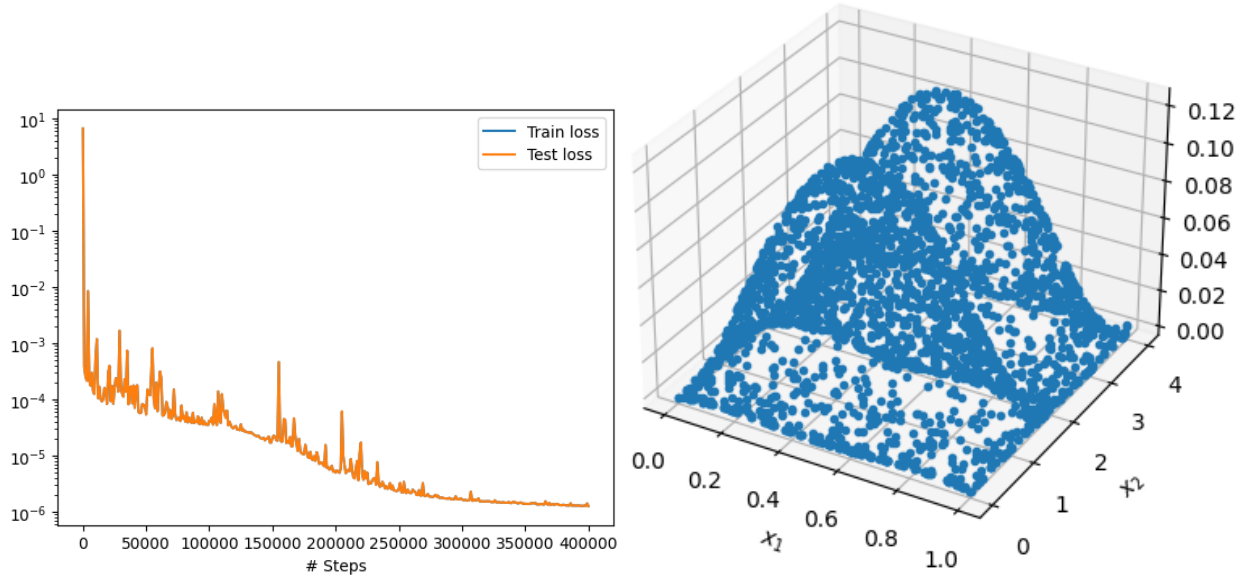


Figure 42: **DDE-T**. Pinned-pinned bar. Loss function (left), shape, Step 400,000 (right). ★ Remark 5.14, Damping. Section 5.3.4, Form 3. Network: Remarks 5.3, 5.5, $T=4$, $W=32$, $H=2$, $n_{\text{out}}=3$, He-uniform initializer, 1,251 parameters, random grid. Training: ★ Remarks 5.7 (LRS 2), 5.9 (ELRS), $\text{init_lr}=[0.04, 0.03, 0.02, 0.01, 0.01, 0.005]$ Cycles 1-6 (VCA); Cycles 7-9 (NCA). ★ Lowest total loss $1.25\text{e-}06$, Step 400,000 (sum of 7 losses). ★ Total GPU time 598 sec. • Figure 43, velocity, midspan displacement, Step 400,000. Figure 44, slope, Step 400,000. ▷ Figure 35, total loss $0.537\text{e-}06$. ▷ Figure 5, reference solution to compare. (23824R1-1)

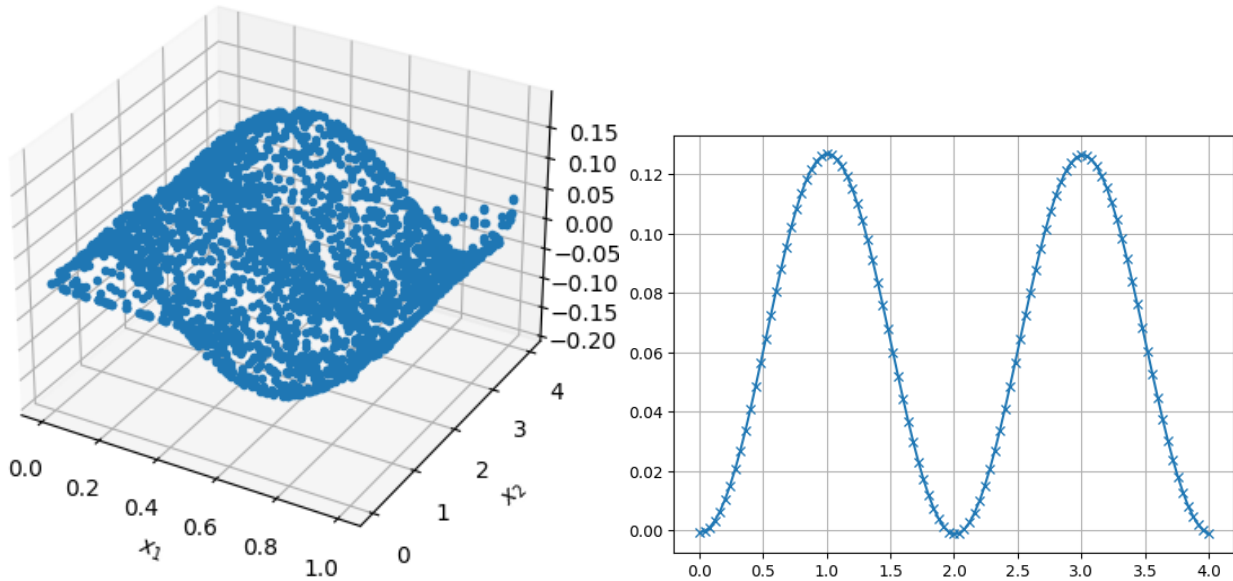


Figure 43: **DDE-T**. Pinned-pinned bar. ★ Velocity (left), visually quasi-perfect midspan displacement, Step 400,000 (right). ★ Section 5.3.4, Form 3. Network: Remarks 5.3, 5.5, $T=4$, $W=32$, $H=2$, $n_{\text{out}}=3$, He-uniform initializer, 1,251 parameters, random grid. Training: Remark 5.7 (LRS 2), Remark 5.9 (ELRS), $\text{init_lr}=[0.04, 0.03, 0.02, 0.01, 0.01, 0.005]$ Cycles 1-6 (VCA); Cycles 7-9 (NCA). • Figure 42, loss function, shape, Step 400,000, lowest total loss, GPU time. Figure 44, slope, Step 400,000. (23824R1-2)

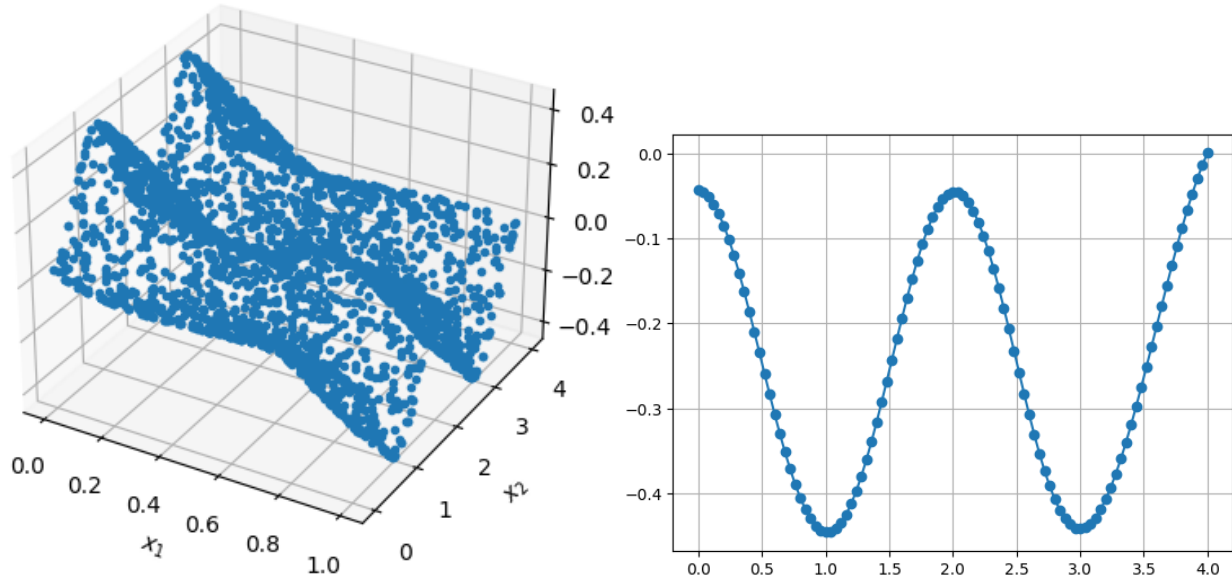


Figure 44: [DDE-T](#). Pinned-pinned bar. ★ Slope (left), right-pinned-end slope, Step 400,000 (right). ★ Section 5.3.4, Form 3. Network: Remark 5.3, 5.5, $T=4$, $W=32$, $H=2$, $n_{out}=3$, He-uniform initializer, 1,251 parameters, random grid. Training: ★ Remark 5.7 (LRS 2), 5.9 (ELRS), $init_lr=[0.04, 0.03, 0.02, 0.01, 0.01, 0.005]$ Cycles 1-6 (VCA); Cycles 7-9 (NCA). ● Figure 42, loss function, shape, Step 400,000, lowest total loss, GPU time. Figure 43, velocity, midspan displacement, Step 400,000. (23824R1-3)

solution shown in SubFigs 45a-45b. Indeed, increasing $init_lr$ to 0.01 resulted in a static solution shown in SubFigs 45c-45d, and reducing $init_lr$ to 0.001 was not enough to avoid a pre-static solution, SubFigs 45e-45f. Returning $init_lr$ to 0.005 and switching from He-uniform to Glorot-uniform initializer resulted in a very-good free-end displacement with a Cycle 5 lowest loss of $1.851e-06$ at Step 187,000, as shown in SubFigs 45g-45h. Decreasing $init_lr$ to 0.001, maintaining the Glorot-uniform initialization, then resulted in a quasi-perfect free-end displacement, albeit with a higher Cycle 5 lowest loss of $5.877e-06$ at Step 200,000, as shown in SubFigs 45i-45j.

It is important to note that the above results do not absolutely imply the superiority of the Glorot initializer over the He initializer, but as noted before in Remark 5.11, the Glorot initializer is equivalent to a smaller learning rate compared to the He initializer. ■

Remark 5.22. Efficiency: Form 1 vs Form 2a vs Form 3. [DDE-T](#) vs [JAX](#). First we used our [DDE-T](#) script. Based on our numerical experiments on the axial motion of a bar, Form 3 is computationally more efficient than Form 2a, which is itself computationally more efficient than Form 1.

For the *pinned-pinned* bar, going from Form 3 (531 sec) to Form 2a (561 sec) requires 6% more computational time. Going from Form 2a to Form 1 (624 sec) requires 11% more computational time. Going from Form 3 to Form 1 requires 18% more computational time.¹⁰ For the *pinned-pinned* bar, Form 1 using the Hessian to compute the 2nd derivative has an average GPU time of 624 sec (RunIDs 2388R5a,b,c). Switching from a Hessian to two Jacobians increased the average GPU time to 693 sec, or 11%. With the Form 3 GPU time remaining the same at 531 sec, going from Form 3 to Form 1 using two Jacobians requires

¹⁰For each form, three runs were carried out to obtain the average GPU time. The additional GPU time required for moving from one form to another was based on these average GPU times. For the pinned-pinned bar, see RunIDs 2388R2a,b,c for Form 3 (531 sec), RunIDs 2388R6a,b,c for Form 2a (561 sec), and RunIDs 23101R3a,b,c for Form 1 with Hessian (624 sec).

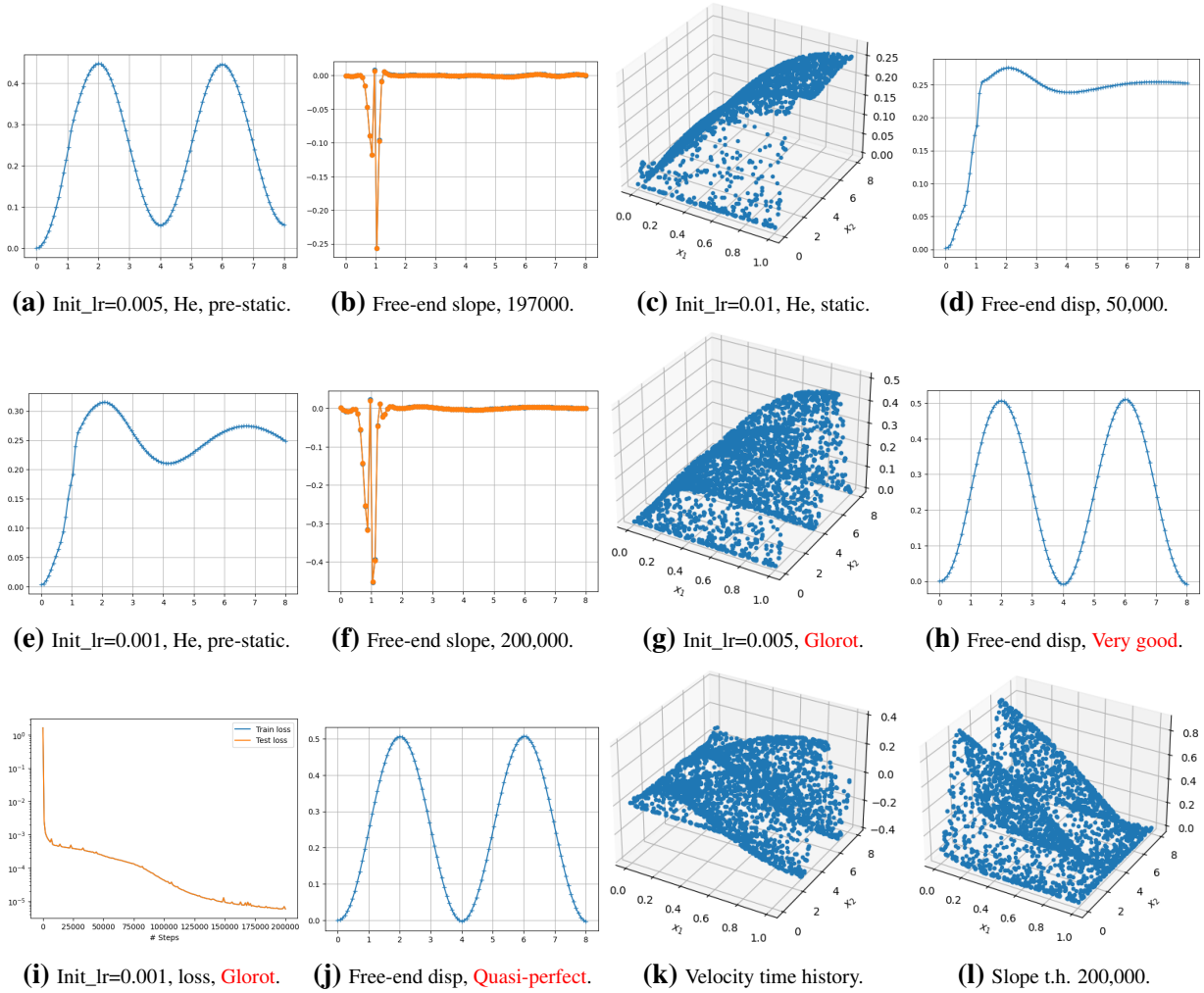
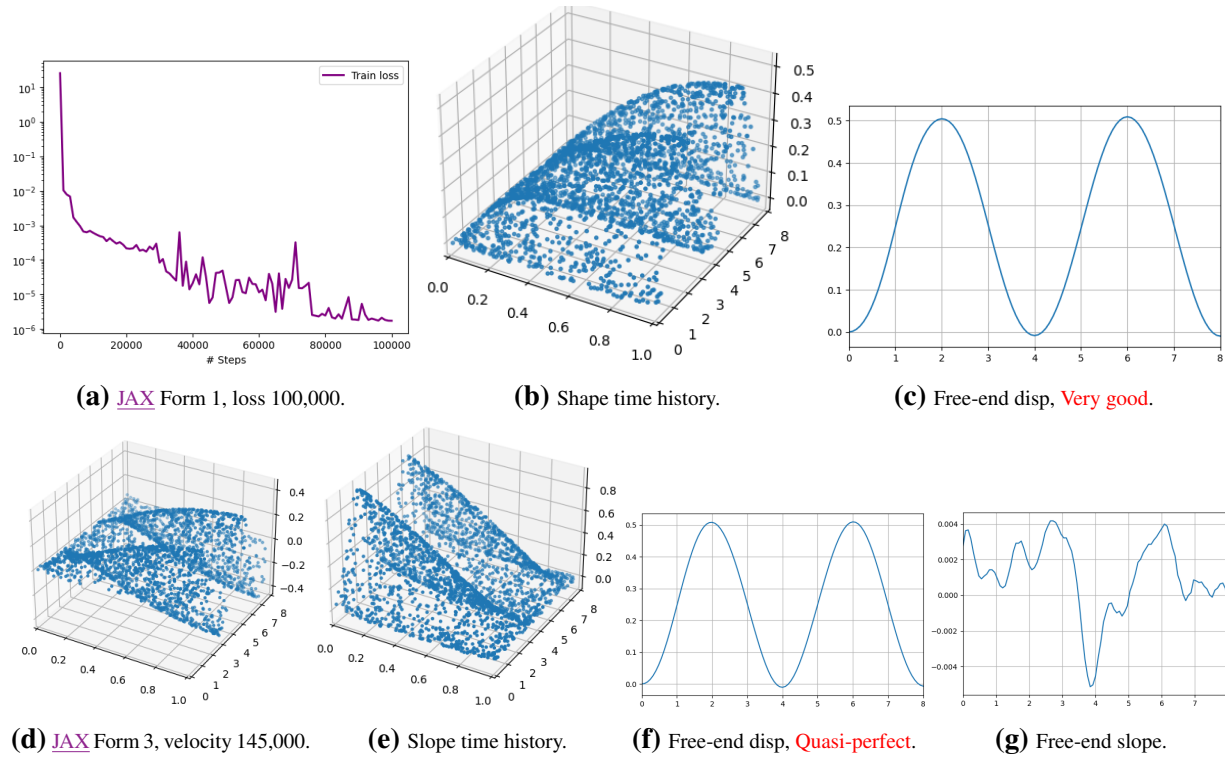


Figure 45: **DDE-T**. Pinned-free bar, **Form 3** (Section 5.3.4). Remark 5.21, Switch Form 2a to Form 3. • SubFigs 45a-45b, *Pre-static solution*. Step 197,000: (45a) Free-end displacement with velocity discontinuity at $t=1$ and upward shift. (45b) Free-end slope jump with large amplitude oscillations (negative space derivative) starting before $t=1$. ★ Section 5.3.4, **Form 3**. *Network*: Remark 5.3, 5.5, $T=8$, $W=64$, $H=4$, $n_{\text{out}}=3$, **He-uniform** initializer, 12,867 parameters, *random grid*. *Training*: ★ Remark 5.8 (LRS 3, NCA), $\text{init_lr}=0.005$, GPU time 537 sec. (2395R3d.1) • SubFigs 45c-45d, *Static shape*, free-end disp, Step 50,000, $\text{init_lr}=0.01$, He-uniform. (2395R3d.2) • SubFigs 45e-45f, *pre-static* free-end disp, slope (space derivative), Step 200,000, $\text{init_lr}=0.001$, He-uniform. (2395R3d.5) • SubFigs 45g-45h, lowest loss $1.851\text{e-}06$, Step 187,000, shape, **Very good** free-end disp, **Glorot-uniform** initializer (Remark 5.11), $\text{init_lr}=0.005$, $\text{damping}\%=-0.7\%$. (2395R3d.3) ★ SubFigs 45i-45l, Step 200,000: (45i) Lowest loss $5.877\text{e-}06$, $\text{init_lr}=0.001$, **Glorot-uniform**, $\text{damping}\%=-0.13\%$, (45j) **Quasi-perfect** free-end disp, (45k) Velocity time history (t.h.), (45l) Slope (space derivative) t.h., GPU 533 sec (Deterministic mode). (2395R3d.4) • Figure 38, **Form 2a**, same model parameters as SubFigs 45a-45b, **Quasi-perfect** free-end disp. ▷ Figure 5, reference solution to compare.



(a) JAX Form 1, loss 100,000.

(b) Shape time history.

(c) Free-end disp, **Very good**.

(d) JAX Form 3, velocity 145,000.

(e) Slope time history.

(f) Free-end disp, **Quasi-perfect**.

(g) Free-end slope.

Figure 46: JAX. Pinned-free bar. SubFigs 46a-46c, **Form 1**: (46a) Step 100,000, Total loss $1.749\text{e-}06$ (sum of 5 losses), Average loss $0.350\text{e-}06$. *Network*: Remark 5.3, 5.5, $T=8$, $W=64$, $H=4$, $n_{\text{out}}=1$, **Uniform** initializer, 12,737 parameters, *random* grid. *Training*: ★ Remark 5.8 (LRS 4), $\text{init_lr}=0.002$, $\text{factor_lr} = [0.2, 0.2, 0.2, 0.2, 0.2, 1, 1, 1, 1]$. (46b) Shape time history (t.h.). Damping%=-0.94%, (46c) **Very good** free-end displacement. (23916R1a.8) ● **Form 3**: (46d) Step 145,000, velocity t.h., Total loss $4.063\text{e-}06$, Average loss $0.580\text{e-}06$. *Network*: Same as the above, except $n_{\text{out}}=3$, 12,867 parameters. *Training*: Same as the above. (46e) Slope (space derivative) t.h. Damping%=-0.3%, (46f) **Quasi-perfect** free-end disp t.h.. (46g) Free-end slope (space derivative) t.h., peak-to-peak amplitude $8.658\text{e-}03$. (23916R1a.7.2)

31% more computational time.

For the *pinned-free bar*, the results (obtained in Deterministic mode) in Figure 27 (Form 1, 655 sec), Figure 38 (Form 2a, 605 sec), and Figure 45 (Form 3, 533 sec), indicate that going from Form 3 to Form 2a requires 14% more computational time, going from Form 2a to Form 1 requires 8% more computational time, going from Form 3 to Form 1 requires 23% more computational time. The **DDE-T** results in Non-deterministic mode are tabulated in Table 1, which is explained below. These percentages would change with the number of derivatives on a PDE system, with the axial motion having the lowest number of derivatives considered here, with two space derivatives and two time derivatives.

After obtaining the above results for the pinned-free bar with our **DDE-T** script, we ran the same cases with our **JAX** script to compare Form 1 to Form 3. Using JAX Form 3, the total loss of, 5.135e-06 (average loss 0.734e-06) at Step 97000 after 357 sec (at Step 100,000, which is before Step 145,000 the results at which are shown in SubFigs 46d-46g) is a good trade-off for the loss 5.877e-06 at Step 200,000 (end of Cycle 5) after 533 sec using **DDE-T** Form 3 in SubFigs 45i-45l. In SubFigs 46d-46g, it took 529 sec to train 150,000 steps of **JAX** Form 3 to get a loss of 4.104e-06 and Cycle 4 lowest loss of 4.063e-06 at Step 145000.

All results depend crucially on the learning-rate schedule and the initializer used, meaning in principle one could conceivably design a learning-rate schedule with an appropriate initializer for DDE-T Form 3 to reach a total loss below 4.104e-06 in 150000 steps or less. Hence in the end, the GPU time for a fixed number of steps is important and more meaningful for comparing between two different implementations.

The GPU times for **DDE-T** and for **JAX** for 200,000 training steps in each form in Non-deterministic mode are tabulated in Table 1, which shows that JAX Form 1 is faster than JAX Form 2a, which is faster than JAX Form 3, the *opposite* of DDE-T.¹¹ The results in Table 1 show that our **DDE-T** script is faster than our **JAX** script. Using DDE-T GPU time as reference, DDE-T Form 1 (529 s) is more efficient than JAX Form 1 (575 s) by 9%, whereas DDE-T Form 2a (498 s) is more efficient than JAX Form 2a (644 s) by 29%, and DDE-T Form 3 (488 sec) is more efficient than JAX Form 3 (733 sec) by 50%. ■

Table 1: *Pinned-free bar*. Remark 5.22, Efficiency, **DDE-T** vs **JAX**. GPU time for 200,000 training steps. All ran in *Non-deterministic* mode. Each number represents the average GPU time of three runs (see Footnote 11). *Network:* Remark 5.3, 5.5, T=8, W=64, H=4.

	Form 1	Form 2a	Form 3
DDE-T	529 sec	498 sec	488 sec
JAX	575 sec	644 sec	733 sec

Remark 5.23. **JAX** *Deterministic slightly faster than Non-deterministic*. Unlike **DDE-T** for which running in deterministic mode carries an average penalty of about 4% in GPU time compared to non-deterministic mode (or 10% for a single case as noted in Remark 5.15), it is surprising to note that **JAX** in deterministic mode is more efficient than in non-deterministic mode. Re-running each **JAX** non-deterministic case in Table 1 three times in deterministic mode, the corresponding average GPU times are: 550 sec (JAX Form 1,

¹¹Table 1. For **DDE-T Form 1**, the average GPU time of three runs was 529 sec: RunIDs 2398R2a.3 (538 s), 2398R2a.4 (523 s), 2398R2a.5 (525 s). **DDE-T Form 2a**, average GPU time 498 sec: 2398R2a.6 (503 s), 2398R2a.6 (504 s), 2398R2a.6 (487 s). **DDE-T Form 3**, average GPU time 488 sec: 2398R2a.9 (499 s), 2398R2a.10 (477 s), 2398R2a.11 (488 s). • For **JAX Form 1**, average GPU time 575 sec: 23916R1a8 (588 s), 23.9.16 R1a.8.3 (554 s), 23.9.16 R1a.8.4 (583 s). **JAX Form 2a**, average GPU time 644 sec: 231024R2c (618 s), 231025R2b (640 s), 231025R2c (675 s). **JAX Form 3**, average GPU time 733 sec: 23916R1a7 (701 s), 23916R1a7.2 (751 s), 23916R1a7.3 (747 s).

or 4% less than non-deterministic), 628 sec (JAX Form 2a, or 2.5% less), 689 sec (JAX Form 3, or 6% less). ■

6 Closure

Following up our review of deep learning applied to computational mechanics [1], we developed novel PINN formulations for nonlinear dynamics governed by partial-differential-algebraic equations (PDAEs), exemplified by the equations of motion of a geometrically-exact Kirchhoff rod in higher-level forms, initially developed to address the pathological problems of shift and amplification encountered with [DDE-T](#), which is likely the most well-documented among PINN frameworks.

For the static-solution problem, we consider the use of barrier functions, which themselves represent a novel application in PINN, to prevent the training iterate to get close to a static solution. Even though the barrier function is an elegant method, it still has room for improvement, while simpler methods such as reducing the model capacity (using lower number of parameters), use a different initializer, and smaller learning rate led to satisfactory results.

Another novelty is to apply PINN directly to the highest-level momentum form (balance of momenta) as it would save much time and effort to hand derive from the highest-level form to the lowest-level form through to computational formulation and implementation as done in traditional approach.

In parallel with using [DDE-T](#), we developed a script based on [JAX](#), which does not exhibit the pathological problems of [DDE-T](#), it is slower than [DDE-T](#) in all forms tested.

To help readers reproduce our results, we normalize/standardize the training process, which is important to compare different training strategies due to the large number of parameters involved. Each figure is accompanied with a caption that details all parameters used to obtain the results. The computed gradients in both [DDE-T](#) and [JAX](#) likely hold the key for the behavior (pathological problems and computational speed) observed.

Large computational efficiency with the proposed PINN formulations recently obtained for the transverse motion of the Euler-Bernoulli beam and for the geometrically-exact Kirchhoff rod will be reported in a follow-up paper.

References

1. Vu-Quoc, L., Humer, A. (2023). Deep learning applied to computational mechanics: A comprehensive review, state of the art, and the classics. *CMES-Computer Methods in Engineering & Sciences*, 137(2), 1069–1343. [CMES](#), DOI: 10.32604/cmes.2023.028130, on [arXiv:2212.08989](#) since 18 Dec 2022. 1, 3, 12, 17, 26, 30, 49
2. Lu, L., Meng, X., Mao, Z., Karniadakis, G. E. (2021). DeepXDE: A deep learning library for solving differential equations. *SIAM Review*, 63(1), 208–228. [Original website](#), [pdf](#), [arXiv:1907.04502](#). 1, 3, 14, 16
3. Dill, E. H. (1992). Kirchhoff's theory of rods. *Archive for History of Exact Sciences*, 44, 1–23. DOI 10.1007/BF00379680. 2
4. Neukirch, S., Yavari, M., Challamel, N., Thomas, O. (2021). Comparison of the Von Kármán and Kirchhoff models for the post-buckling and vibrations of elastic beams. *Journal of Theoretical, Computational and Applied Mechanics*, (May). DOI 10.5281/zenodo.4766972. 2
5. Simo, J. C. (1982). *A Consistent Formulation of Nonlinear Theories of Elastic Beams and Plates*. PhD dissertation, Civil Engineering, University of California at Berkeley, November. 2
6. Simo, J. C., Hjelmstad, K. D., Taylor, R. L. (1984). Numerical formulations of elasto-viscoplastic response of beams accounting for the effect of shear. *Computer Methods in Applied Mechanics and Engineering*, 42(3), 301–330. 2

7. Simo, J. C. (1985). A finite strain beam formulation. The three-dimensional dynamic problem. Part I. *Computer Methods in Applied Mechanics and Engineering*, 49(1), 55–70. [2](#)
8. Karniadakis, G. E., Kevrekidis, I. G., Lu, L., Perdikaris, P., Wang, S., et al. (2021). Physics-informed machine learning. *Nature Reviews Physics*, 3(6), 422–440. [Original website](#). [3](#)
9. Cuomo, S., di Cola, V. S., Giampaolo, F., Rozza, G., Raissi, M., et al. (2022). Scientific Machine Learning through Physics-Informed Neural Networks: Where we are and What's next. *Journal of Scientific Computing*, 92(3). Article No. 88, [Original website](#), [arXiv:2201.05624](#). [3](#)
10. Lagaris, I. E., Likas, A., Fotiadis, D. I. (1998). Artificial neural networks for solving ordinary and partial differential equations. *IEEE transactions on neural networks*, 9(5), 987–1000. [Original website](#). [3](#)
11. Lagaris, I. E., Likas, A. C., Papageorgiou, D. G. (2000). Neural-network methods for boundary value problems with irregular boundaries. *IEEE Transactions on Neural Networks*, 11(5), 1041–1049. [Original website](#). [3](#)
12. Lavin, A., Zenil, H., Paige, B., Krakauer, D., Gottschlich, J., et al. (2021). Simulation Intelligence: Towards a New Generation of Scientific Methods. [arXiv:2112.03235](#). [3](#)
13. Bazmara, M., Silani, M., Mianroodi, M., Sheibani, M. (2023). Physics-informed neural networks for nonlinear bending of 3D functionally graded beam. *Structures*, 49, 152–162. [DOI: 10.1016/j.istruc.2023.01.115](#). [3](#)
14. Zienkiewicz, O. C., Taylor, R. L., Zhu, J. Z. (2013). *The Finite Element Method: Its Basis & Fundamentals*. 7th edition. Butterworth-Heinemann. [FEAPpv, Project page](#), [Internet archived 2023.03.31](#). [3](#)
15. Zienkiewicz, O. C., Taylor, R. L., Fox, D. D. (2014). *The Finite Element Method for Solid & Structural Mechanics*. 7th edition. Elsevier India. [3](#)
16. Zienkiewicz, O. C., Taylor, R. L., Nithiarasu, P. (2013). *The Finite Element Method for Fluid Dynamics*. 7th edition. Butterworth-Heinemann. [3](#)
17. Taylor, R. L. (2020). *FEAP: A Finite Element Analysis Program*. Version 8.6 Theory Manual. Technical report, University of California at Berkeley, CA 94720. [Internet archived 2022.06.30](#). [FEAP Wiki](#). [Project page](#), [Internet archived 2023.03.31](#). [3](#)
18. Schoeberl, J. (2014). *C++11 Implementation of Finite Elements in NGSolve*. Technical report ASC No. 30/2014, Institute for Analysis and Scientific Computing, Vienna University of Technology, TU Wien. [Internet archived 2022.08.03](#). [Netgen/NGSolve website](#). [3](#)
19. Simo, J., Vu-Quoc, L. (1986). On the dynamics of flexible beams under large overall motions—The plane case: Part I. *ASME Journal of Applied Mechanics*, 53, 849–854. Dec. [9](#), [10](#)
20. Reissner, E. (1972). On one-dimensional finite-strain beam theory: the plane problem. *Zeitschrift für angewandte Mathematik und Physik ZAMP*, 23(5), 795–804. [10](#)
21. Nafis, N. (2021). The story behind ‘random.seed(42)’ in machine learning. *Geek Culture, Medium*, (Aug 3). [Original website](#). See also Leticia B. (2018), [The Story of Seed\(42\)](#). [17](#)
22. Nocedal, J., Wright, S. (2006). *Numerical Optimization*. Springer, New York. 2nd edition. [56](#)
23. Fiacco, A. V., McCormick, G. P. (1990). *Nonlinear Programming: Sequential Unconstrained Minimization Techniques*. SIAM, Philadelphia. Series *Classics in Applied Mathematics*. [56](#)
24. Frisch, K. R. (1955). *The logarithmic potential method of convex programming*. Technical report. University Institute of Economics, Oslo, Norway. [56](#)
25. Frisch, K. R. (1954). *Principles of Linear Programming—With Particular Reference to the Double Gradient Form of the Logarithmic Potential Method*. Technical report. University Institute of Economics, Oslo, Norway. [56](#)
26. Carroll, C. W. (1959). An Operations Research Approach to the Economic Optimization of a Kraft Pulping Process. Ph.D. dissertation, Institute of Paper Chemistry, Appleton, Wisconsin. [56](#)

27. Carroll, C. W. (1961). The Created Response Surface Technique for Optimizing Nonlinear Restrained Systems. *Operations Research*, 9(2), 169–184. [56](#)

Appendices

1 Analysis of time shift and amplification

First, we analyze the computed solution of Form 1 of the axial motion of a pinned-pinned elastic bar with distributed axial force (Section 5.3.1), with $\bar{x} \approx \bar{X}$:

$$\text{PDE: } \bar{u}^{(2)} + \bar{f}_x = \ddot{\bar{u}}, \quad (64)$$

$$\text{BCs: } \bar{u}(0, \bar{t}) = \bar{u}(1, \bar{t}) = 0, \quad (85)$$

$$\text{ICs: } \bar{u}(\bar{x}, 0) = 0, \quad \dot{\bar{u}}(\bar{x}, 0) = 0. \quad (87)$$

To alleviate the notation, we omit the overbar designating non-dimensionalization on (x, t) , while keeping the overbar in \bar{u} and \bar{f}_x . Let the computed solution $\tilde{u}(x, t)$ be related to the exact solution $\bar{u}(x, t)$ by (see Figures 22-23):

$$\tilde{u}(x, t) = \alpha \bar{u}(x, t - \delta) + c \Rightarrow \bar{u}(x, t) = \frac{1}{\alpha} [\tilde{u}(x, t + \delta) - c], \quad (97)$$

where α is the amplification parameter, δ the time shift parameter, and c the vertical shift parameter. These are the three *hidden* parameters, in addition to the network parameters, for the training to adjust to reduce the loss. Figure 23 shows that as the shift and amplification (scaled from their true values in Table 2) increase, the total loss continues to decrease during training.

Table 2: Pinned-pinned bar. Form 1. Section 1, Analysis. Unscaled shift-amplification parameters (δ, c, α), with \mathcal{A} being constant, initial velocity, left-end displacement versus checkpoint training step number. • Figure 23, scaled shift-amplification parameters and initial velocity increase with training, using $p_{\text{scaled}} = \pm(p - p_{25000}) * k_p > 0$, where p_{scaled} is the positive scaled parameter p , with p_{25000} the value of p at Step 25000, and k_p a selected scale factor for p : $k_\delta = 10$, $k_c = 100$, $k_{(\alpha\mathcal{A})} = 10$, $k_{\text{Init vel}} = 10$.

Step	Time shift δ	Vertical shift c	Amplitude $\alpha\mathcal{A}$	Initial velocity	Left-end disp
25000	0	0.00973727	0.08445985	0.01150370	0.00973727
50000	0.107	-0.00462352	0.13343337	-0.06753206	-0.00094142
100000	0.146	-0.00861757	0.14141834	-0.09649991	-0.00139512
150000	0.168	-0.01143161	0.14696970	-0.11479854	-0.00152922
200000	0.184	-0.01377921	0.15177655	-0.12892485	-0.00155308
250000	0.196	-0.01580278	0.15583168	-0.14010072	-0.00157554
300000	0.204	-0.01743147	0.15909590	-0.14862418	-0.00158554
350000	0.212	-0.01873142	0.16170362	-0.15547872	-0.00158999
400000	0.216	-0.01975145	0.16374922	-0.16018747	-0.00159215

The peak-to-peak amplitude of \bar{u} (if known), or of a computed quasi-perfect solution, used as a reference is denoted by \mathcal{A} , so that $\alpha\mathcal{A}$ is the peak-to-peak amplitude of the computed solution \tilde{u} (Figure 22).

The space and time derivatives of $\tilde{u}(x, t)$ are

$$\tilde{u}_{xx}(x, t) = \alpha \tilde{u}_{xx}(x, t - \delta) \Rightarrow \tilde{u}_{xx}(x, t) = \frac{1}{\alpha} \tilde{u}_{xx}(x, t + \delta), \quad (98)$$

$$\tilde{u}_t(x, t) = \frac{1}{\alpha} \tilde{u}_t(x, t + \delta), \quad \tilde{u}_{tt}(x, t) = \frac{1}{\alpha} \tilde{u}_{tt}(x, t + \delta), \quad (99)$$

which when substituted in Eq. (64) yield

$$\check{u}_{xx}(x, t + \varsigma) + \bar{a} \bar{f}_x(x, t) = \check{u}_{tt}(x, t + \varsigma) \Rightarrow \check{u}_{xx}(x, t) + \bar{a} \bar{f}_x(x, t - \varsigma) = \check{u}_{tt}(x, t) , \quad (100)$$

with boundary conditions at $x_b = 0$ and at $x_b = 1$:

$$\bar{u}(x_b, t) = 0 = \frac{1}{\bar{a}} [\check{u}(x_b, t + \varsigma) - c] \Rightarrow \check{u}(x_b, t + \varsigma) = c , \quad (101)$$

and initial conditions:

$$\bar{u}(x, 0) = 0 = \frac{1}{\bar{a}} [\check{u}(x, \varsigma) - c] \Rightarrow \check{u}(x, \varsigma) = c , \quad (102)$$

$$\bar{u}_t(x, 0) = 0 = \frac{1}{\bar{a}} [\check{u}_t(x, \varsigma)] \Rightarrow \check{u}_t(x, \varsigma) = 0 . \quad (103)$$

Due to the computed displacement being enforced by the Dirichlet boundary condition, i.e.,

$$\check{u}(x, 0) = \epsilon \approx 0 = \bar{a} \bar{u}(x, -\varsigma) + c \Rightarrow c = -\bar{a} \bar{u}(x, -\varsigma) + \epsilon , \quad (104)$$

where ϵ is a small number or the order of 10^{-3} , the “essentially zero” for this type of network training, as shown in Table 2. So if $\varsigma > 0$ (right time shift), since $\bar{u}(x, -\varsigma) > 0$ and $\bar{a} > 0$, it follows that $c < 0$ if $\bar{a} \bar{u}(x, -\varsigma) > \epsilon$, which is a condition met in the example in Table 2.

The Neumann boundary condition was used in DeepXDE for the initial velocity, but did not enforce the time derivative of the computed solution to the “essentially zero” ϵ . Instead, the initial velocity was allowed to be non-zero:

$$\check{u}_t(x, 0) = \bar{a} \bar{u}_t(x, -\varsigma) \neq 0 , \quad (105)$$

and thus if $\varsigma > 0$, since $\bar{u}_t(x, -\varsigma) < 0$, it follows that $\check{u}_t(x, 0) < 0$, which is observed in Figure 22.

Second, we show that Form 2a of the pinned-pinned elastic bar (Section 5.3.2)

$$\text{PDE-1: } \bar{u}^{(2)} + \bar{f}_x = \dot{\bar{p}}_x , \quad (88)$$

$$\text{PDE-2: } \dot{\bar{u}} = \bar{p}_x , \quad (88)$$

$$\text{BCs: } \bar{u}(0, \bar{t}) = \bar{u}(1, \bar{t}) = 0 , \quad (85)$$

$$\text{ICs: } \bar{u}(\bar{x}, 0) = 0, \quad \bar{p}_x(x, 0) = 0 . \quad (90)$$

have neither shift nor amplification. The analysis for Form 3 is the same, and is not repeated. The explicit Dirichlet boundary condition imposed an “essentially zero” ϵ on the initial velocity of the computed solution:

$$\check{u}_t(x, 0) = \epsilon = \bar{a} \bar{u}_t(x, 0 - \varsigma) \Rightarrow \bar{u}_t(x, -\varsigma) = \epsilon / \bar{a} \approx 0 , \quad (106)$$

with $\bar{a} \neq 0$ and ς in the vicinity of zero. But the initial velocity of the exact solution is $\bar{u}_t(x, 0) = 0$. Hence, $\check{u}_t(x, -\varsigma) - \epsilon / \bar{a} = \bar{u}_t(x, 0) = 0$, and thus $s \approx 0$ (“essentially zero”). At this point $\bar{a} > 0$ can be anything. The explicit Dirichlet boundary condition also imposes an “essentially zero” ϵ on the initial displacement of the computed solution:

$$\check{u}(x, 0) = \epsilon = \bar{a} \bar{u}(x, 0 - \varsigma) + c = \bar{a} \bar{u}(x, 0) + c \Rightarrow c = \epsilon \approx 0 , \quad (107)$$

which is also an “essentially zero” (see the left-end displacement in Table 2). Now substituting $\bar{u} = \check{u} / \bar{a}$

into the above Form 2a of the PDE system to obtain:

$$\text{PDE-1: } \ddot{u}_{xx}/\mathcal{a} + \bar{f}_x = \dot{\bar{p}}_x \Rightarrow \ddot{u}_{xx} + \mathcal{a}\bar{f}_x = \mathcal{a}\dot{\bar{p}}_x, \quad (108)$$

$$\text{PDE-2: } \ddot{u}_t/\mathcal{a} = \bar{p}_x \Rightarrow \ddot{u}_t = \mathcal{a}\bar{p}_x, \quad (109)$$

$$\text{BCs: } \ddot{u}(0, t) = \ddot{u}(1, t) = 0, \quad (85)$$

$$\text{ICs: } \ddot{u}(x, 0) = 0, \quad \bar{p}_x(x, 0) = 0. \quad (90)$$

Thus \ddot{u} would be the solution of the above PDE system only if we had amplified the applied force \bar{f}_x by the amplification factor \mathcal{a} . In other words, if we did not amplify the applied force, i.e., $\mathcal{a} = 1$, then $\ddot{u} = \bar{u}$, or in practice, $\ddot{u} \approx \bar{u}$.

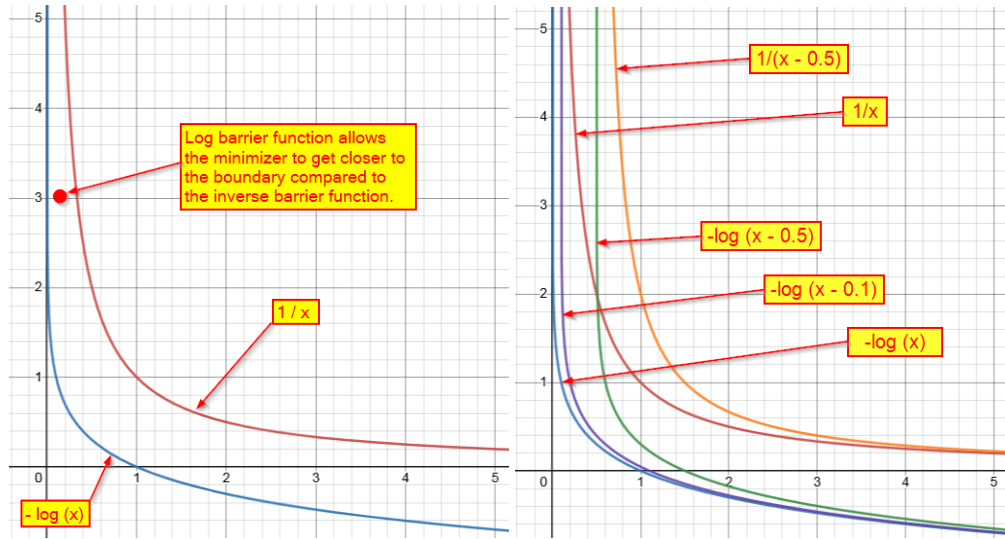


Figure 47: Inverse barrier function vs log barrier function. Appendix 2. Shifted barrier, buffer-zone depth \mathcal{d} .

2 Filtering static solutions, barrier functions

A static solution is a solution of the governing equations of motion, such as Eqs. (41)-(42), with zero inertia force on the right hand side, abstractly written based on the dynamic nonlinear differential operator $\mathcal{D}_i^{(k)}$ defined in Eq. (82) as:

$$\mathcal{D}_i^{(k)} \Big|_{n_q^{(k)}=0} = \mathcal{S}_i^{(k)}(\{\partial_X^p u_j, \partial_X^{p-1} u_j, \dots, \partial_X^0 u_j\}) = \mathcal{S}_i^{(k)}(\bar{\mathbf{u}}_{\text{st}}(X)) = 0,$$

$$k = 0, \dots, 3, \quad i = 1, \dots, n_i^{(k)}, \quad (110)$$

where $\mathcal{S}_i^{(k)}$ is a static nonlinear differential operator, which is a static part of the balance of linear momenta in PINN Form k , with $n_q^{(k)} = 0$ in Eq. (82), and $\bar{\mathbf{u}}_{\text{st}} = (\bar{u}_{\text{st}}, \bar{v}_{\text{st}})$ the exact static solutions for $\bar{\mathbf{u}} = (\bar{u}, \bar{v})$.

For convenience, the following static-operator array is defined based on the dynamic-operator array defined in Eq. (83):

$$\mathcal{S}^{(k)} = \left\{ \mathcal{S}_i^{(k)}, i = 1, \dots, n_i^{(k)} \right\}, \quad k = 0, \dots, 3. \quad (111)$$

To prevent the minimization iterate during the minimization process from reaching the static solution $\bar{\mathbf{u}}_{\text{st}}$, the loss function J can be augmented by a barrier (or penalty) function $\mathcal{L}(\bar{\mathbf{u}})$ that would drastically increase

the loss, thus creating a barrier (penalty), when the minimization iterate comes close to these solutions.

For a generic constrained nonlinear optimization problem of the form:

$$\min_x f(x) \text{ such that } 0 < x, \quad (112)$$

the nonlinear objective function $f(x)$ can be augmented by a barrier (penalty) function $\mathcal{E}(x)$:

$$J^{(\mathcal{E})} = f(x) + w \mathcal{E}(x), \text{ with} \quad (113)$$

$$\mathcal{E}(x) = \mathcal{E}^{(\text{inv})}(x) = \mathcal{E}^{(\text{i})}(x) = \frac{1}{x - \mathcal{d}}, \text{ or} \quad (114)$$

$$\mathcal{E}(x) = \mathcal{E}^{(\text{log})}(x) = \mathcal{E}^{(\text{l})}(x) = \log\left(\frac{1}{x - \mathcal{d}}\right) = -\log(x - \mathcal{d}). \quad (115)$$

where $\mathcal{E}^{(\text{inv})} = \mathcal{E}^{(\text{i})}$ is the *inverse* barrier function, $\mathcal{E}^{(\text{log})} = \mathcal{E}^{(\text{l})}$ the *logarithmic* (log) barrier function, and \mathcal{d} the shift of the origin to create a buffer zone that prevents the minimization iterate from getting too close to the feasible-domain boundary, as shown in Figure 47. Shown in the right subfigure are the cases for $\mathcal{d} = 0.1$ (for log barrier only) and $\mathcal{d} = 0.5$. While the buffer-zone depth of the inverse function gradually decreases toward the boundary, the buffer-zone depth for the shifted log function remains seemingly constant, with much slower decrease rate.

The shorter abbreviations defined as “i = inv = inverse” and “l = log = logarithm” are to be used in an expanded superscripts (mn) that determine the character of the barrier function $\mathcal{E}^{(mn)}$, with $m \in \{\text{i}, \text{l}\}$ (already defined above) and $n \in \{\text{s}, \text{p}, \text{a}\}$ (to be defined further below in the context of structural dynamics).

Let $\bar{\mathbf{u}}_{\text{st}}$ be a static solution satisfying the static PDE, i.e., the left-hand side of Eq. (82):

$$\mathcal{S}_i(\bar{\mathbf{u}}_{\text{st}}(X, t)) = 0, \text{ for } i = 1, \dots, n_i. \quad (110)$$

$$J^{(\mathcal{E})}(\bar{\mathbf{u}}) = J(\bar{\mathbf{u}}) + w \mathcal{E}(\bar{\mathbf{u}}). \quad (116)$$

Barrier functions based on a *static solution*, with superscripts “i = inverse,” “l = log,” and “s = statics”:

$$\mathcal{E}^{(\text{is})}(\bar{\mathbf{u}}) := \frac{1}{|\bar{\mathbf{u}} - \bar{\mathbf{u}}_{\text{st}}| - \mathcal{d}}, \quad \mathcal{E}^{(\text{ls})}(\bar{\mathbf{u}}) := -\log(|\bar{\mathbf{u}} - \bar{\mathbf{u}}_{\text{st}}| - \mathcal{d}). \quad (117)$$

Barrier functions based on satisfying the *static nonlinear operator*, with additional superscripts “p = pde,” and “k = Form k” (other than the above):

$$\mathcal{E}^{(\text{ip}, k)}(\bar{\mathbf{u}}) := \frac{1}{\|\mathcal{S}^{(k)}\| - \mathcal{d}}, \quad \mathcal{E}^{(\text{lp}, k)}(\bar{\mathbf{u}}) := -\log\left(\|\mathcal{S}^{(k)}\| - \mathcal{d}\right), \quad \|\mathcal{S}^{(k)}\| = \left[\sum_{i=1}^{i=n_i^{(k)}} \left(\mathcal{S}_i^{(k)}\right)^2 \right]^{1/2}. \quad (118)$$

Barrier functions based on the system *acceleration* (or time derivative of linear momenta), with an additional superscript “a = acceleration” (other than the above):

$$\mathcal{E}^{(\text{ia})}(\bar{\mathbf{u}}) := \frac{1}{\|\dot{\bar{\mathbf{p}}}\| - \mathcal{d}}, \quad \mathcal{E}^{(\text{la})}(\bar{\mathbf{u}}) := -\log(\|\dot{\bar{\mathbf{p}}}\| - \mathcal{d}), \quad \|\bar{\mathbf{p}}\| = [(\dot{\bar{p}}_1)^2 + (\dot{\bar{p}}_2)^2]^{1/2}. \quad (119)$$

Remark 2.1. *Acceleration barrier function.* For PDEs without an analytical static solution, the static-solution barrier function in Eq. (117) is clearly not convenient to use. For PDEs with complex, nonlinear static operators, the barrier function in Eq. (118) aiming at satisfying such a static operator is computationally inefficient. On the contrary, since the system acceleration is readily available, the acceleration barrier function in Eq. (119) is easily implemented, and computationally efficient. ■

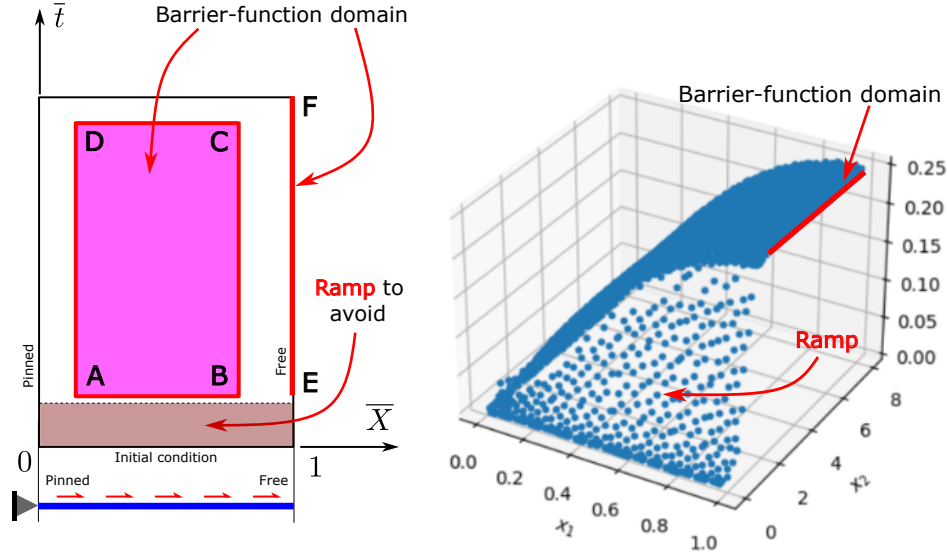


Figure 48: *Barrier-function domain.* Section 2. The barrier function domain (left), a subset of the computational domain bounded by $\bar{X} \in [0, 1]$ and $\bar{t} \in [0, \bar{t}_{\max}]$ could be the rectangle ABCD, or just the segment EF, with both avoiding the ramp zone that occurs for certain distribution of nodes in the computational domain and the network architecture, such as a random distribution of nodes (in a static solution) with a neural network having 4 hidden layers, and 32 neurons per layer for a pinned-free bar (right).

Remark 2.2. *History of logarithmic and inverse barrier functions.* In structural dynamics, as soon as we observed through our numerical experiments that the PINN minimization process could lead to a static solution, we immediately thought about adding an inverse penalty function to the PINN loss function to prevent the minimization iterate from reaching the static solution. By taking the logarithm of the inverse barrier function, we obtain the log barrier function. This was done before we checked the optimization literature, such as [22] p. 417, from where we learned of [23] and [24]. It was surprising that, according to the classic book by Fiacco and McCormick [23] p. 7, the years of appearance of these barrier functions were reversed, with the logarithmic barrier function introduced by Frisch in 1954 [25] and 1955 [24], and the inverse barrier function introduced by Carroll a few years later in 1959 [26] and 1961 [27]. ■

As an example of how the barrier function works, consider the static solution in SubFigs 27c-27d, obtained with **DDE-T** Form 1, using a network with N51 W32 H2 and 1,185 parameters. In Figure 50, SubFigs 50c-50d, an acceleration barrier (Appendix 2, Remark 2.1) was used, and effectively helped prevent the static solution, while achieving a “Very good” free-end displacement at Step 25,000, with a damping percentage of -0.6%, which measures the ratio between two successive local maxima (peaks) of free-end displacement at {0.378, 0.379}, respectively, below the more accurate peak amplitude of about 0.5 shown in Figure 28. At Step 50,000, this ratio yielded a damping percentage of -0.3%, and was thus even classified as quasi-perfect. Even though the shape of the response was far from being recognized as good, the vibration period resembled the accurate vibration period in Figure 28 (or in Figure 5), with the times for the local maxima being {2.4, 5.6}, instead of {2., 6.}.

As for the selection of the barrier depth and weight, see Figure 51 for the influence of the barrier weight w on the solution, keeping the barrier depth $\mathcal{A} = 1$. It is also possible to vary the barrier depth to illustrate its influence on the solution.

Upon removal of the barrier after Step 50,000, the static solution sprung back quickly, as shown by a precipitous drop in the loss function, the shape, and the characteristic free-end displacement with a flat

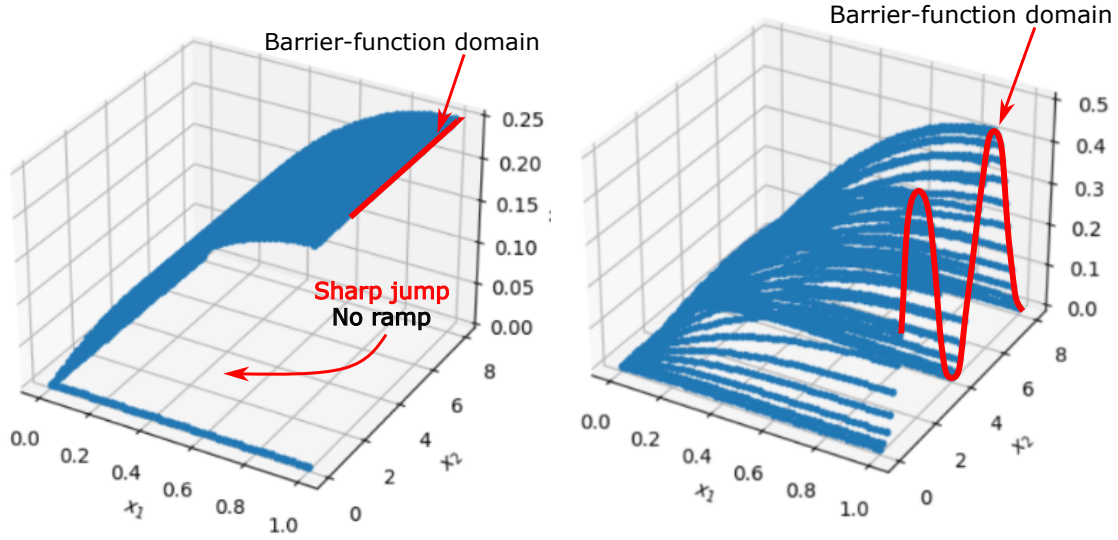


Figure 49: Expected effects of barrier function. Section 2. Pinned-free bar, axial motion. • Left: NO barrier, static solution with 4 hidden layers, 128 neurons per payer. • Right: With barrier, dynamic solution with two periods, 2 hidden layers, 32 neurons per layer.

plateau in SubFigs 50e-50g, demonstrating that the barrier function was the key player that effectively held back the static solution.

3 Error relative to exact solution, generalization

We provide here (1) a comparison of PINN results to the exact solution for the axial motion of a pinned-pinned elastic bar under a constant, uniform distributed load, (2) revealing the essentially-zero value in the transverse displacement and the pinned boundary conditions, and (3) a generalization of the motion in time beyond the space-time domain used for training.

Compared to the exact solution, the error of the displacement time history is measured by the square-root of the mean squared error (MSE), abbreviated by SMSE for short, during the time interval of interest. The relative error (RE) is obtained by dividing the SMSE by the peak-to-peak amplitude (0.25) of the exact solution (0.125) at the center of the pinned-pinned elastic bar.

Figure 52 demonstrates the limitation of the generalization—i.e., predicting the solution beyond the space-time domain used to train the network—that PINN could provide. It could however predict the displacement curving up to follow closely the upswing from the end of the training time domain ($\bar{t} = T = 4$) at which the displacement and the velocity were zero as shown in SubFigure 52c until close to half a period beyond $\bar{t} = T = 4$, i.e., the interval $[4, 5]$, with the MSE = 5.47e-4 compared to the training MSE = 0.66e-4.

Remark 3.1. PINN vs traditional FEM for generalization. Extending the time domain to obtain the numerical solution in traditional FEM using the implicit Newmark time-integration method requires additional discrete-system solution steps, which could significantly increase the computational cost. With PINN, there is no need to do optimization again, as the generalization to extend the solution beyond the training time domain $[0, T]$ is by performing the low-cost prediction (function evaluation) using exactly the same neural-network minimizers (weights and biases) obtained during the training optimization process on the previous (unextended) space-time domain. No further computational-intensive optimization is required for PINN. ■

The theoretically-zero transverse displacement in SubFigure 52b shows the *essentially-zero* value of the order of 1e-3, typical of PINN results. The zero displacement in the pinned boundary condition is not

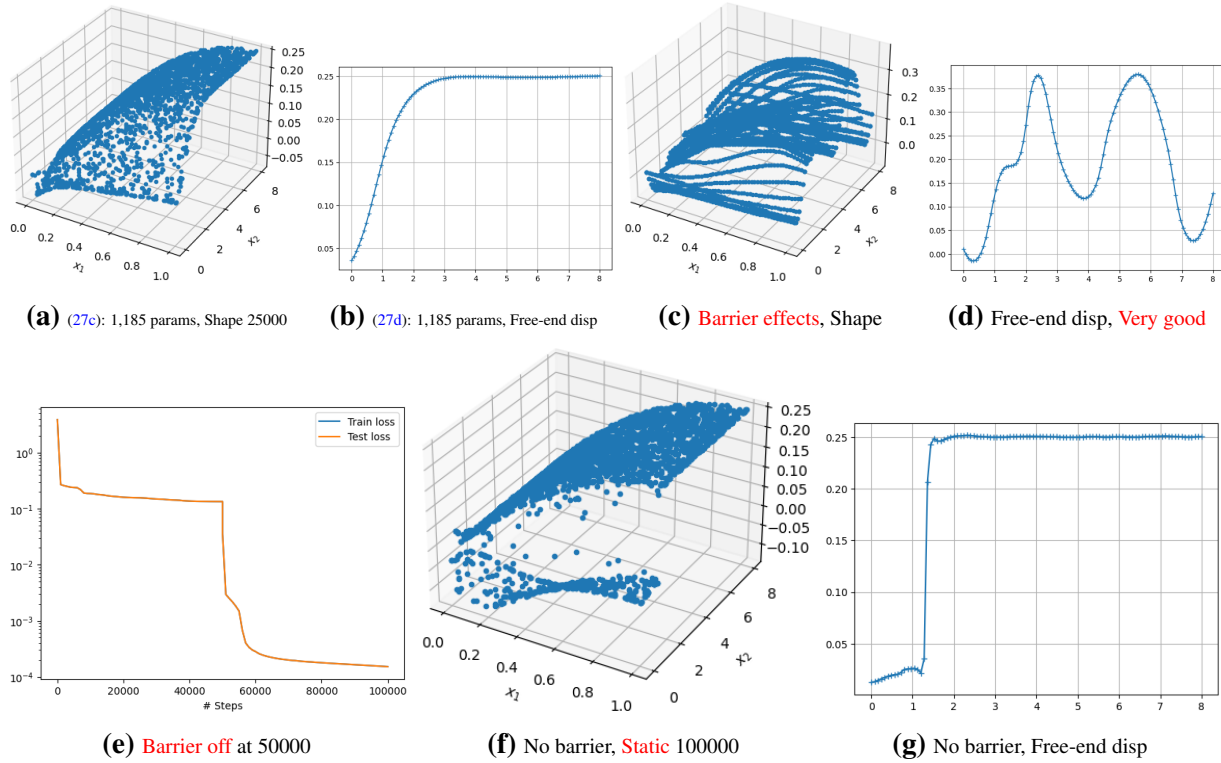


Figure 50: DDE-T. Pinned-free bar, *static* solutions, *barrier* functions. Appendix 2. Sub-Figs 50a-50b = SubFigs 27c-27d, **No barrier**, *static* solution, recalled for convenience. • Sub-Figs 50c-50d: Step 25,000, Shape, Free-end disp. ★ **Barrier** depth $d = 1$, weight $w = 1$. *Network*: Remarks 5.3, 5.5, $T=8$, $W=32$, $H=2$, $n_{\text{out}}=1$, Glorot-uniform initializer, 1,185 parameters, ★ *regular* grid. *Training*: Remark 5.6 (LRS 1), $\text{init_lr}=0.001$. Damping%=-0.6%, **Very good**. Local maxima = {0.378, 0.379}. Time at local max = {2.4, 5.6}. ▷ Step 50,000, damping%=-0.3%, **Quasi-perfect** free-end disp. (23105R1c) • SubFigs 50e-50g: **Barrier turned off** at Step 50,000. **Static solution came back**, even with random grid. (23105R1c.2) • Figure 27, DDE-T static solutions. Figure 28, using our JAX script, no static solution. ▷ Figure 38, **Form 2a**, GPU time **605 sec** for 200,000 steps. Figure 45, **Form 3**, GPU time **537 sec** for 200,000 steps. ▷ Figure 5, reference solution to compare. ▷ Figure 51, barrier-weight effects.

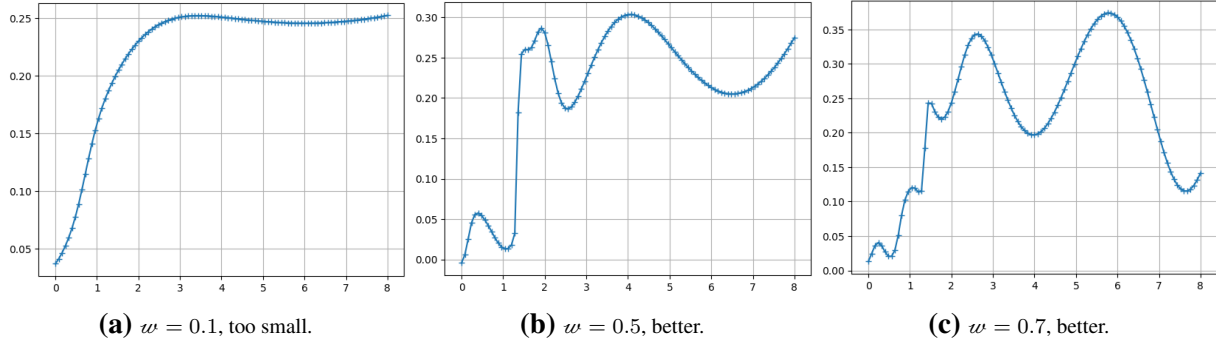


Figure 51: **DDE-T**. Pinned-free bar, *barrier weight* w effects. Appendix 2. All parameters were the same as in Figure 50, except for the barrier weight w . • SubFig 51a: $w = 0.1$, smooth, flat plateau began to curve. • SubFig 51b: $w = 0.5$, waves, bigger jump after $t = 1$. • SubFig 51c: $w = 0.7$, waves, smaller jump after $t = 1$, with two peaks clearly formed. • SubFig 50d, $w = 1.0$, smooth, no jump, with two distinct peaks.

exactly satisfied, but *essentially zero* (i.e., of the order $1e-3$). From this standpoint, the PINN displacement time history in the training interval $[0, 4]$, with its SMSE = $8e-3$ and RE = 3%, approximated well the exact solution, with *essentially-zero* difference.

Remark 3.2. *Uncertainty in real boundary and initial condition.* Traditional FEM can satisfy zero boundary and initial (BC-IC) conditions. In practice, exactly-zero BC-IC conditions are, however, an idealization, and thus *essentially-zero* BC-IC conditions could represent uncertainty in the real BC-IC conditions. ■

The zero right-end-pinned boundary condition did not generalize, i.e., remains at zero in the time interval $[4, 6]$, as shown in SubFigure 52d. SubFigure 52e shows the time history ($\bar{t} \in [0, 4]$) of the space slope along the bar length $\bar{x} \in [0, 1]$, whereas SubFigure 52f shows the right-pinned-end space-slope time history (at $\bar{x} = 1$), which is negative in the training time interval $[0, 4]$, indicating compressive state (as it should be), and is positive during generalization, corresponding to the rising curve in SubFigure 52d in the generalization time interval $[4, 6]$. In general, PINN cannot generalize to have periodicity, which is longer than the half period $[4, 5]$ beyond $T = 4$.

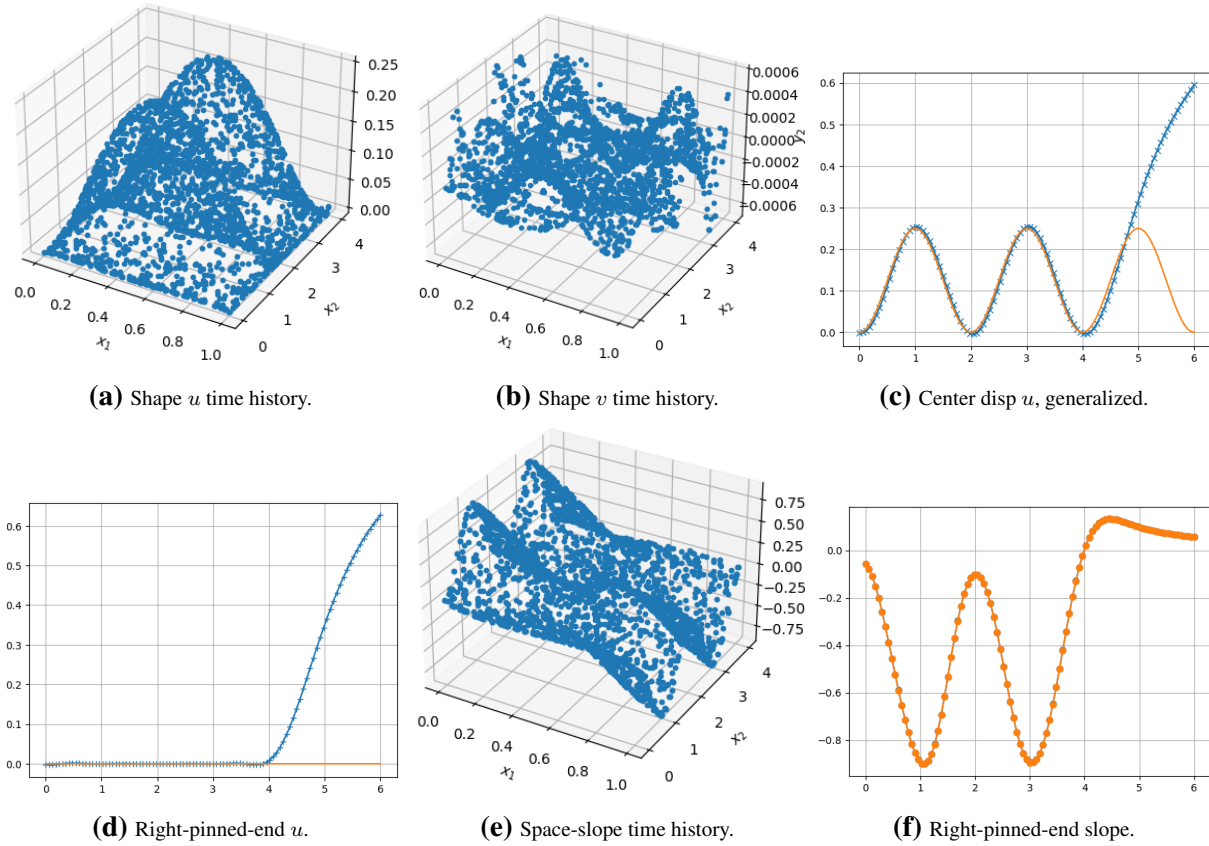


Figure 52: DDE-T. Pinned-pinned bar. Form 3.2: Step 200,000. Network: Remark 5.3, 5.5, $T=4$, $W=64$, $H=4$, $n_{\text{out}}=10$, Glorot initializer, 18,554 parameters, random grid. Training: ★ Remark 5.8 (LRS 3, NCA), $\text{init_lr}=0.01$. SubFig. 52a, shape time history (t.h.). (52b) Transverse displacement t.h., essentially-zero value of order $1e-3$. (52c) Axial displacement at bar center (blue), exact solution (orange), training SMSE = $8e-3$, RE=3%. (52d) Right-pinned-end disp u (blue) cannot generalize (should be zero, orange). (52e) Bar space slope t.h. (52f) Right-pinned end space slope t.h. (24.1.19 R1a.1b.3)